Interventional MR Elastography for the monitoring of thermal ablations

Kisoo Kim

To cite this version:

Kisoo Kim. Interventional MR Elastography for the monitoring of thermal ablations. Medical Imaging. Université de Strasbourg, 2019. English. NNT : 2019STRAD045 . tel-02525330

HAL Id: tel-02525330
https://theses.hal.science/tel-02525330

Submitted on 30 Mar 2020

UNIVERSITÉ DE STRASBOURG

ÉCOLE DOCTORALE MSII
ICube – UMR 7357

THÈSE présentée par :

Kisoo KIM

pour obtenir le grade de : **Docteur de l'Université de Strasbourg**
Discipline/ Spécialité : **Imagerie physique**
La date de soutenance : **26/11/2019**

Interventional MR Elastography for the monitoring of thermal ablations

THÈSE dirigée par :

VAPPOU Jonathan	Chargé de Recherche, CNRS, Université de Strasbourg
GANGI Afshin	Professeur, Hôpitaux Universitaires de Strasbourg

RAPPORTEURS :

PARKER Dennis L.	Professeur, University of Utah, UT
SALAMEH Najat	Professeur, University of Basel, CH

EXAMINATEURS :

BRETON Elodie	Ingénieur de recherche, CNRS, Université de Strasbourg
FELBLINGER Jacques	Professeur, Université de Lorraine, Nancy

Résumé

Le cancer est récemment devenu la principale cause de décès dans les pays les plus développés. On estime à 3,9 millions le nombre de nouveaux cas de cancers et à 1,93 million le nombre de décès en 2018 en Europe. Parmi les procédures de traitement les plus répandues, les ablations thermiques des tumeurs (ou thermothérapie) présentent l'avantage de cibler précisément les zones à traiter tout en évitant le plus possible d'endommager les tissus sains environnants. La thermothérapie est souvent combinée à une méthode d'imagerie telle que la tomodensitométrie, l'échographie ou l'imagerie par résonance magnétique (IRM). Ce suivi par l'imagerie est nécessaire car il permet au radiologue de repérer les lésions, de décider d'une stratégie de traitement et de veiller au bon déroulement de la procédure. L'IRM est une modalité permettant d'étudier avec précision les tissus mous, fournissant des images avec un meilleur contraste comparées à celles obtenues par scanner ou échographie. De plus, il s'agit d'une technique d'imagerie non invasive et non ionisante permettant d'imager des organes profonds en trois dimensions et selon n'importe quelle orientation.

Le suivi des ablations thermiques par IRM a deux objectifs spécifiques : 1) le suivi en temps réel de l'évolution de la température dans la région traitée, afin de contrôler la quantité d'énergie déposée 2) l'évaluation en temps réel des effets du traitement sur les tissus. La thermométrie IRM (TRM) est couramment utilisée pour contrôler le dépôt d'énergie thermique et estimer les dommages infligés aux tissus au cours des ablations thermiques guidées par IRM. Plus récemment, l'élasticité ou la rigidité des tissus, pouvant être mesurée par élastographie IRM (ERM), a fait l'objet d'une attention croissante en tant que biomarqueur complémentaire de la température.

Bien que le suivi de l'évolution de la température et de l'élasticité des tissus soit une technique récente largement exploitée dans le domaine de la recherche, cette technique n'est pas encore adoptée en tant que standard clinique pour le suivi des thermothérapies. Sa limitation à certains types de tissus et son faible taux de rafraichissement d'images ne répondent pas encore aux conditions d'utilisation clinique standard.

Cette thèse de doctorat présente un ensemble de méthodes développées pour la thermométrie et l'ERM interventionnelle.

La première partie de ce travail est consacrée au développement d'une séquence ERM multicoupe rapide permettant une meilleure couverture spatiale de la région concernée par la thermothérapie. Un système d'ablation HIFU (ultrasons focalisés de haute intensité) compatible IRM a été utilisé dans le cadre de cette thèse. En effet, une couverture spatiale 3D complète de la zone d'ablation est privilégiée à un simple mode d'imagerie 2D pour deux raisons. Premièrement, les images 2D peuvent se retrouver décentrées par rapport à la région d'observation et ne pas rendre compte précisément de l’échauffement réel subi par les tissus au point focal, de sorte que les évaluations de l’augmentation maximale de la température et de la localisation exacte du point focal peuvent être faussées. Deuxièmement, seule l’imagerie tridimensionnelle peut fournir avec précision la structure de la zone d'ablation, déterminée par la structure locale des tissus (flux sanguin, dépôt de chaleur, physiologie des tissus, etc.) que seule l’imagerie tridimensionnelle peut fournir. Le premier projet vise à proposer l'utilisation d’une séquence à double écho (« Simultaneous Echo Refocusing », SER) qui peut permettre l'encodage simultané ERM et l'acquisition de 2 coupes par TR, et à démontrer la faisabilité d'un suivi multi-coupe des changements de température et d'élasticité au cours des ablations thermiques. La validation de notre méthode s’est effectuée en trois étapes : une première expérience réalisée sur fantôme a d’abord permis de confronter notre nouvelle séquence d’ERM à la méthode standard. La deuxième expérience a eu pour but de valider l'utilisation de la méthode SER pour le suivi des changements de température et d'élasticité pendant une ablation HIFU. Troisièmement, l'expérience HIFU dans le tissu musculaire du poulet a eu pour but d´évaluer les variations de volume subies par le tissu pendant l'ablation HIFU.

La deuxième partie de cette thèse présente une nouvelle stratégie d'acquisition IRM rendant possible la thermométrie et l’élastographie simultanées pour le suivi des ablations thermiques dans tous les tissus mous, y compris en présence de graisse. D'un côté, la thermométrie PRFS référencée à la graisse permet de mesurer la température tout en corrigeant la dérive du champ magnétique principal. D'autre part, l’ERM permet de mesurer les propriétés mécaniques des tissus qui sont liées à des dommages structuraux tissulaires durant les ablations. La stratégie proposée offre une amélioration de la surveillance combinée ERM/TRM en temps réel des ablations thermiques, en élargissant sa précision dans les tissus mous, y compris les tissus contenant des graisses, tout en maintenant le temps d'acquisition similaire. Pour la validation, trois expériences sont effectuées. Premièrement, une mesure précise de la température est validée dans une expérience fantôme en utilisant des couples thermiques à fibres optiques. La deuxième expérience est effectuée pour valider les cartes d'élasticité obtenues comparées à celles reconstruites par la séquence d’ERM de référence. Troisièmement, des expériences HIFU dans du muscle de porc avec des fractions adipeuses homogènes sont menées pour évaluer la faisabilité clinique.

Dans cette thèse de doctorat, deux travaux différents auront un impact important sur les ERM/TRM interventionnelles en fournissant : 1) des ERM/TRM multicoupes rapides pour contrôler précisément le dépôt d’énergie; 2) une évaluation des lésions tissulaires dans les tissus mous en prenant en compte la présence de graisse.

Mots clés: imagerie par résonance magnétique (IRM), élastographie par résonance magnétique (ERM), ablation thermique, IRM interventionnelle

Abstract

In 2018, the cancer burden in Europe is estimated to 3.9 million of new cases and 1.93 million of cancer deaths. Thermal therapy has been adopted in the treatment of localized tumors over the last decade. Thermal energy is delivered in order to treat cancer tissue while minimizing normal tissue damage as much as possible. Thermal therapy is often performed in combination with Computed Tomography (CT), Ultrasound (US), and Magnetic Resonance Imaging (MRI). Radiologists rely on such real-time guidance in order to monitor the treatment response and avoid complications. MRI provides rich soft tissue contrasts compared to CT and US. Furthermore, MRI can take an image in any scan orientation and employs non-ionizing and non-invasive measures.

MR Imaging for thermal therapy has two specific aims: 1) real-time temperature monitoring that can control energy deposition. 2) assessment of tissue damage that can provide the treatment response. MR Thermometry (MRT) is commonly used to control heat deposition and to estimate tissue damage during MR-guided thermal ablations. Recently, tissue elasticity, which can be measured by MR Elastography, has received increasing attention as a biomarker that would be complementary to temperature because thermal tissue damage can affect the mechanical properties of tissue, for example, through tumor necrosis or protein coagulation.

Although temperature-elasticity monitoring for thermal ablation is already developed, this technique has not yet reach clinical use. This Ph.D. thesis applies a set of different developments dedicated to interventional MRE/MRT.

The first part of this thesis is dedicated to the development of fast multislice MRE sequence for improved spatial coverage during thermal therapy. MR-compatible High Intensity Focused Ultrasound (HIFU) device is used for this Ph.D. work. Full spatial coverage of the ablation area is desirable compared to 2D imaging for two reasons. First, the 2D images may not be properly centered on the heated zone, hence maximum temperature increase and exact heat localization may be missed. Second, the geometry of the ablation area is shaped by local tissue configuration (blood flow, spatially varying heat deposition, tissue physiology, etc.), that only 3D coverage can provide. The first project aims to propose the use of simultaneous echo refocusing (SER) that can permit simultaneous MRE encoding and acquisition of 2 slices in a single acquisition, and to demonstrate the feasibility of multislice monitoring of temperature and elasticity changes during thermal ablations. For the validation, three experiments are conducted: First, a phantom experiment is prepared for comparison with regular MRE sequence. The second experiment is conducted to validate the use of the SER method for monitoring temperature and elasticity changes during HIFU ablation. Third, HIFU experiment in chicken muscle tissue is carried out to monitor the volumetric change of tissue structure during HIFU ablation.

The second part of this thesis presents a new acquisition strategy for simultaneous fat referenced PRFS thermometry and MRE, in order to monitor thermal ablations for all types of soft tissues, including fat containing tissues. On one side, fat referenced PRFS thermometry makes it possible to measure temperature while enabling field-drift correction. On the other side, MRE enables measuring the mechanical properties of the tissue that are related to tissue structural damage during ablations. The proposed strategy offers a refinement of the combined MRT/MRE real-time monitoring of thermal ablations, extending its accuracy in soft tissues including fat containing tissues, while keeping the acquisition time similar. For the validation, three experiments are conducted: First, accurate temperature measurement is validated in a phantom experiment by using fiber optic thermal couples. The second experiment is conducted to validate elasticity maps as compared to those reconstructed with the regular MRE sequence. Third, HIFU experiments in pig rib tissue with homogenous fat fractions are conducted to evaluate the clinical feasibility.

In this Ph.D. thesis, two different works will have substantial impact on interventional MRE/MRT by providing: 1) Fast multislice MRE/MRT to control precise energy deposition. 2) Assessment of tissue damage in all types of soft tissues.

Keywords: Magnetic resonance imaging, MR Elastography, thermal ablation, interventional MRI

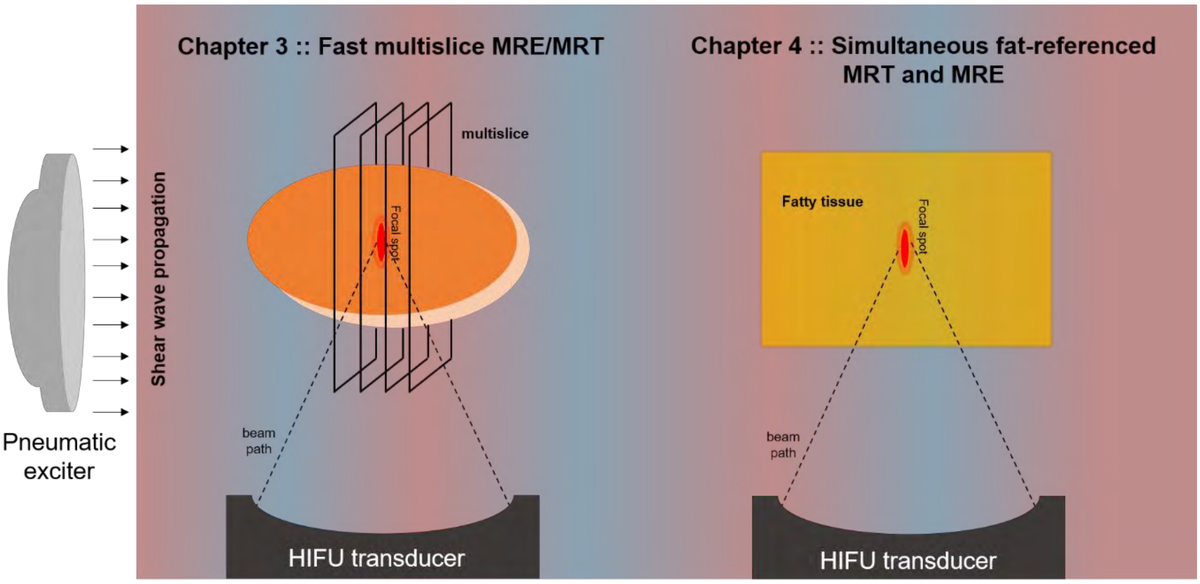

Graphical abstract

Acknowledgements

I would like to express my sincere thanks to Dr. E. Breton, CNRS and Dr. J. Vappou, CNRS for giving me scholarly criticism, unconditional support, and constant encouragement. I could not have completed my Ph.D. without their dedicated efforts.

I would also like to thank people who have kindly helped me in preparing materials regarding this Ph.D. project: Prof. A. Gangi, Hôpitaux Universitaires de Strasbourg, Dr. P. Cabras, CNRS, and MSc. K. Choquet, University of Strasbourg.

I am grateful to my parents, my sister and brother for their endless love and supports. Dear parents, I know you sacrifice all your life to give us a better life. I would like to give you all this glory. Thank you very much for your dedication. Dear my sister and brother, thank you so much for encouraging me. I could overcome hard time thanks to you.

Lastly, I wish to express here, thanks to my wife, Gieun Ji for loving and management of our household activities while I completed this Ph.D.

Contents

Abbreviations

ADC	Analog to Digital Converter
B_0	Main magnetic field
CAIPIRINHA	Controlled Aliasing in Parallel Imaging Results in Higher Acceleration
CEM43	Cumulative Equivalent Minutes at 43 ℃
CT	Computed Tomography
EPI	Echo Planar Imaging
FEM	Finite Element Modeling
FRPRFS	Fat Referenced Proton Resonance Frequency Shift
GRAPPA	GeneRalized Autocalibrating Partial Parallel Acquisition
GRE	Gradient Recalled Echo
HIFU	High Intensity Focused Ultrasound
HT	HyperThermia
IDEAL	Iterative Decomposition of water and fat with Echo Asymmetry and Least squares estimation
LFE	Local Frequency Estimation
LITT	Laser-induced Interstitial Tumor Therapy
MRE	MR Elastography
MRI	Magnetic Resonance Imaging
MRT	MR Thermometry
MSG	Motion Sensitive Gradient
MWA	MicroWave Ablation
NMR	Nuclear Magnetic Resonance
NPV	Non-Perfused Volume
PNR	Phase-to-Noise Ratio
PRFS	Proton Resonance Frequency Shift
RFA	RadioFrequency Ablation
ROI	Region Of Interest
RSC	Relative Stiffness Changes
SENSE	SENSitivity Encoding
SER	Simultaneous Echo Refocusing
SMS	Simultaneous MultiSlice
SNR	Signal-to-Noise Ratio
T_1	Longitudinal relaxation time
T_2	Spin-spin relaxation time
TD	Thermal Dose
TE	Echo Time
TR	Repetition Time
US	UltraSound
2D	2-Dimension

Chapter 1

1. Introduction

Contents

1.1 Cancer

1.1.1 Cancer epidemiology

As reported by (Ferlay et al., 2018) in 2018, Europe accounts for 9 % of the total world population while representing 25 % of the global detected cancer cases. More specifically, the cancer burden in Europe is estimated to 3.9 million of new cases and 1.93 million of cancer deaths. As shown in Figure 1.1, the most common cancers in males were prostate (450,000 cases), lung (312,000 cases), and colorectal (274,000 cases) cancers. Causes of the death in males were lung (267,000 cases), colorectal (130,000 cases), and prostate (107,000 cases) cancers. The most frequently diagnosed cancer in females was breast cancer (523,000 cases), followed by colorectal (228,000 cases) and lung (158,000 cases) cancers. The causes of the death from cancer in females were breast (138,000 cases), lung (121,000 cases), and colorectal (113,000 cases) cancers.

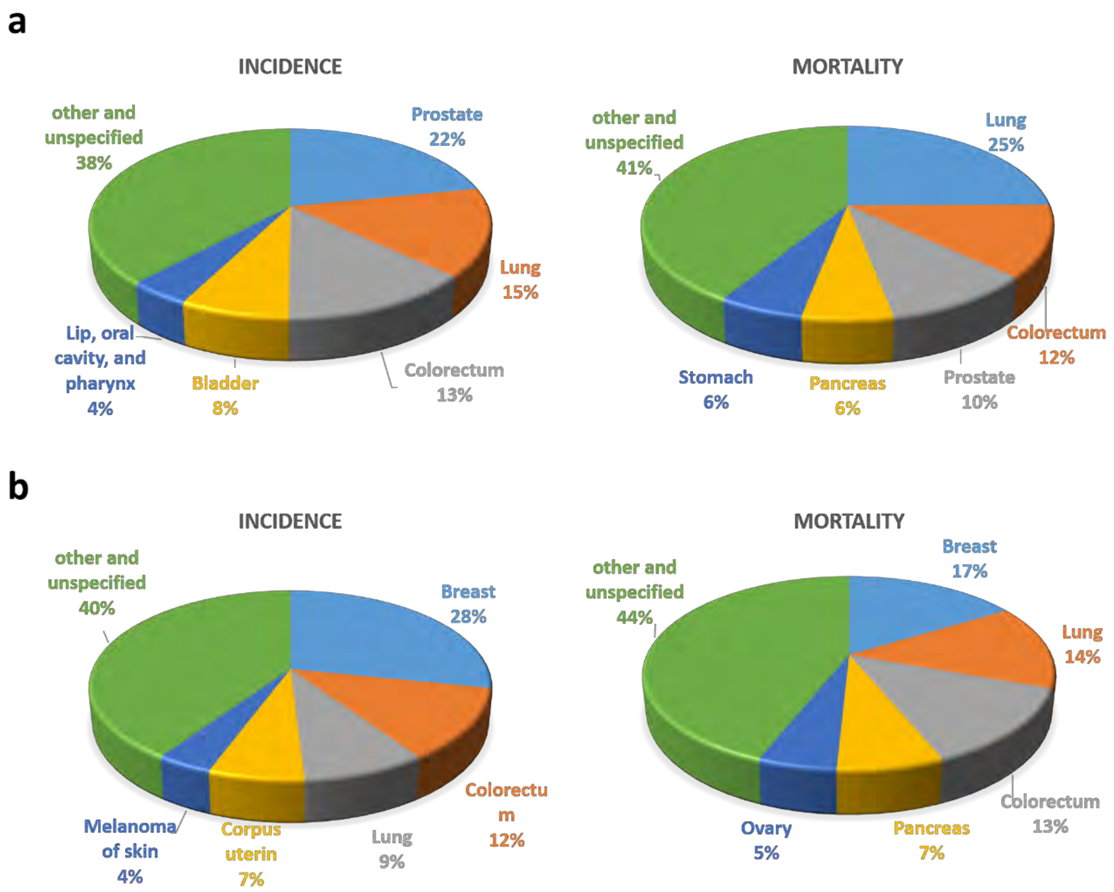

Figure 1.1 Chart of the estimated incidence and death from cancers in males (a) and females (b) in Europe in 2018. Reproduced from (Ferlay et al., 2018).

1.1.2 Cancer treatment

Cancer management is continuously under progress. Various strategies for cancer treatment can be used depending on cancer type and size (Figure 1.2).

One of the most common treatments is surgical resection, which is obviously highly invasive and requires large incisions. Currently, minimally invasive interventions that require small incisions about 1 cm in diameter are also used in specific cases in order to reduce the side effects of conventional surgical resection.

Chemotherapy can be used as a primary and/or adjuvant therapy. Its goal is to treat all cancerous cells in the body (systemic therapy) and to restrain the cancer recurrence. Conventional chemotherapeutic agents are cytotoxic, i.e. they interfere with cell division via mitosis. Other systemic therapies are immunotherapy and hormonal therapy. Generally, immunotherapy helps the immune system recognize and attack cancer cells by using checkpoint inhibitors (Pardoll, 2012). Recently, immunotherapy combined with chemotherapy has shown a great potential in many cancer types (Lake and Robinson, 2005). Hormonal therapy is usually used for hormonally responsive tissues such as breast, prostate, endometrium, and adrenal cortex. Gene expression in certain cancer cells is sensitive to the levels of certain hormones. Hence, the change in the levels or activity of hormones can stop cancer growth or can even cause cell death (Decruze and Green, 2007).

Radiation therapy is used to treat localized cancer through the use of ionizing radiation that can damage the DNA of cancerous tissues leading to cell death. Radiation beams with different angles are geometrically combined to cross each other over the target in order to provide a much larger absorbed dose in cancer tissue than in the surrounding, healthy tissue (Nutting et al., 2000).

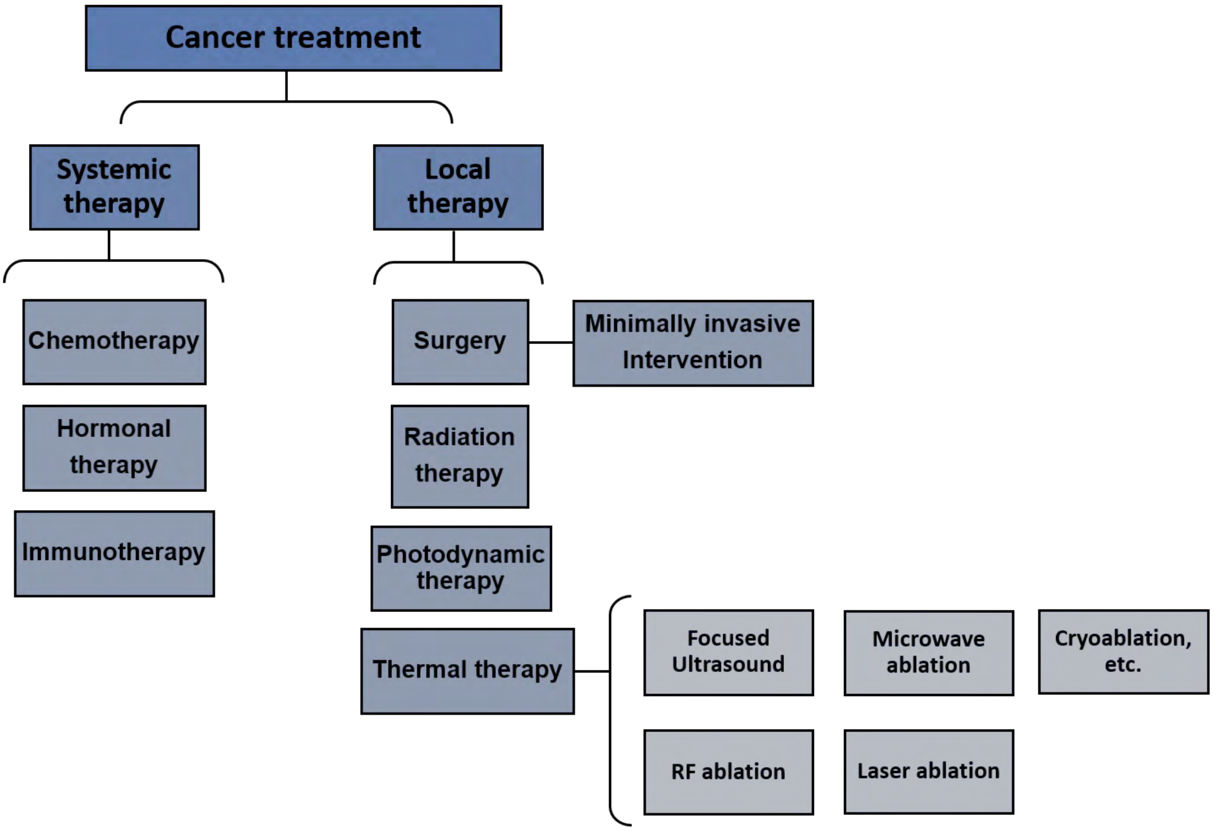

Figure 1.2 Diagram of common cancer treatments.

1.2 Thermal therapy in cancer

Thermal therapy has been increasingly used for treating localized tumors over the last decade. This approach relies on transferring thermal energy for the destruction of cancerous tissue, eradication or reduction of benign tumors and targeted tissue modification (Diederich, 2005). Many different types of ablation can be used, such as radiofrequency ablation, microwave ablation, laser ablation, cryoablation, and high intensity focused ultrasound. This chapter provides more details concerning the following aspects of thermal therapies: thermal bioeffects and heat or cold-delivery technologies.

1.2.1 Mechanisms of thermal therapy

Since its beginning, thermal therapy has been classified according to temperature range. Temperature below -20 ℃ can cause freezing injury in living cells. This approach is usually called cryoablation. On the contrary, heat-based thermal therapy is often referred to as hyperthermia (HT) or mild HT if applied in temperature ranges (39-45°C) and defined as thermal ablation if the applied temperature exceeds 45°C. Table 1.1 details typical physiological changes in soft tissues in response to temperature increases.

Cell damage can be achieved at temperature below -20 ℃, while temperatures below -40 ℃ will destroy all cells as a result of intracellular ice (Aarts et al., 2019; Baust et al., 2014). This is the basic principle of cryotherapy. Generally, cryotherapy employs a strategy including repeated freeze-thaw cycles in order to generate ice crystals in cells and/or in the extracellular space. A combination between direct rupture and destruction of the cell membrane, and cell death through dehydration resulting from osmotic effects, allows the destruction of cancerous cells.

In the range of temperature 39~45°C, living cells are affected by changes in their environment (Jain and Ward-Hartley, 1984; Tempel et al., 2016; Vaupel and Kallinowski, 1987). First, blood flow increases in response to heat (Vaupel et al., 1989). The vascular system of tumors has abnormal structure and function, which restrain tumors from meeting the requirements for oxygen level necessary to survive excessive heat (oxygenation). This temperature range can cause cell necrosis or cell death. Secondary, tumor vessels become more permeable. High temperature causes the fatty acid tails of the phospholipids to loosen and increases protein mobility within the membrane (Vígh and Maresca, 2002). The resulting increased vessel permeability results in higher chemotherapy-drug uptake in cancer cells (Lande et al., 1995; Tempel et al., 2016). Furthermore, heated tumor cells release exosomes and heat shock proteins, which makes them become more sensitive to NK cells and T cells. A recent study has proven that hyperthermia can contribute to the activation of the immune system (Toraya-Brown and Fiering, 2014).

Higher temperature (>45℃) causes ischemia, hypoxia, and microvascular thrombosis to tumor tissues (Brace, 2011). Protein denaturation is generated over 60℃, while temperatures over 100℃ vaporize tissue water, and carbonization occurs in tissues over 300℃.

Table 1.1 Physiological changes in response to temperature (Brace, 2011; Tempel et al., 2016).

Temperature range (℃)	Physical & Biological effects
≤-40	Intracellular ice
39 – 45	Blood flow ↑ Vessel permeability ↑ Drug uptake ↑ Activation of the immune system ↑
45-100	Protein denaturation (>60℃) Coagulation, ablation
100-300	Vaporization
>300	Carbonization

1.2.2 Clinical devices

1) Radiofrequency ablation (RFA)

RFA was first introduced in 1891 by d'Arsonval (d'Arsonval, 1891). Currently, there are many examples of clinical RFA devices for treating tumors in liver, lung, kidney, bone, and glandular tissue, etc. (Brace, 2009; Hayashi et al., 2003; McGahan and Dodd, 2001). RFA relies on Joule heating by high RF current with frequencies ranging from 375 to 480 kHz (Clasen and Pereira, 2008).

Monopolar RFA device use an insulated needle (electrode) and a grounding pad placed on the tissue. This device may induce thermal injuries caused by an electrical current flowing from the electrode to the grounding pad. To overcome the potential side effects, a bipolar RFA device uses two electrodes on a single probe which allows for limited current pathway within the treatment area (Figure 1.3) (Osaki et al., 2013).

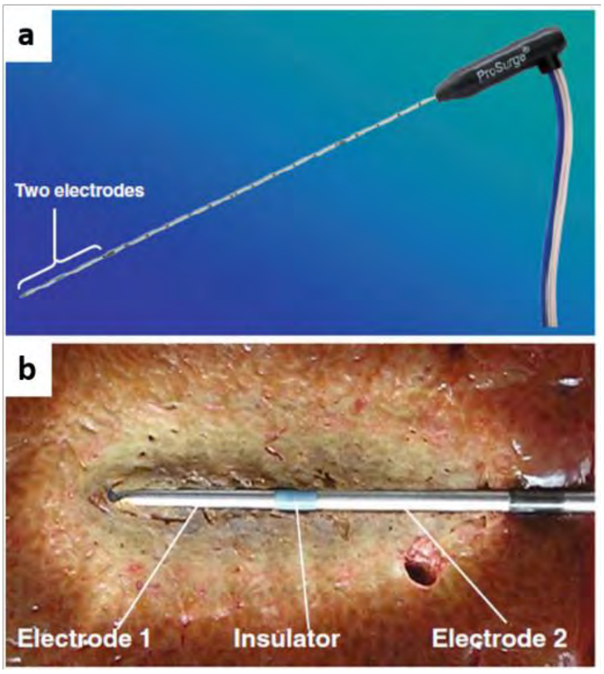

Figure 1.3 An example of the bipolar RFA system. The applicator has two electrodes near its tip. Reproduced from (Osaki et al., 2013).

2) Microwave ablation (MWA)

MWA uses electromagnetic waves applied at high frequencies (915 MHz or 2.45 GHz) (Brace, 2009). The dipole moment of polar molecules, such as H_2O, is rotated by aligning to the alternating electromagnetic field. Thus, the localized EM field results in Dielectric heating inside tumors.

MWA can be a more efficient heat source than RFA in certain tissues with low or zero conductivity such as lung or bone (Lubner et al., 2010; Simon et al., 2005), because materials with low conductivity inhibit RF current flow while allowing EM wave propagations. In addition, MWA can treat larger tissue volume, typically faster than RFA, and does not require any grounding pads.

3) Laser-induced interstitial tumor therapy (LITT)

When high powered short-wavelength laser interacts with materials, the absorbed light is converted into heat. LITT relies on thermal effects of lasers, transmitted to tissue through an optical fiber. The size of active heating depends on the size of the optical fiber tip, laser wavelength, and thermal and optical properties of the tissue (Brace, 2011; Garnon et al., 2013). LITT treatment is reserved for the treatment of small focal lesions (less than 9 mm in diameter), while multiple fibers can be used simultaneously to treat larger tumors (Wu et al., 2018).

LITT is easily compatible with imaging modalities, especially with MRI because of fiber materials, consisting of glass and plastic. Currently, LITT has been used in particular for the treatment of brain (Carpentier et al., 2012), prostate (Oto et al., 2013), liver (Dick et al., 2003), and bone (Hibst, 1992).

4) Cryoablation

During cryoablation, the tip of the probe reaches a temperature as low as -75 ℃, and then tissue is allowed to thaw. The freezing and thawing process is repeated several times in order to result in the formation of intracellular ice (Baust et al., 2014). The typical size of the inner core of the ice ball (reaching temperatures below -40°C) is 2 cm (Shah et al., 2016). One strong advantage of cryoablation is that multiple cryoprobes can be combined in order to treat larger tumors, the ice ball being shaped to cover the morphology of the lesion.

Imaging modalities such as CT and MRI are generally used to control cryoablations in order to evaluate the ice growth during the treatment. Figure 1.4 shows the MR-guided cryoablation system at the University hospital of Strasbourg. Low-signal area in T_2-weighted images corresponds to the presence of the ice ball (Figure 1.4c, white arrow).

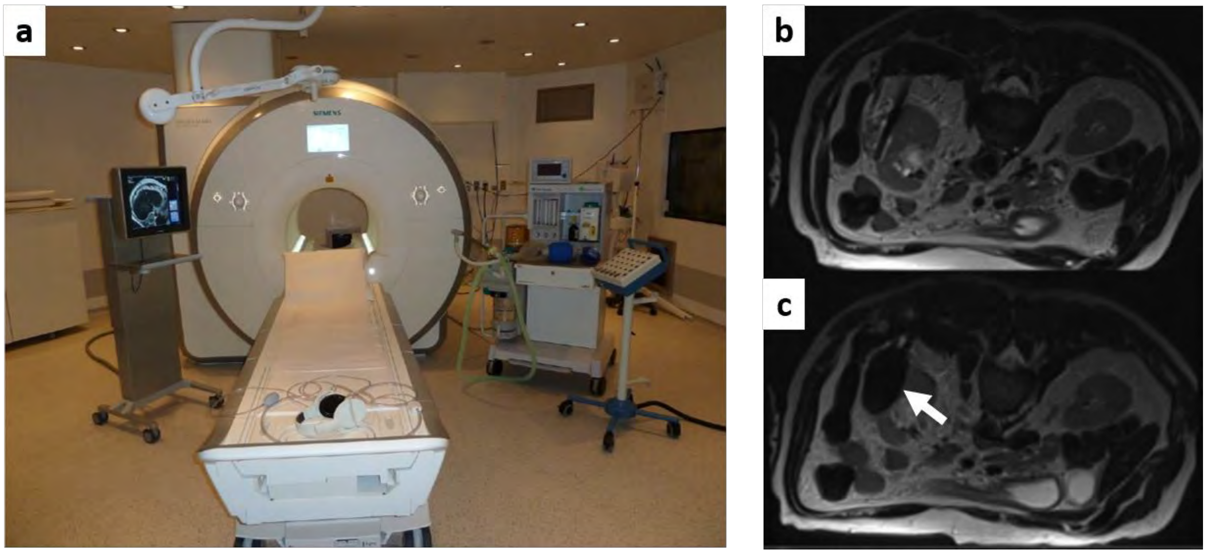

Figure 1.4 (a) Interventional MR with cryoablation system (right) at University hospital of Strasbourg, France, (b) T_2-weighted image for verification of the probes position, (c) monitoring of ice-ball during cryotherapy (white-arrow). Reproduced from (Tsoumakidou et al., 2012).

5) High intensity focused ultrasound (HIFU)

Wood et al. first observed the biological effect of high-intensity ultrasound on ex-vivo tissues (Wood and Loomis, 1927). Fry et al. made thermal lesions within the central nervous system in several animal experiments (Fry et al., 1955). Clinical use of HIFU emerged in the 1990s thanks to progress in medical imaging that allowed better targeting and monitoring.

- *HIFU transducer*

A typical HIFU transducer is made of a piezoelectric array that can be concave for a natural pre-focusing as shown in Figure 1.5. Each piezoelectric element generates mechanical stress when an electric field is applied. The mechanical stress results in an ultrasound (US) wave propagating through the body. Typically, the HIFU transducer can be operated with acoustic compression pressures up to 70 MPa, peak rarefaction pressures of up to 20 MPa, and intensities of 100-10000 W/cm^2 (Dubinsky et al., 2008; Napoli et al., 2013a). In contrast, the pressure and the intensity of the diagnostic ultrasound transducer is generally used within the 0.001-0.003 MPa and 0.1-100 W/cm^2 ranges, respectively. Biological effects of ultrasound can be classified into two categories, depending on the ultrasonic waveform and the intensity range: Mechanical effects and thermal effects.

- *Mechanical effects*

Several mechanical phenomena resulting from intense ultrasonic fields have been observed (Dubinsky et al., 2008): 1) cavitation, 2) microstreaming, and 3) radiation forces. At very high pressures, ultrasonic wave rarefaction can result in the formation of an air bubble. These air bubbles obtained through cavitation will keep oscillating if the US propagation is continued. Stable cavitation occurs when such oscillations are stable and oscillate at specific modes. Unstable cavitation can be seen as an uncontrolled oscillation that can result in bubble expansion and tissue damage through implosion, yielding extremely high, localized pressure and heat. Fluid microstreaming can also occur under high amplitude acoustic oscillations. The fluid velocity due to microstreaming is associated with shear stresses that can have a biological effect. Fluid microstreaming can also occur around oscillating microbubbles. Lastly, radiation forces result from the interaction between the US wave and an absorbing medium. The radiation force can 'push' inside the medium, which can also have a biological effect.

- *Thermal effects*

High energy density can cause heat over a small volume. Such temperature increase is associated with the following parameters in the Bio-Pennes equation (Pennes, 1948):

$$\rho C_p \frac{\partial T}{\partial t} = \nabla(k\nabla T) + q_p + q_m - wC_b(T - T_b) \qquad \text{Equ. 1.1}$$

Where ρ is tissue density ($\approx$1000 kg/m^3), T is temperature (°C), T_b is the temperature of blood (°C), C_p is specific heat, C_b is the blood specific heat, w is the local blood perfusion rate (kg/m^3/s), k is the tissue thermal conductivity (W/m/°C), q_p is the energy deposition (W/m^3), and q_m is the heat due to metabolism, which is often negligible compared to q_p in cases of hyperthermia. In the case of HIFU heating, q_p depends on tissue acoustic absorption α and ultrasound intensity I: $q_p = 2\alpha I$

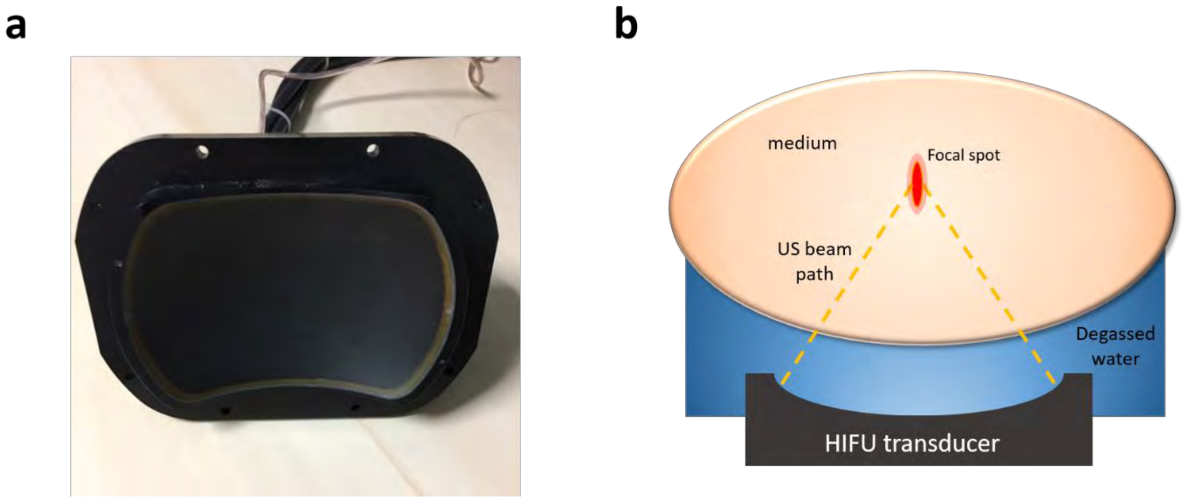

Figure 1.5 (a) photo and (b) illustration of a 256-element HIFU transducer (Image Guided Therapy, Inc., Pessac, France). A HIFU transducer consists of phased-array elements disposed so that the transducer can focus within a given spatial zone. Degassed water is used for ultrasound transmission.

- *MR-guided HIFU ablation*

Thermal ablations are often performed under Computed Tomography (CT), Ultrasound (US), or Magnetic Resonance Imaging (MRI) guidance. This guidance is essential for ensuring treatment safety and efficiency. MRI provides intrinsically rich soft tissue contrast compared to CT and US. It enables image acquisition in any scan orientation and employs non-ionizing radiation. Additionally, MRI can offer functional and metabolic imaging as well as quantitative assessment of temperature changes induced by thermal ablations. Owing to these advantages, MR-guided thermal therapy systems have been used in clinical practice as an alternative to conventional surgical ablation (Jolesz, 2009). In particular, MR-guided HIFU is particularly relevant, due to the fact that US HIFU technology can be made compatible with MR with relative ease, and that MR thermometry provides essential information in real time for ablation monitoring.

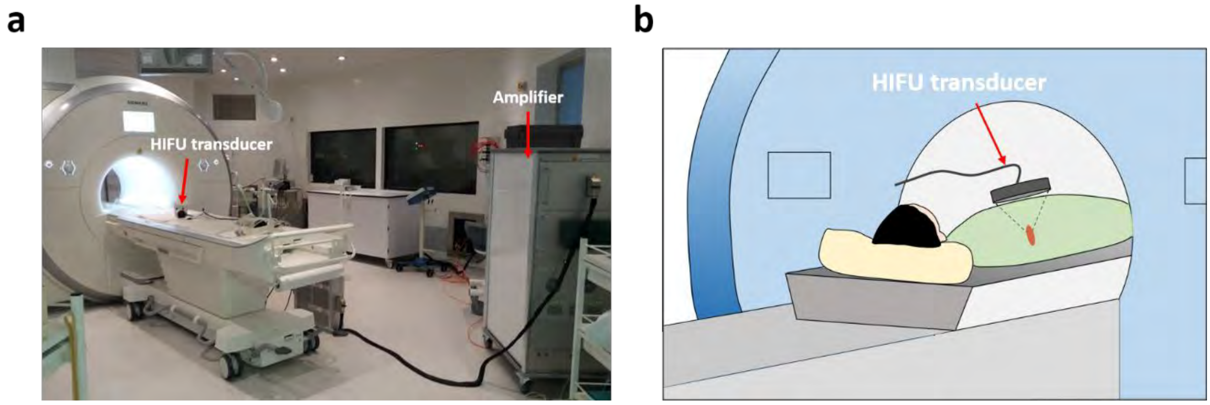

Figure 1.6 (a) MR-guided HIFU system (Image Guided Therapy, Inc., Pessac, France) at University hospital of Strasbourg, France, (b) an illustration of HIFU setup

1.3 MR monitoring of thermal therapy

MR Imaging for thermal therapy has two specific aims: 1) real-time temperature monitoring to control the energy deposition; 2) assessment of tissue damage that can provide information on treatment response.

MR Thermometry (MRT) is commonly used for temperature monitoring during thermal therapy. Several MR parameters are sensitive to temperature, such as proton density, T_1 and T_2 relaxation times, diffusion coefficient, and the water proton resonance frequency shift (PRFS). In particular, PRFS-based MRT is the most commonly used method for monitoring thermal therapy because of its high sensitivity to temperature changes obtained during thermal therapies, and its high temporal resolution on the order of a few seconds (Rosenberg et al., 2013; Zhu et al., 2017). More details of the mechanisms of PRFS and other temperature-sensitive parameters will be described in Chapter 2 (page 22).

1.3.1 Biomarkers reliable for thermal tissue damage

In 1984, Sapareto and Dewey proposed the thermal dose model for damages from temperature-time history (Sapareto and Dewey, 1984). The cumulative Equivalent Minutes at 43 °C (CEM43) model is defined to estimate a thermal isoeffect dose through the exposure time (Sapareto and Dewey, 1984; van Rhoon et al., 2013):

$$CEM43 = \sum_{i=1}^{i \cdot \Delta t} R^{(43-T_i)} \cdot \Delta t \qquad \text{Equ. 1.2}$$

$$with\, R = \begin{cases} 0.25 & T_i < 43°\mathrm{C} \\ 0.50 & T_i \geq 43°\mathrm{C} \end{cases}$$

Where Δt is the time interval, i is the measurement number, and T_i is the temperature of the i^{th} measurement.

Therefore, the cumulative thermal dose (TD) represents an integration of temperature over time and has been shown to be a reliable marker of tissue damage. For example, if mild temperature ranges (~45°C) are maintained for a few minutes, it can induce protein coagulation (Figure 1.7). Recent studies have proposed improved thermal dose models including tissue characteristics such as tissue thickness, heat diffusion, and local blood perfusion rates, etc. (MacLellan et al., 2018; Napoli et al., 2013b). However, fundamental limitations when using TD alone for monitoring thermal ablations over time need to be mentioned, such as the fact that TD thresholds are still tissue-dependent (van Rhoon et al., 2013), and that TD is particularly sensitive to any uncertainty or bias due to its cumulative property (Vappou et al., 2018). TD has also been shown to be poorly correlated to non-perfused volume (NPV), a reliable marker of post-ablation tissue damage, showing potential errors of MR Thermometry due to long-term heat accrual (Bitton et al., 2016). In addition, PRFS thermometry in fat-containing tissues may result in significant temperature errors depending on echo time, fat fraction, and extent of temperature increase because the temperature dependent electron-screening constant in fat is negligible compared to the one of water protons (Rieke and Pauly, 2008a; Taylor et al., 2011).

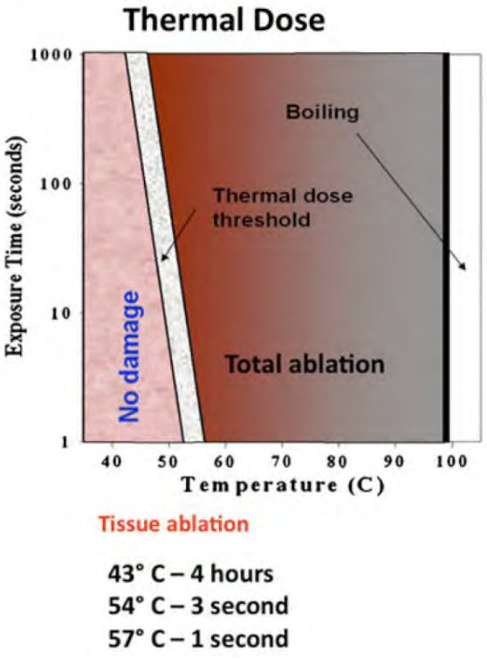

Figure 1.7 Thermal dose depending on temperature and exposure time. Reproduced from (Napoli et al., 2013b).

MRI can provide additional biomarkers for tissue damage complementary to temperature. Table 1.2 shows several biomarkers that relate to thermal tissue damage. The measurement of T_1 or T_2 relaxation times can provide accurate temperature information in fat containing tissues and reflect the degree of tissue damage (Baron et al., 2014; Todd et al., 2014). Magnetization transfer ratio has also been shown to describe thermal damage through its analysis of protein levels (Peng et al., 2009). As reported by (Kwon et al., 2014), MR Electrical impedance tomography can be used for measuring the change in electrical conductivity of the ablated tissue.

Table 1.2 Biomarkers for thermal tissue damage.

Reference	Biomarkers	Field strength [T]	Tissue type	Application	Temperature↑ vs.
(Todd et al., 2014)	T_1 (for fat), PRFS (for water)	3.0	Ex-vivo porcine muscle	HIFU	T_1↑
(Baron et al., 2014)	T_2 (for fat)	1.5	In-vivo porcine liver	HIFU	T_2↑
(Peng et al., 2009)	Magnetic transfer ratio, PRFS	3.0	Ex-vivo porcine muscle	HIFU	Magnetic transfer ratio↑
(Kwon et al., 2014)	Electrical conductivity	3.0	Ex-vivo bovine	RFA	σ ↑
(Kruse et al., 2000)	Elasticity	1.5	Ex-vivo bovine skeletal muscle	Themally regulated holder	Shear modulus↓
(Wu et al., 2001)	Elasticity	1.5	Ex-vivo bovine	HIFU	Shear modulus ↓ (Shear modulus ↑ over 60°C)
(Chen et al., 2014)	Elasticity	1.5	In-vivo porcine liver	Laser	Shear modulus ↑
(Corbin et al., 2016a)	Elasticity, PRFS	1.5	In-vivo porcine liver	Laser	Shear modulus ↑

1.3.2 Mechanical properties as biomarker

Thermal tissue damage can induce changes in the mechanical properties of tissues, for example, through tumor necrosis or protein coagulation. In 1998, Stafford et al. first investigated the use of US elastography to distinguish the extent of thermal damage in several lesions (Figure 1.8) (Stafford et al., 1998). Mariani et al. investigated thermal lesions in pig liver using US shear wave elastography (Mariani et al., 2014). RFA was performed for thermal ablation and the thermal lesion was visualized under combined shear wave elastography with B-mode imaging (Figure 1.9).

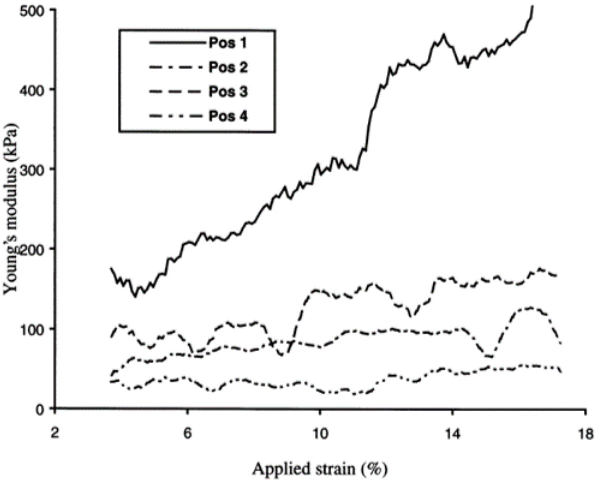

Figure 1.8 Young's modulus as a function of the strain of laser ablation applied in ovine kidney. Position 1 (pos 1) is in the center of the lesion. Position 2 is in an intermediate position in the lesion. Position 3 (pos 3) is in the border of the lesion. Position 4 (pos 4) is in the normal tissue. Reproduced from (Stafford et al., 1998).

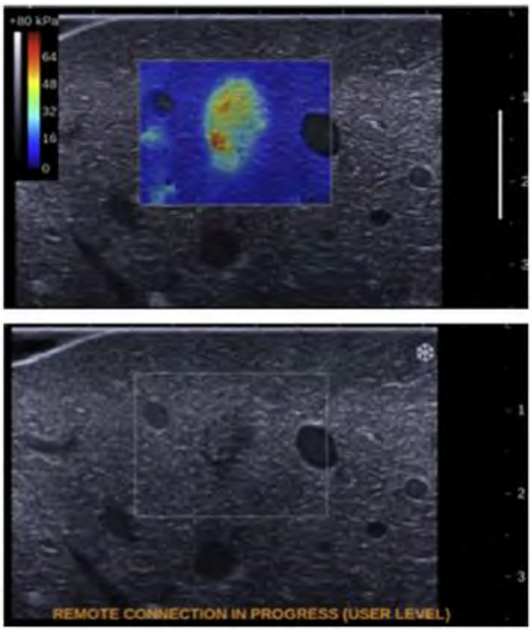

Figure 1.9 Shear waves elastography (top) and B-mode image (bottom). The ablated lesion has higher Young's modulus than the surrounding normal tissues. Reproduced from (Mariani et al., 2014).

In the field of MRI, MR Elastography (MRE) offers the possibility to measure the mechanical properties of soft tissues non-invasively. Such measurements are quantitative as they rely on the estimation of the velocity of shear waves propagating within the tissue. Wu et al. established a relationship between temperature and elasticity changes measured with MRE in ex-vivo bovine muscle tissue (Wu et al., 2001). They observed that the shear modulus of ex-vivo bovine tissues decreased in the temperature range from 20 ℃ to around 60 ℃, which can be explained by protein unfolding during heating. Over 60 ℃, protein structural changes started to become irreversible. Thus, the shear modulus increased and did not go back to its original value during cooling down (Figure 1.10).

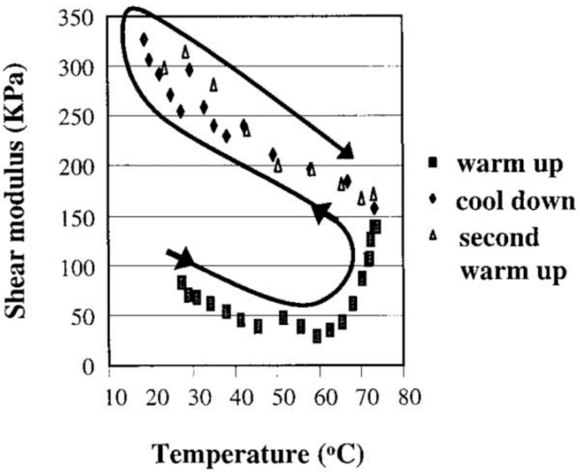

Figure 1.10 Shear modulus of ex-vivo bovine tissue measured with MRE at various temperature. The arrow indicates increasing experimental time. This graph illustrates tissue shear modulus changes during the heating and cooling process. Reproduced from (Wu et al., 2001).

More recently, Chen et al.(Chen et al., 2014) have demonstrated the feasibility of monitoring changes in elasticity of porcine liver in-vivo as a result of laser ablations. Liver elasticity was found to increase significantly after ablations.

Corbin et al.(Corbin et al., 2016a, 2016b) proposed an interventional MRE protocol and method that allows for simultaneous PRFS temperature and elasticity monitoring within a few seconds (Figure 1.11). This interventional MRE system was developed in our laboratory. It includes a needle MRE driver, a respiratory triggered gradient-echo sequence with motion encoding and an online reconstruction method that provides elasticity and temperature measurements in real-time. Changes in elasticity and temperature occurring during laser thermal ablation are successfully measured in-vivo over 20 minutes thanks to this interventional MRE system (Corbin et al., 2016a).

Hofstetter et al. (Hofstetter et al., 2019) proposed a new MR-shear wave elastography approach that can measure elasticity within an in-plane area of ~5 × 5 cm, using multiple acoustic radiation force pushes. Ex-vivo HIFU experiment in bovine liver was performed and MR-shear wave elastography showed the evolution of shear wave speed in the ablated zone (Figure 1.12). This technique allows for monitoring changes in shear wave speed due to HIFU ablation.

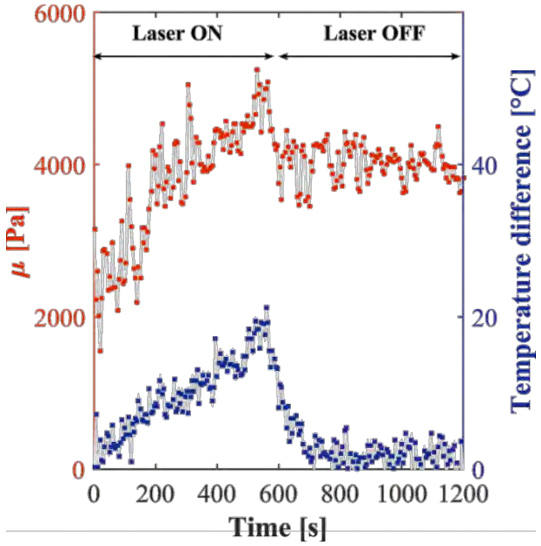

Figure 1.11 Evolution of the shear modulus (red) and the temperature during a laser ablation in swine liver in-vivo.

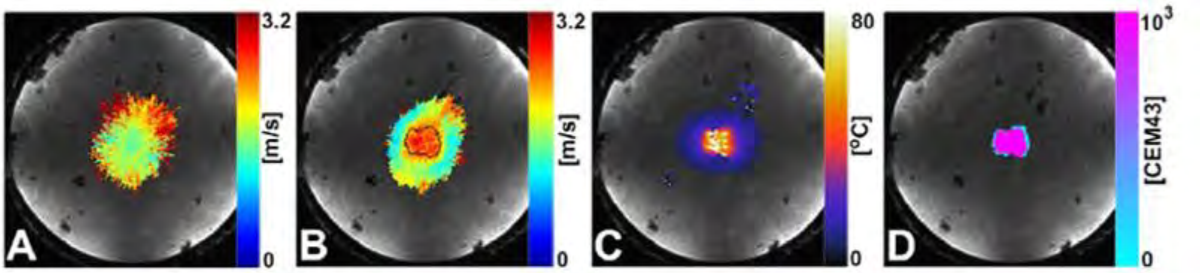

Figure 1.12 Ex-vivo HIFU experiment. Shear wave speed maps measured before (A) and after (B) ablation. Temperature map (C) and corresponding thermal dose (D). The thermal dose threshold of 240 CEM43 is overlaid as a black line in (B). Reproduced from (Hofstetter et al., 2019).

1.4 Research objective

As previously mentioned, tissue elasticity has received increasing attention as a biomarker for assessing therapy response during thermal ablation. Recent studies have demonstrated the possibility of using both MR Elastography and MR Thermometry simultaneously in order to monitor tissue damage.

This Ph.D. thesis applies a set of different developments dedicated to interventional MRE/MRT for the monitoring of hyperthermia. The first part of this thesis is dedicated to the development of a fast multislice MRE sequence for improved spatial coverage during thermal therapy. Full spatial coverage of the ablation area is desirable compared to 2D imaging for two reasons. First, the 2D images may not be properly centered on the ablation area. Second, the geometry of the ablation area is shaped by local tissue configuration (blood flow, spatially varying heat deposition, tissue physiology, etc.), that only 3D coverage can provide. The first project aims to propose the use of simultaneous echo refocusing (SER) (Feinberg et al., 2002) for the acquisition of 2 slices sharing a single MRE gradient encoding in a single TR, and to demonstrate its use for multislice monitoring of temperature and elasticity changes during thermal ablations.

The second part presents a new acquisition strategy for simultaneous fat referenced PRFS thermometry and MRE, in order to monitor thermal ablations for all types of soft tissues, including fatty tissues. On one side, fat referenced PRFS thermometry makes it possible to measure temperature while enabling field-drift correction (Hofstetter et al., 2012). On the other side, MRE enables measuring the mechanical properties of the tissue that are related to tissue structural damage during ablations. The proposed strategy offers a refinement of the combined MRT/MRE real-time monitoring of thermal ablations, extending its accuracy in soft tissues including fat containing tissues, while keeping the acquisition time similar.

1.5 Outline

This PhD dissertation is organized as follows:

Chapter 2 introduces the basic principles of PRFS-based MR Thermometry and MR Elastography, including a historical review. The purpose of this chapter is to provide a theoretical background for the understanding of chapters 3 and 4.

Chapter 3 describes the use of simultaneous echo refocusing (SER) for accelerating the multislice MRE acquisition. The proposed method is demonstrated in three experiments: First, a phantom experiment is prepared to compare with regular MRE sequences. A second experiment is conducted to validate the use of the SER method for monitoring temperature and elasticity changes during HIFU ablation. Third, a HIFU experiment in chicken muscle tissue is carried out to monitor the volumetric change of tissue temperature and elasticity during HIFU ablation.

Chapter 4 provides a new framework for simultaneous fat referenced PRFS Thermometry and MRE. Accurate temperature measurement is validated in a phantom experiment by using fiber optic thermal sensors. In addition, elasticity maps are compared to those reconstructed with regular MRE-GRE sequence. Then, HIFU experiments in pig rib muscle tissue with homogenous fat fractions are conducted to evaluate the feasibility to extend into clinical practice.

Chapter 5 provides a general discussion about this Ph.D. thesis and the field of interventional MRE.

Chapter 2

2. General background

Contents

2.1 Magnetic Resonance Imaging

This summarizes some of the basic principles of magnetic resonance imaging (MRI) that are required to understand the following chapters. Additional mathematical details will be found in (Bernstein et al., 2004).

2.1.1 NMR signals and image reconstruction

For the sake of simplicity, let us consider a 2D image acquired in the x-y plane. The microscopic magnetization of each hydrogen nucleus processes at the Larmor angular frequency ω around the axis of the main magnetic field B_0 as follows:

$$\omega = \gamma B_0 \qquad \text{Equ. 2.1}$$

Where the gyromagnetic ratio of the hydrogen nuclei γ is 267.522×10^6 rad/s/T. At thermal equilibrium, the macroscopic magnetization of a spin system within a static magnetic field is aligned with the axis of this static magnetic field. When a radio-frequency excitation pulse oscillating at the Larmor frequency is applied, the direction of the macroscopic magnetization is tilted way from the main magnetic field, towards the transverse plane perpendicular to the main magnetic field axis. In the transverse plane, the magnetization $M_\perp$ is detected in receive coils as a complex signal oscillating with the precession of spins at the Larmor frequency.

MRI exploits three gradients in orthogonal directions in order to encode spatial information in the NMR signal: a slice selection gradient, a frequency encoding gradient, and a phase encoding gradient. First, the slice selection gradient induces a linear spatial variation of the Larmor frequency (in this example applied along the z-direction) so that a radio-frequency pulse centered at its central frequency can tip the magnetization away from the main magnetic field direction in a given slice. Second, the phase encoding gradient (in this example applied along the y-direction) provides each row of pixels in the image with a given phase. Third, the frequency encoding gradient (in this example applied along the x-direction) relates the precession frequency of the spin to its position along each line of pixels, during signal acquisition.

This signal is recorded in the dataset, called ‘k-space’ (Figure 2.1). An MR sequence is performed for each phase encoding step and is repeated in order to fill all rows in the k-space. The NMR signal measured in the receive coil contains the sum of all spins having different frequencies. Therefore, the k-space data can be written as:

$$S(k_x, k_y) = \int\int M_{\perp}(x,y)e^{-i2\pi \cdot x \cdot k_x}e^{-i2\pi \cdot y \cdot k_y}dx\,dy \qquad \text{Equ. 2.2}$$

Where $S(k_x, k_y)$ can represent a full k-space dataset in the spatial frequency domain, x and y are the spatial coordinates along the Ox and Oy axes respectively, G_x is a frequency encoding gradient, k_x is equal to $(\gamma/2\pi)\int_0^{T_x} G_x(t)dt$, $G_y(t)$ is a phase encoding gradient, and k_y is equal to $(\gamma/2\pi)\int_0^{T_y} G_y(t)dt$ where T_x is the duration of the prephasing gradient and T_y is the duration of the G_y lobe.

The transverse magnetization $M_{\perp}(x,y)$ can be reconstructed by the inverse Fourier transform of $S(k_x, k_y)$. From this complex image, magnitude and phase images can be derived as shown in Figure 2.1. The magnitude image indicates the intensity of the NMR signal and the phase image includes a frequency information of the NMR signal.

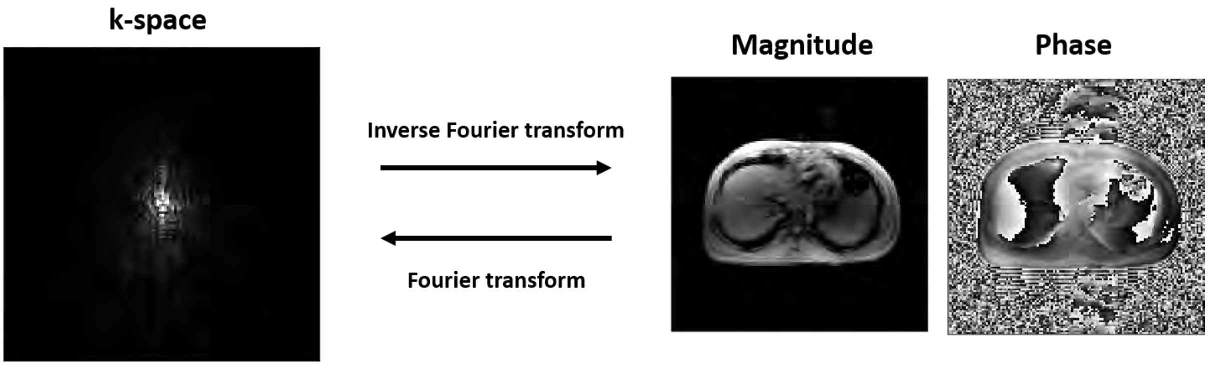

Figure 2.1 An example of k-space (magnitude) and corresponding magnitude and phase images, that can be reconstructed by the inverse Fourier transform of the complex k-space data.

2.2 MR Thermometry

2.2.1 Temperature dependent MR parameters

1) Proton density

The proton density can be derived from the Boltzmann distribution (Abragam, 1961) at thermal equilibrium. Therefore, the temperature can be estimated by the proton density as follows:

$$proton\ density \propto \chi_0 B_0 \qquad \text{Equ. 2.3}$$

$$\chi_0 \propto 1/T$$

Where the susceptibility χ_0 is inversely proportional to the temperature T. The relative change in temperature is calculated by the change in proton density, but the temperature sensitivity is about -0.3 %/°C, requiring high Signal-to-Noise Ratio (SNR) (Rieke and Pauly, 2008b). In addition, the change in the proton density depends on the change in the susceptibility related to thermal damage, not temperature alone. Therefore, it is not clinically used to measure temperature during thermal therapy.

2) T_1 relaxation time

As reported in (Kahn and Busse, 2012), the temperature-dependence of the longitudinal relaxation time T_1 was first modeled by:

$$T_1 \propto e^{-E_a(T_1)/kT} \qquad \text{Equ. 2.4}$$

Where $E_a(T_1)$ is the activation energy of the relaxation time and k is the Boltzmann constant. T_1 increases with an increase in temperature. Recently, the hybrid T_1- and PRFS- based MR Thermometry was developed for monitoring temperature in fatty and aqueous tissues, simultaneously (Todd et al., 2014). Its temporal resolution is 3.8 s, which might be sufficient for the monitoring of clinical thermal therapy. The temperature dependence of T_1 was found to be 8 ms/°C in the adipose breast tissue. However, additional T_1 variations occur when irreversible changes are induced in tissue structure. Hence the tissue temperature dependence of T_1 does no longer follow a linear relationship when irreversible changes occur.

3) T_2 relaxation time

The transverse relaxation time T_2 is not receiving much interest in the field of MR Thermometry because of its nonlinear relationship with temperature in aqueous tissues. Recently, several studies proposed to use T_2 for measuring the temperature in adipose tissues and bone marrow (Baron et al., 2014; Ozhinsky et al., 2016). Their findings are that T_2 in fat is linearly proportional to temperature. Its temperature sensitivity is about 5-7 ms/°C.

4) R_2^* relaxation rate

The transverse relaxation rate R_2^* is defined as the inverse of T_2^*.

$$R_2^* = \frac{1}{T_2^*} = \frac{1}{T_2} + \gamma \Delta B_0 \qquad \text{Equ. 2.5}$$

Where ΔB_0 is the field inhomogeneity and γ is the gyromagnetic ratio.

R_2^* can be usually estimated using a multi-echo dataset. (Lorenzato et al., 2014) reported that the multi-echo gradient echo sequence can be used for temperature monitoring with R_2^* change. In addition, PRFS temperature can be estimated from the multi-echo dataset. As shown in Equ. 2.5, R_2^* reflects the change in the field inhomogeneity, which can be affected by the change in susceptibility induced by temperature change. Therefore, it is possible to estimate temperature change through R_2^* change. The temperature sensitivity was found to be about 0.35 s^{-1}/°C in porcine muscle (Lorenzato et al., 2014).

5) Diffusion

Diffusion imaging allows for measuring the Brownian-motion of the water molecules. The relationship between diffusion and temperature was summarized by (Le Bihan et al., 1989) as follows:

$$D \propto e^{-E_a(D)/kT} \qquad \text{Equ. 2.6}$$

Where D is diffusion coefficient, $E_a(D)$ is the activation energy of the diffusion of water molecules, and k is the Boltzmann constant. As reported by (Rieke and Pauly, 2008b), the temperature sensitivity is about 2%/°C, which is acceptable in clinical practice. However, the relationship between temperature change and diffusion change is highly dependent on tissue characteristic and condition (Bleier et al., 1991).

2.2.2 Proton Resonance Frequency Shift based MR Thermometry

Proton Resonance Frequency shift (PRFS) -based MR Thermometry is the most commonly used method for monitoring thermal ablations thanks to its high sensitivity to temperature ($\approx -0.01\ ppm/℃$) within the temperature range encountered during hyperthermia. The sensitivity of PRFS to temperature was first established by (Hindman, 1966). In 1995, Ishihara et al. proposed PRFS-based MR Thermometry in a gradient echo sequence (Ishihara et al., 1995). The resonance frequency in a molecule in the main magnetic field B_0 is given by the Larmor frequency (Equ. 2.1). However, hydrogen bonds in water molecules come loose as temperature increases, leading to increased electron screening of ^{1}H nucleus, and therefore to lower proton resonance frequency (Ishihara et al., 1995). This phenomenon is called the water proton resonance chemical shift (PRFS) with temperature. The local magnetic field can be expressed as:

$$B_{loc} = (1 + s)B_0 \qquad \text{Equ. 2.7}$$

Where s is the electron-screening constant or shielding constant of the water proton. Hence, Equ. 2.1 becomes:

$$\omega = \gamma(1 + s)B_0 \qquad \text{Equ. 2.8}$$

The temperature dependent electron-screening constant of the water proton is expressed as:

$$s(T) = \alpha T \qquad \text{Equ. 2.9}$$

Where α is the PRFS coefficient of the water proton about -0.0103 $\pm$ 0.0002 ppm/℃ (Hindman, 1966). As shown in Figure 2.2, it is possible to estimate relative temperature changes by monitoring local resonance frequency variations in hydroxide.

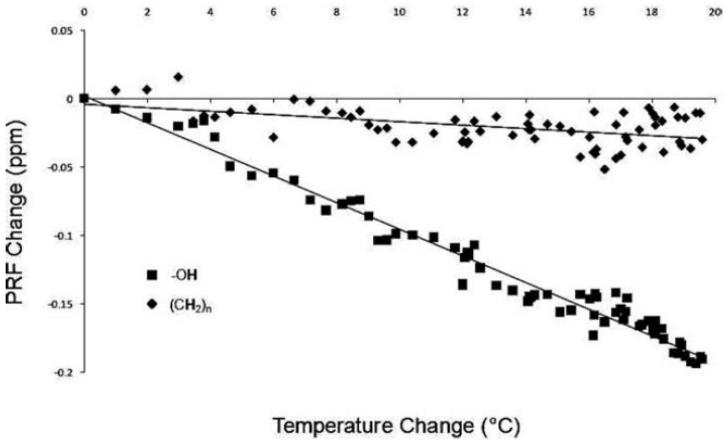

Figure 2.2 Temperature dependent PRFS in -OH and -CH_2. The temperature increase is related to PRFS in hydroxide, but not to PRFS in methylene. Reproduced from (Taylor et al., 2011).

In gradient echo sequences, relative phase shifts are proportional to temperature, and hence can be converted to temperature changes as follows:

$$\Delta T = \frac{\phi(T) - \phi(T_0)}{\gamma \alpha B_0 TE} \qquad \text{Equ. 2.10}$$

Where ΔT is the temperature difference relative to the reference image, $\phi(T)$ is the current phase image, $\phi(T_0)$ is the reference phase image, γ is the gyromagnetic ratio, α is the temperature sensitive coefficient, B_0 is the main magnetic field, TE is the echo time. The reference phase image (before heating) is subtracted to the current phase image (during heating). Finally, the temperature calculated from Equ. 2.10 is accumulated in order to estimate tissue damage via the CEM43 model as described in chapter 1.3 (Figure 2.3).

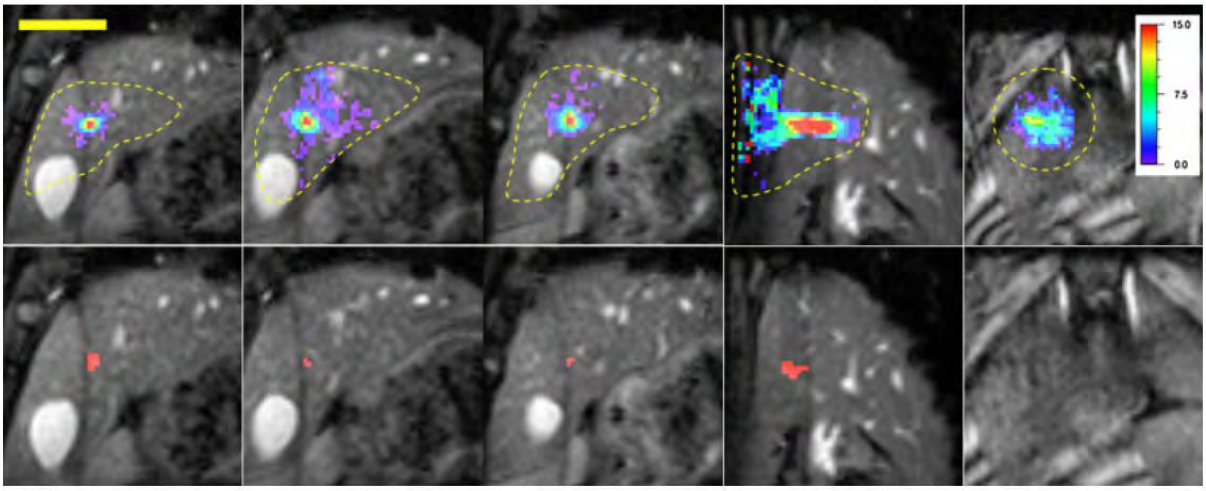

Figure 2.3 Temperature (top row) and thermal dose (bottom row) images of the liver during HIFU ablation. The region exceeding the 240CEM43 is shown in red in the thermal dose image. MR images are obtained by a single-shot gradient-recalled echo planar imaging (EPI) sequence with multislice acquisition. Reproduced from (Quesson et al., 2011).

2.3 MR Elastography

2.3.1 Introduction

MRE is already being used clinically for the assessment of liver fibrosis. The extent of liver fibrosis can be assessed by measuring the mechanical properties of the liver (Taouli et al., 2009). As shown in Figure 2.4, stiffness increases together with the degree of fibrosis.

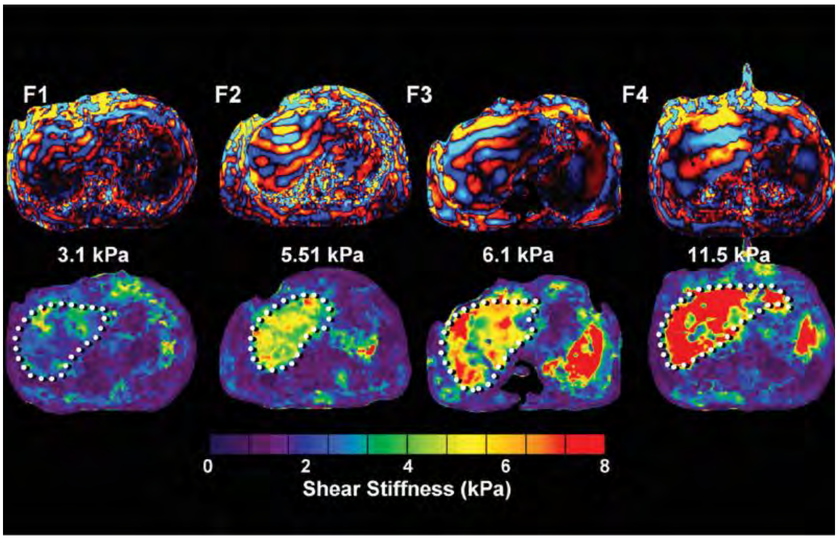

Figure 2.4 Stiffness increase in the liver corresponds to increasing fibrosis level (F1 to F4). The wavelength increases along with fibrosis level. Reproduced from (Venkatesh Sudhakar K. et al., 2013).

Additionally, MRE can detect many pathological changes due to cancer. For example, breast and liver cancers are stiffer than healthy tissues (Figure 2.5) (Pepin et al., 2015). The stiffness of lesions may be increased due to abnormal vasculature and high interstitial fluid pressure. In the brain, the stiffness of meningioma appears to be softer than the surrounding brain tissue (Murphy et al., 2013). As reported by (Murphy et al., 2011), Alzheimer disease results in significantly softer stiffness than healthy brain tissue. Also, MRE has shown potential to evaluate other diseases, such as renal parenchymal disease (Rouvière et al., 2011), lung parenchyma disease (Mariappan et al., 2011), cardiac amyloidosis (Arani et al., 2017), etc.

Figure 2.5 Evaluation of breast cancer in human, obtained by MRE. Stiffness of the cancerous tissue is significantly higher than that of healthy glandular tissue. White dashed line points out the cancer lesion. Reproduced from (Pepin et al., 2015).

2.3.2 Principle of MRE

Measuring tissue elasticity using MRE requires three main elements listed as follows:

1) Applying displacements

The first step is the generation of shear waves within the region of interest using an internal or external acoustic exciter. The most common MRE mechanical excitation source consists in using an external pneumatic driver. As shown in Figure 2.6, the acoustic source is an active driver that is placed outside of the MRI scanner, and the acoustic wave is transmitted to an MR-safe passive driver, placed in contact with the body. A flexible membrane on the surface of the passive driver transmits the vibration to the body, resulting in the propagation of shear waves (Venkatesh Sudhakar K. et al., 2013).

Other technologies for excitation have been used, such as electromechanical or piezoelectric actuators (Sack et al., 2008; Uffmann et al., 2002; Vappou et al., 2007). Generating waves directly within the organ of interest has also been proposed, through the use of percutaneous instruments transmitting the vibration induced by a piezoelectric actuator (Corbin et al., 2016b; Yin et al., 2007). As reported by (Corbin et al., 2016b), an MR-compatible piezoelectric stack driver is used to make the tip of a needle vibration in the longitudinal direction and directly creates the acoustic wave to propagate away from the needle shaft in the transverse direction. Alternatively, the displacement can be also induced by acoustic radiation force from HIFU excitation (Hofstetter et al., 2019; Souchon et al., 2008; Wu et al., 2000).

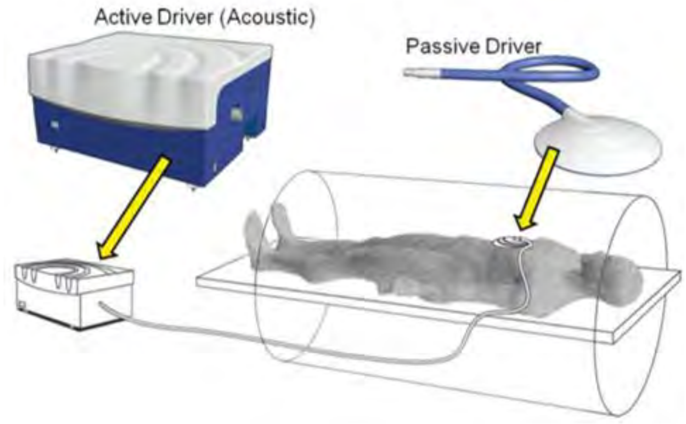

Figure 2.6 Illustration of a pneumatic MRE driver system. Reproduced from (Venkatesh Sudhakar K. et al., 2013).

2) Measuring displacements

The harmonic oscillation $\vec{\xi}(t)$ induced by the propagating shear wave can be described as:

$$\vec{\xi}(t) = \overrightarrow{\xi_0} \cdot sin\left(2\pi f \cdot t - \vec{k} \cdot \vec{r}\right) \qquad \text{Equ. 2.11}$$

Where $\overrightarrow{\xi_0}$ is the motion amplitude, f is the frequency of the applied harmonic wave, $\vec{k}$ is the wave number and $\vec{r}$ is the position vector.

The second step of MRE consists in encoding the shear wave using MRI. If Equ. 2.1 is expressed as a function of time, then the resonance frequency can be written as:

$$\frac{d\phi}{dt} = \gamma B(t) \qquad \text{Equ. 2.12}$$

Let us assume that an additional bipolar gradient $\vec{G}$ is applied while the tissue undergoes a harmonic wave motion. The bipolar gradient $\vec{G}$ consists of two trapezoidal lobes (each with the same gradient area, and with opposite polarity). As shown in Figure 2.7, the first lobe of the gradient $\vec{G}$ and the mechanical wave results in phase shifts and the second lobe of the gradient $\vec{G}$ and the mechanical wave accumulates the same phase shifts because both the polarity of the gradient and the displacement are inverted together. The MRE encoding gradient $\vec{G}$ is usually called the motion sensitive gradient (MSG) and is applied in a specific direction in which it encodes the spatial component of the shear wave.

Therefore, the local magnetic field $B(t)$ in the presence of the bipolar gradient $\vec{G}$ and harmonic shear wave $\vec{\xi}(t)$ becomes:

$$B(t) = B_0 + \vec{G}(t) \cdot \left(\vec{r_0} + \vec{\xi}(t)\right) \qquad \text{Equ. 2.13}$$

Where $\vec{r_0}$ is the initial position vector of tissue at time $t = 0$.

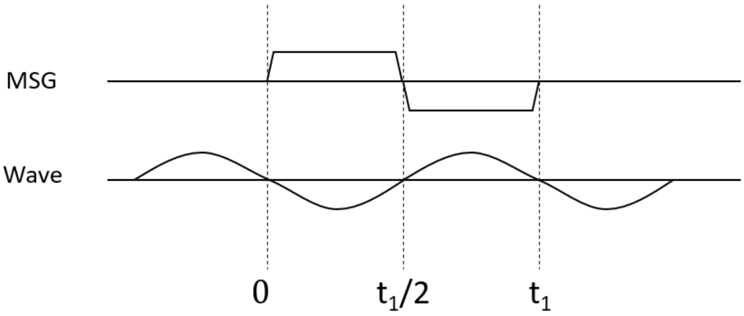

Figure 2.7 Chronogram of the MSG and the mechanical wave. t_1 is the period of the MSG and the mechanical shear wave.

Equ. 2.11 becomes:

$$\frac{d\phi}{dt} = \gamma\left[B_0 + \vec{G}(t) \cdot \left(\vec{r_0} + \vec{\xi}(t)\right)\right] \qquad \text{Equ. 2.14}$$

Hence, the phase of the MR image contains information about the tissue motion as follows:

$$\phi = \gamma \int_0^t \left[B_0 + \vec{G}(t) \cdot \left(\vec{r_0} + \vec{\xi}(t)\right)\right] dt \qquad \text{Equ. 2.15}$$

The phase of the MR image described in Equ. 2.15 can also be written as:

$$\phi = \phi_0 + \phi_m \qquad \text{Equ. 2.16}$$

Where ϕ_0 stands for the background phase and ϕ_m reflects the phase accumulation resulting from the shear wave encoding. Two strategies can be adopted in order to remove the static background phase reflecting B_0 field inhomogeneities. A background phase image (ϕ_0) can be acquired prior to the shear wave propagation so that it can be subtracted to the following phase images acquired during shear wave propagation, under the assumption that the background phase remains constant during the acquisition.

The most commonly adopted strategy consists in acquiring two-phase images with opposed MSG polarities, so that Equ. 2.16 translates into:

$$\begin{cases} \phi_+ = \phi_0 + \phi_m \\ \phi_- = \phi_0 - \phi_m \end{cases} \qquad \text{Equ. 2.17}$$

Where ϕ_+ and ϕ_- are phase values acquired from MSG$+/-$, respectively. Subtracting the phase images one to another results in the suppression of the static background phase ϕ_0, while the motion-induced phase shift ϕ_m is doubled (Equ. 2.18):

$$\phi_m = (\phi_+ - \phi_-)/2 \qquad \text{Equ. 2.18}$$

Although that approach doubles the acquisition time compared to a unique reference scan, the strong gain obtained in terms of Phase-to-Noise Ratio (PNR) makes it the current state-of-the-art for diagnostic MRE.

Phase encoding can be seen as a convolution between an MSG and a mechanical wave, which means that frequencies other than the main excitation frequency can also be encoded. In order to extract the fundamental frequency of the motion, the wave propagation is captured at different time points by varying the time offset between the MSG and the mechanical wave. Theses phase difference images ($\phi_{m1}, \phi_{m2}, \phi_{m3}, \dots$) are processed by applying a temporal Fourier transform in order to isolate the motion at the fundamental frequency. The phase offsets are typically evenly spaced across a mechanical period. Estimating the mechanical properties (Next section) is performed on the resulting filtered wave image.

Figure 2.8 shows the chronograms of typical gradient echo- and spin echo-MRE sequences including the MSG.

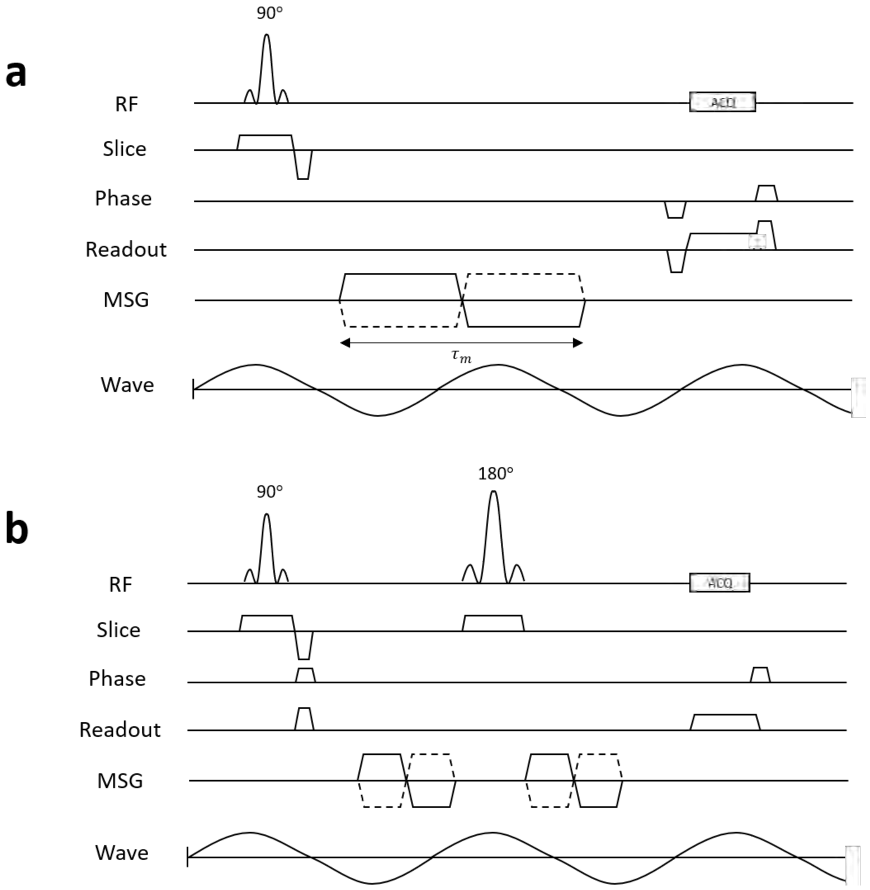

Figure 2.8 Chronograms of typical gradient echo MRE sequence (a) and spin echo MRE sequence (b). In general, those sequences are implemented with interleaved acquisitions varying the polarity of MSG (solid line: MSG+, dashed line: MSG-). τ_m is the period of the MSG, here different from the period of the mechanical shear wave.

3) Estimating the mechanical properties

For estimating the mechanical properties, several inversion algorithms have been used to transform the wave images into elasticity maps. Before applying any algorithm on MRE data set, the biomechanical behavior of the tissue must be correctly modeled. Several assumptions can be made about tissue biomechanical behavior, such as simple linear elasticity, viscoelasticity (Sack et al., 2008; Sinkus et al., 2005; Vappou et al., 2007), anisotropy (Chatelin et al., 2016) or poroelasticity (McGarry et al., 2015). In this work, we will assume pure linear elasticity, which is a common assumption in clinical practice. It results in the following expression between the shear modulus and shear wave velocity:

$$\mu = \rho c^2 = \rho(\lambda f)^2 \qquad \text{Equ. 2.19}$$

Where ρ is the density of soft tissues, c is the shear wave speed, and f and λ are the mechanical frequency and the wavelengh in tissue, respectively.

One of the methods for estimating the shear modulus is to evaluate the wavelength λ from the wave images. Manduca et al. proposed a way to estimate the local frequency using the combination of several lognormal filters, namely local frequency estimation (LFE) algorithm (Manduca et al., 1996). This approach can produce a robust estimate of the shear modulus in the presence of noise and heterogeneous geometry.

Another way to estimate the shear modulus is solving the differential equation of motion, namely, a direct inversion (Oliphant et al., 2001). Since the computation is performed on the basis of the equations of motion in a small region, its spatial resolution is better than the LFE algorithm and it is possible to measure the viscoelastic properties of tissue (Sack et al., 2008; Sinkus et al., 2005). However, a direct inversion approach is typically sensitive to noise, while the LFE algorithm is relatively robust to noise. An alternative method is based on an optimization process between computed and experimental displacement fields (Van Houten et al., 1999). However, this method requires particularly long computational time.

In this Ph.D. thesis, the LFE algorithm was used because of its robust and fast estimate of the shear modulus. We will focus mainly on this inversion method for the following sections.

Figure 2.9 shows a summary of the MRE process, illustrated in a gelatin phantom made of two halves with different stiffness. In summary, the MR phase image represents the shear wave displacement field, encoded by the bipolar gradients (MSG) as formalized in Equ. 2.15. A 2D phase unwrapping algorithm (Goldstein et al., 1988) is applied to the phase images. The two-phase images with opposite MSG polarities are subtracted from one another. It allows for the suppression of the static background phase and increasing motion sensitivity by a factor of 2. In addition, several phase offsets between the MSG and the wave propagation are used in order to extract the motion at the fundamental excitation frequency thanks to a temporal Fourier transform. Note that the difference in wavelength between both halves of the phantom in Figure 2.9 is visible in the real part of the Fourier transformed wave image: the shorter wavelength on the left corresponds to the softer half. Lastly, the LFE algorithm is applied to the filtered wave image, providing the local spatial frequency of the shear wave in the image domain. This wavelength is used in Equ. 2.19 for the shear modulus estimation.

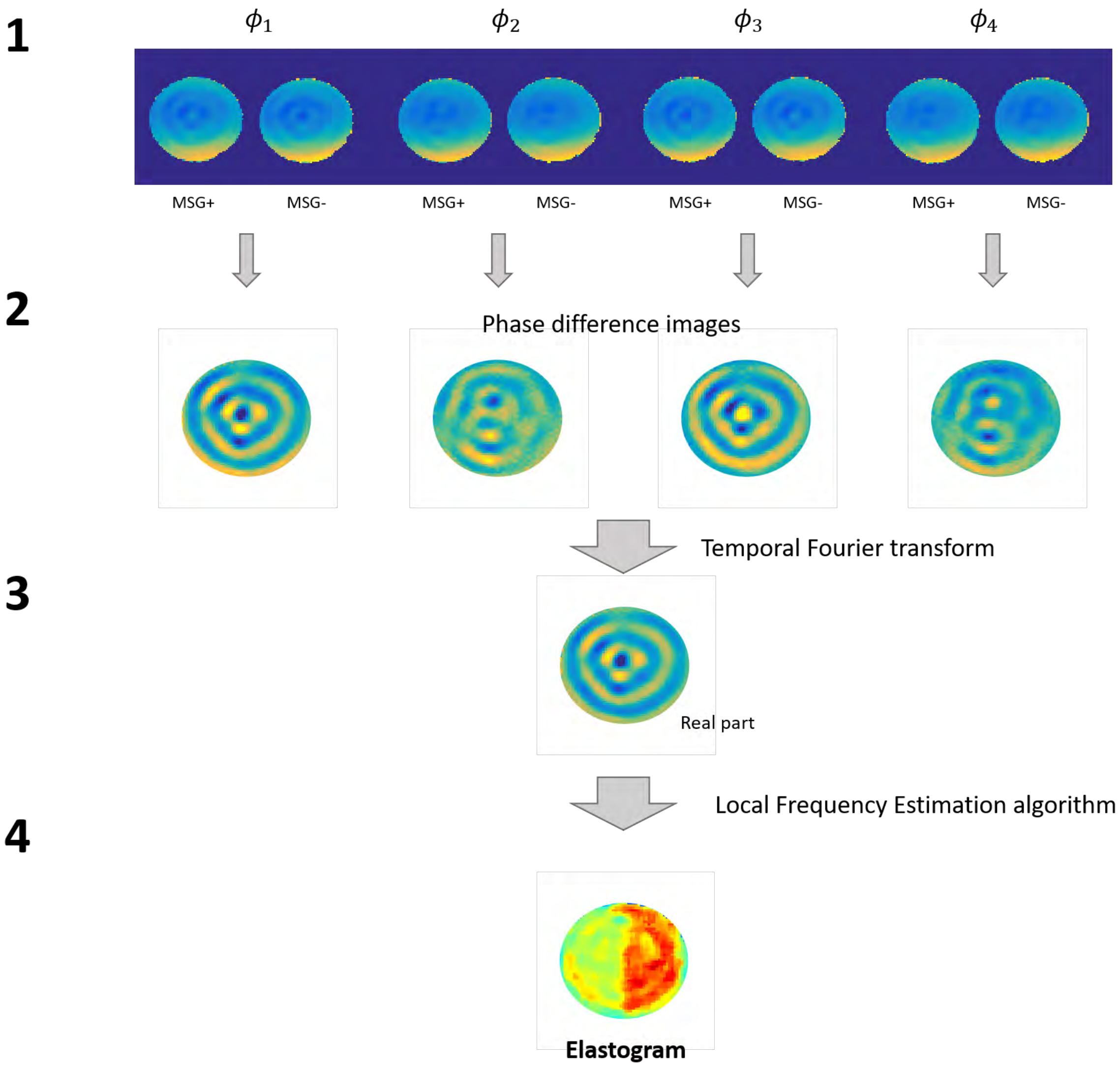

Figure 2.9 Flow chart of the MRE processing. ϕ_i (i=1,2,3,4) is the phase offset. In step 2, phase difference images correspond to the subtraction of a pair of phase images acquired with opposite MSG polarities. In step 3, because temporal Fourier transform generates complex wave values, real parts of the result are shown in this figure. In step 4, the local frequency of the shear wave obtained in step 3 is used in Equ. 2.19 to evaluate the shear modulus.

2.4 Simultaneous MR Thermometry and MR Elastography

As previously mentioned, temperature and elasticity should be measured in real time for accurate monitoring of thermal therapy. Thanks to a particular data processing method, it is possible to extract both PRFS thermometry and elasticity from the same sequence without additional acquisition time.

Le et al. first proposed this simple method to derive PRFS data from gradient echo MRE datasets (Le et al., 2006), in which two phase images are acquired with opposed MSG polarity for each mechanical phase offset. Each phase image consists of temperature-dependent PRF phase shift ϕ_T, the background phase ϕ_0 (including the static background phase and the B_0 field drift), and motion-induced MSG encoded phase shift ϕ_m as follows:

$$\begin{cases} \phi_+ = \phi_0 + \phi_T + \phi_m \\ \phi_- = \phi_0 + \phi_T - \phi_m \end{cases} \qquad \text{Equ. 2.20}$$

Where ϕ_+ and ϕ_- are phase values acquired with MSG$+/-$, respectively. Hence, the motion-induced phase shift ϕ_m can be calculated by subtracting the two-phase images (Equ. 2.18), while the temperature dependent phase shift can be recovered by canceling out ϕ_m through averaging of both phase images:

$$\phi_0 + \phi_T = (\phi_+ + \phi_-)/2 \qquad \text{Equ. 2.21}$$

Equ. 2.18 and Equ. 2.21 are applied for the reconstruction of elasticity and temperature maps, respectively. In PRFS calculation (Equ. 2.10), the reference phase acquired before heating (ϕ_0) is subtracted to the current phase image ($\phi_0 + \phi_T$). Hence, the temperature dependent PRF phase shift ϕ_T can be estimated. Finally, both PRFS-based MRT and MRE can be processed from a regular gradient echo MRE sequence with MSG$+/-$ interleaved acquisitions without any additional acquisition. Those repeated high amplitude bipolar MSG gradients may induce eddy currents. For PRFS-based MRT, repeated bipolar gradients could make further global field drift during the acquisition. The field correction should be therefore used to remove that error induced by the field drift. Image artifacts caused by time varying gradients are expected to be compensated through active shielding.

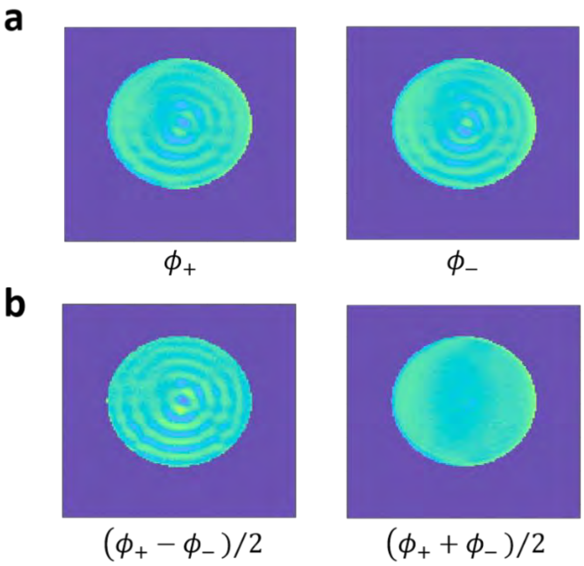

Figure 2.10 Simultaneous PRFS thermometry and MRE. Phase images ϕ_+ and ϕ_- acquired with opposed MSG polarities (a), and phase subtraction (ϕ_m) and summation ($\phi_0 + \phi_T$) images (b). By using this method, the background phase and PRF phase shift can be separated from the motion-induced phase shifts.

2.5 Interventional MRE/MRT in the ICube laboratory

This section describes the custom-made interventional MRE/MRT framework used for real-time monitoring during thermal therapies in the ICube laboratory.

Hardware set-up

This work was conducted in a 1.5 T open bore MRI (MAGNETOM Aera, Siemens Healthcare). All MR sequences developed in this thesis were modified using the Siemens IDEA sequence programming framework. As defined in the MRE pulse sequence code, the MR console generates an optical trigger signal for the mechanical wave to start. The time when that trigger is played during TR varies in order to adjust the MRE phase offset θ between the onset of the mechanical wave and the MSG; such phase offsets are typically evenly spaced over one cycle of the mechanical wave.

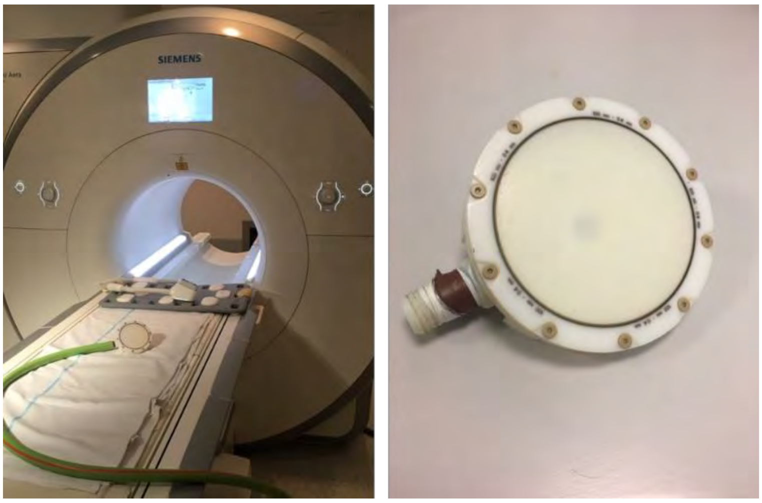

Figure 2.11 Left side: Custom-made MRE pneumatic MRE passive driver on the table of the 1.5 T MRI scanner (MAGNETOM Aera, Siemens). The mechanic exciter is connected to a subwoofer speaker with a plastic hose. Right side: detailed view of the 3D-printed pneumatic MRE passive driver.

The acoustic amplifier generates the wave once the trigger signal input is received. The pneumatic MRE passive driver was manufactured with bi-material polymer 3D printer (Figure 2.11). The MRI console was connected to a personal computer (a 64-bit window OS with a 2.5 GHz Intel dual-core i7 processor) for post-processing. As shown in Figure 2.12, all newly reconstructed phase and magnitude images are transferred from the MR console to the connected personal computer through TCP/IP connection. Received images are processed online with Matlab (Mathworks, Natick, USA).

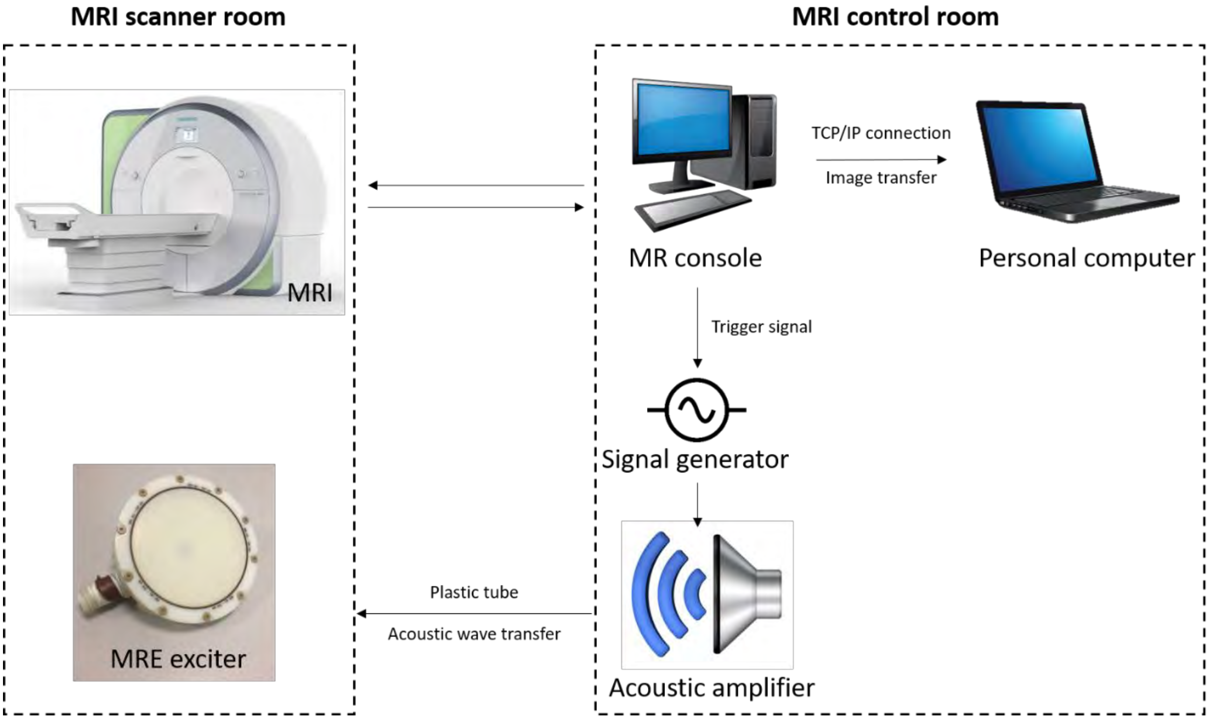

Figure 2.12 Diagram of the interventional MRE system.

MR sequence

All MRE sequences used in this Ph.D. study are based on a gradient recalled echo (GRE) MRE sequence. Typical GRE-MRE sequence have the MSG period equal to the period of the mechanical wave. To reduce both the acquisition time and the TE, we use fractional MRE encoding in order to increase the temporal resolution (Rump et al., 2007): the repetition time (TR) is equal to one period or two periods of the mechanical wave as shown in Figure 2.13. Fractional encoding consists in encoding the mechanical wave with an MSG with a frequency higher than the mechanical wave frequency; hence it becomes possible to use a TR equal to one mechanical period. Rump et al. (Rump et al., 2007) investigated that the encoding efficiency is determined by the ratio between the period of the MSG (f_g) and the mechanical wave (*f*). Their finding shows that the maximum efficiency occurs for $f \approx 0.82 f_g$. This fractional encoding method allows faster acquisition time by allowing fitting the whole acquisition of one line within one cycle of mechanical excitation.

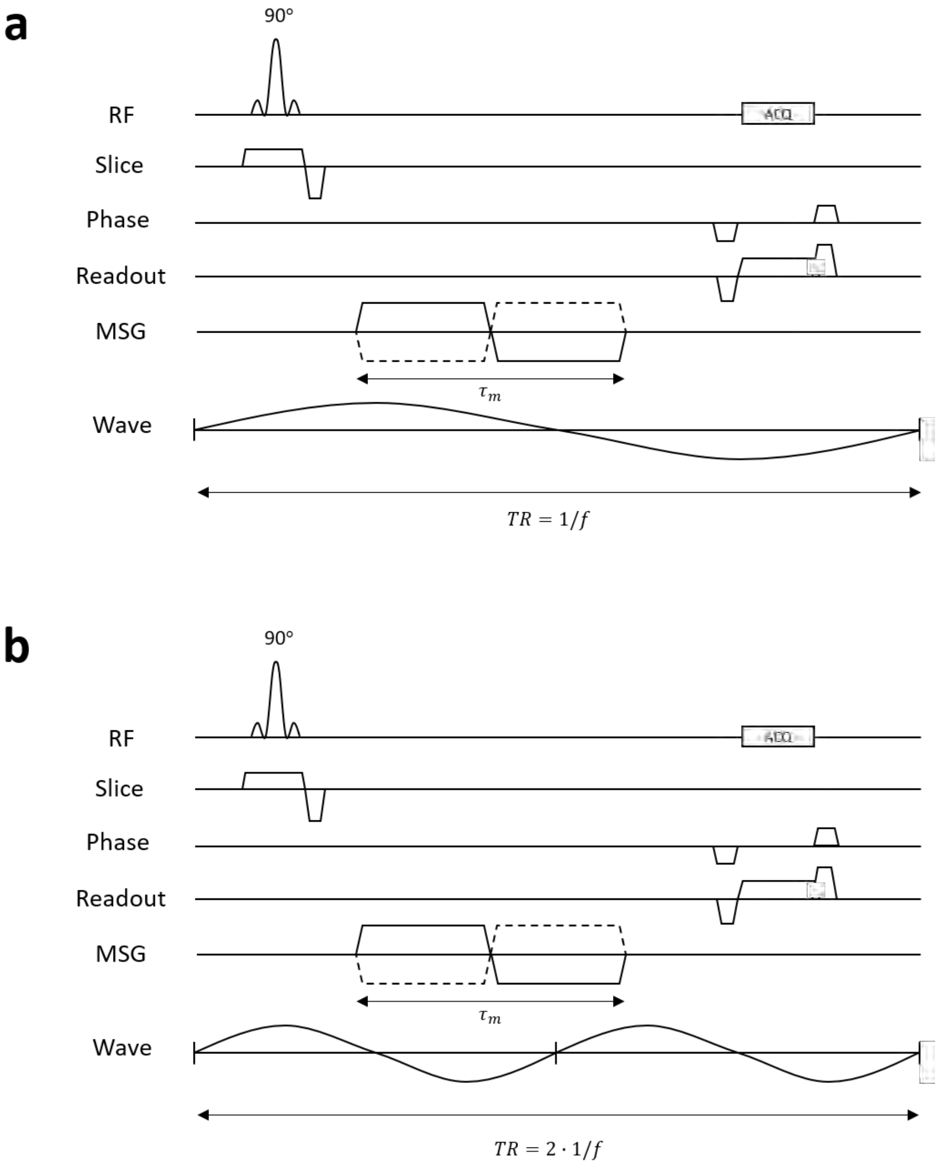

Figure 2.13 Chronogram of the fractional encoding GRE-MRE sequence developed for interventional MRE/MRT system. GRE 1-period MRE sequence (a) has TR period equal to the period of the mechanical wave. GRE 2-periods MRE sequence (b) has TR period equal to two periods of the mechanical wave. The motion is encoded in only one direction.

MSG$+/-$ interleaved images are acquired before the phase offset is shifted by the phase offset step $\Delta\theta$ (Figure 2.14). As previously mentioned, MRE reconstructions require a full dataset including different phase offsets between mechanical wave and the MSG. Subsequent elastogram can be reconstructed with every newly obtained pair of phase images with opposite MSG, i.e., using a sliding window approach (Corbin et al., 2016b). Therefore, PRFS temperature and elasticity maps can be updated simultaneously once a pair of phase images is obtained from the MR console through TCP/IP connection (Figure 2.12).

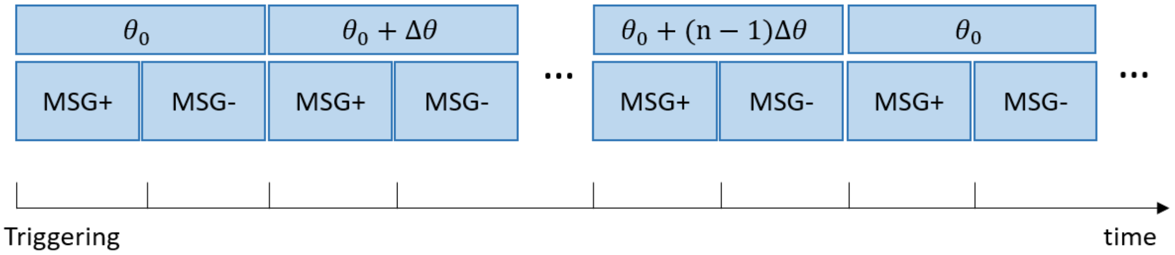

Figure 2.14 Image acquisition scheme. The phase offset is shifted by $\Delta\theta$ for the acquisition of each pair of MSG+/- phase images, until the maximum $(n-1)\cdot\Delta\theta$ is reached.

Chapter 3

3. Fast multislice MR Elastography and MR Thermometry using Simultaneous Echo Refocusing

Contents

3.1 Introduction

The MRE acquisition is inherently slow due to the high number of images acquired in order to reconstruct a single elastogram. The number of acquired images results from both the acquisition of images with several phase offsets between the mechanical wave and MSG, and the acquisition of two images per phase offset with opposite MSG polarities (MSG+/-) in order to double the PNR. In addition, specifically for GRE-MRE sequences, MSGs induce strong lengthening of the minimum TE, which results in a subsequent minimum TR increase hence increasing the acquisition time in GRE-MRE sequences. The "MRE" TR is also typically expressed as a multiple of the mechanical wave period in GRE MRE sequences. For example, with the typical 60 Hz mechanical wave frequency used in diagnostic MRE in the liver, the TR of GRE MRE sequences is equal to two mechanical periods (33.33 ms with a mechanical period of 16.67 ms). In other words, the minimum "GRE MRE" TR is both fixed by the minimum TE and the mechanical wave period.

The principle of fractional motion encoding was developed in order to use the MSG with higher frequency than the mechanical excitation frequency (Garteiser et al., 2013; Rump et al., 2007), so that the MSG period is shorter than the mechanical wave period and hence the related TE increase is reduced. In GRE-MRE sequence, fractional encoding can therefore shorten the acquisition time through a reduction of the minimum TR.

However, despite this acceleration technique, the acquisition time may still be too long in several applications. Several acceleration techniques have been developed in MRE. Recently, (Guenthner et al., 2019) proposed the Ristretto MRE acquisition scheme using a multislice GRE-MRE sequence with very high fractional encoding. It allows for having acceleration factor of 2 to 4.5 compared to conventional multislice GRE-MRE acquisition, at the expense of strongly decreased MSG encoding. Faster k-space readout strategies, such as echo-planar imaging (EPI) or spiral trajectories, have also been proposed for 3D MRE reconstruction (Guenthner and Kozerke, 2018; Shi et al., 2015). In addition, the simultaneous multislice (SMS) technique was proposed for multislice 3D coverage in brain MRE (Guenthner et al., 2017; Johnson et al., 2016). Recently, multiband RF pulse and controlled aliasing in parallel imaging (CAIPIRINHA) (Setsompop et al., 2011) was used to develop SMS-EPI MRE sequence (Sui et al., 2019). It allows for imaging the whole brain within 3.5 min with sufficient SNR for reconstructing the elastograms. Lastly, (Ebersole et al., 2018) introduced a new MRE reconstruction method from highly undersampled data. Like compressed sensing MRI, the proposed method has a sparsity data unique to MRE reconstruction according to the MSG polarity and phase offset. This undersampled data acquisition allows for having acceleration factor of up to 6.

Interventional MRE/MRT has sought to achieve high spatial coverage, which is key in properly monitoring the extent and effects of the ablation in both targeted and surrounding healthy tissue. The objective of this study is to introduce another acceleration option for multislice interventional MRE/MRT, through the use of simultaneous echo refocusing (SER) (Feinberg et al., 2002). The SER technique applies two consecutive RF excitation pulses and their respective slice selection gradients. Combined with adequate pre-dephasing readout gradients, two echoes, one per slice, can be sequentially acquired in a single image acquisition (Figure 3.1).

There are two main reasons for the use of the SER technique in our application: First, it enables to acquire MRE datasets with an acceleration factor of 2 without any higher fractional encoding. The RISTRETTO multi-slice GRE-MRE sequence employs a multi-shot approach in one mechanical wave period (Guenthner et al., 2019). It has led to high fractional encoding at the expense of sensitivity to motion. In contrast, the use of the SER technique can keep high motion sensitivity with an acceleration factor of 2. Second, as compared to the SMS technique using multiband RF pulse, the SER technique does not require any MR environment with additional coils (Borman et al., 2016; Johnson et al., 2016; Sui et al., 2019). Using additional RF coils that are necessary for SMS is always particularly challenging in an interventional MR environment.

The proposed sequence was evaluated in three experimental setups: first, SER-GRE was compared to standard GRE-MRE sequences in phantoms. Second, high intensity focused ultrasound (HIFU)-ablation was performed in a phantom to evaluate the potential of SER-GRE MRE/MRT for fast multislice monitoring. Third, similar experiments were conducted in ex-vivo tissue to evaluate the ability of monitoring the changes induced in biomechanical properties during HIFU ablation. These experiments aimed at evaluating whether the SER method could be used for the acceleration of multislice interventional MRE/MRT for the monitoring of thermal ablations.

3.2 Methods

3.2.1 Simultaneous Echo Refocusing (SER)

Feinberg et al. (Feinberg et al., 2002) first introduced multi-slice imaging technique in a single echo train, without multi-frequency RF excitation. In Figure 3.1, two consecutive excitation pulses and their respective slice selection gradients create magnetization in two non-contiguous slices. Adequate pre-dephasing readout gradients make it possible to sequentially acquire two echoes, one per slice. More specifically, gradients applied between the two RF pulses only affect the magnetization excited by the first RF pulse, while gradients applied after the second RF pulse affect both slices. Net area of readout pre-dephasing gradients corresponds to half and quarter of the area of the rephasing readout gradient, for echoes 2 and 1 (i.e. RF pulse 1 and 2), respectively. Thus, echo formations are generated at different times during the readout period (Feinberg et al., 2002) and slice 1 is acquired with a longer TE than slice 2.

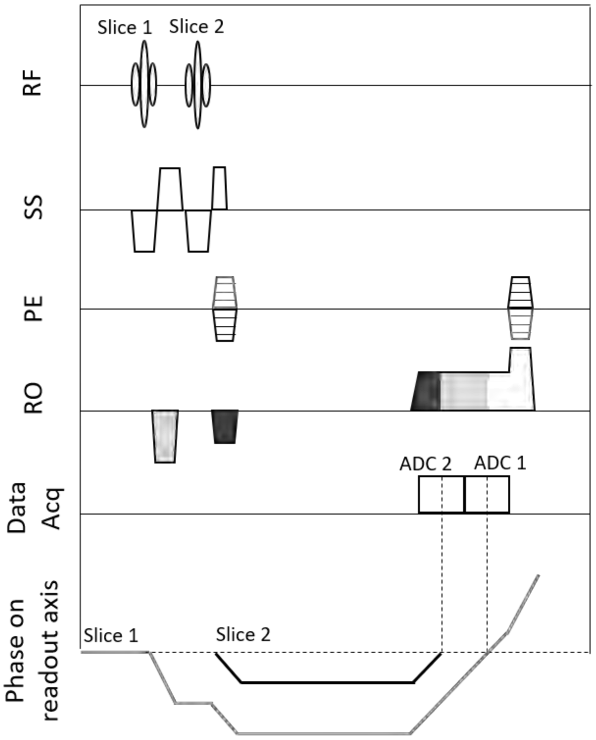

Figure 3.1 Multislice magnetization and phase status on readout direction. Net area of readout pre-dephasing gradients, colored in light/dark gray color, is equal to the net area of the rephasing readout gradient with light/dark gray color. ADC 1 and ADC 2 correspond to the acquisition of slices 1 and 2 excited by the first and second RF pulses, respectively. RF: RF excitation, SS: Slice Selection, PE: Phase Encode, RO: Readout, Data Acq: data acquisition.

This technique is of interest when long TE is sought for T_2/T_2^* weighting, but also more importantly when phase encoding gradients (diffusion, velocity encoding, etc.) strongly lengthen the "native" (i.e. regular one slice acquisition) minimum TE.

3.2.2 SER simultaneous MR Elastography and MR Thermometry

As shown in Figure 3.2b, the SER method was implemented in an MRE GRE sequence, so that 2 slices are acquired in a single TR, sharing a single MSG for mechanical wave encoding.

Experiments were conducted in a 1.5 T MR scanner (MAGNETOM Aera, Siemens Healthcare, Erlangen, Germany). A pneumatic exciter (Resoundant, Rochester, MN, USA) was used for mechanical wave generation, and was triggered to adjust the phase-offset (θ) between MSG and mechanical excitation. Two images with opposite polarities of MSG (MSG$+/-$) were obtained at each phase-offset. This pair of phase images was used for both MRE reconstruction (difference between phase images) and for PRFS thermometry (average between phase images) (Le et al., 2006) as detailed in Chapter 2.4. For MRE reconstruction, the filtered phase difference image was processed after temporal Fourier transform using a local frequency estimation based algorithm in order to estimate the local wavelength (Manduca et al., 1996). The shear modulus was then calculated by $\mu = \rho(\lambda f)^2$ under the assumption of linear elasticity and uniform tissue density (ρ=1000 kg/m^3) where f is the applied mechanical frequency.

PRFS-thermometry was calculated from the average of each pair of phase images, which contains temperature information but no wave information. In PRFS calculation, further phase addition images were subtracted from the references corresponding to the same phase offset (Figure 3.2b).

$$\Delta T = \frac{[\phi_p - \phi_p^0] - [\phi_{p,C} - \phi_{p,C}^0]}{\gamma \alpha B_0 TE} \qquad \text{Equ. 3.1}$$

Where ϕ_p and ϕ_p^0 are the current and reference phase images per phase-offset, respectively. For field drift correction, $\phi_{p,C}$ and $\phi_{p,C}^0$ are respectively the current and reference average values of phase measured in a non-heated region-of-interest (ROI) (Rieke and Pauly, 2008b). γ is the gyromagnetic ratio of the hydrogen nuclei, B_0 is the main magnetic field, α is the temperature coefficient (≈-0.01 ppm/°C), and TE is echo time across the selected slice.

3.2.3 Comparison experiment in a phantom

The first experiment consists in a comparison between SER-GRE MRE and two conventional GRE-MRE sequences with different levels of fractional encoding. Two GRE-MRE sequences with high and optimal fractional encoding, respectively, were used to study the tradeoff between motion encoding efficiency and acquisition time (Table 3.1). The GRE-MRE sequence with high fractional encoding (GRE 1-period) had a shorter TR equal to one acoustic wave period, while the GRE sequence with optimal fractional encoding (Rump et al., 2007) (GRE 2-periods) had a longer TR equal to two acoustic wave periods. In other words, the GRE 2-periods offers optimal MRE motion encoding at the cost of a two-time-longer acquisition time compared to the GRE 1-period, the latter resulting in lower motion encoding efficiency although it has a higher temporal resolution.

Table 3.1 MR acquisition parameters of GRE and SER-GRE MRE sequences

	TR (ms)	**TE (ms)**	**Vibration frequency (Hz)**	**MSG frequency (Hz)**	**Acquisition time for 2 slices (sec)**
GRE 1-period	8	6.26	125	220	1.24
GRE 2-periods	16	8.6	125	152	2.48
SER-GRE	16	8.6 (slice 2) /11.4 (slice 1)	125	152	1.24

FOV 300 mm × 300 mm, matrix 128×128, parallel imaging GRAPPA factor 2, partial Fourier 7/8, phase resolution 90 %, slice thickness 7 mm, read-out bandwidth 950 Hz/Px, Flip angle 15°, MRE encoding direction Readout, MRE phase offsets 4, amplitude of MSG 20 mT/m.

Spine coils and a 4-element surface coil were used. The pneumatic exciter was placed below the gel phantom (half-7% gelatin and half-9% gelatin) to generate acoustic waves at 125 Hz. Two slices were acquired with a slice gap of 100%. A total of 10 successive elastograms were reconstructed.

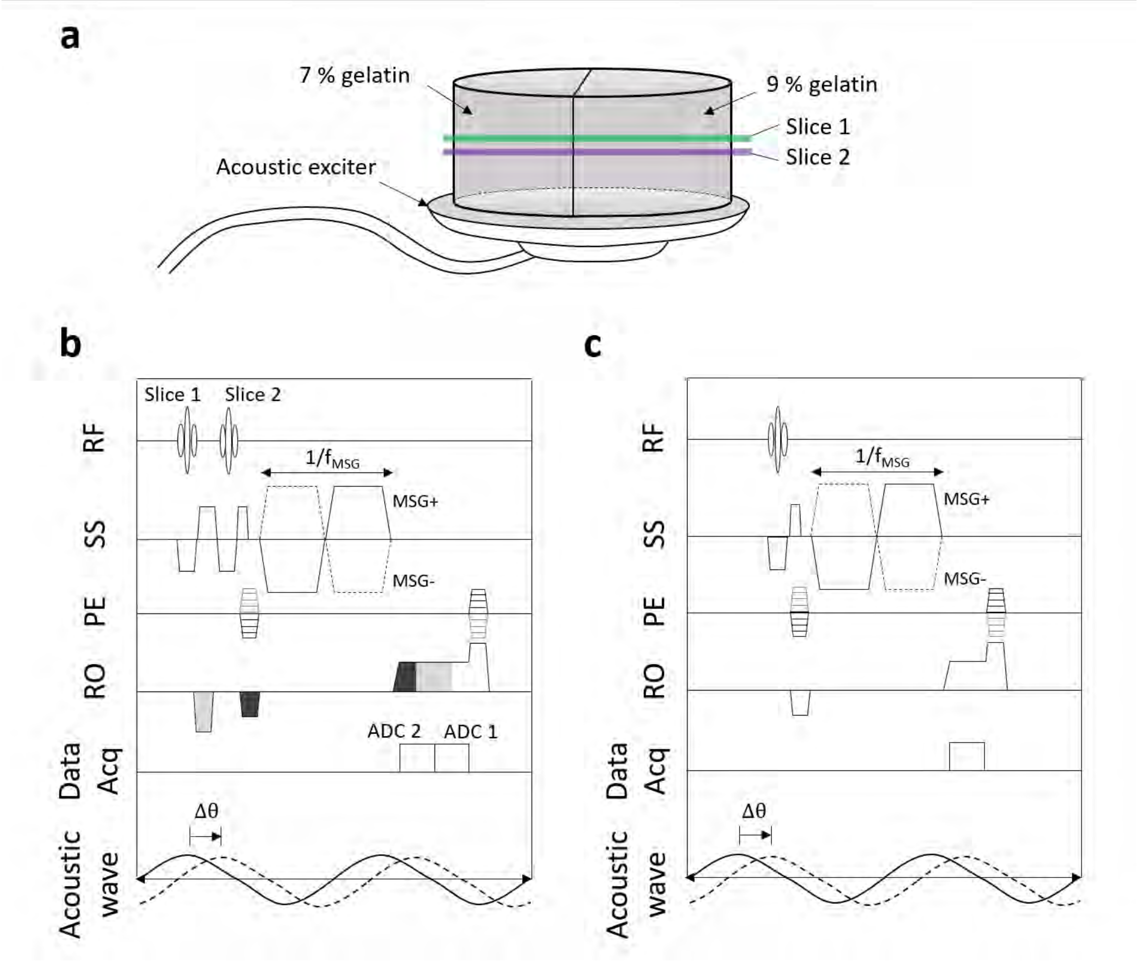

Figure 3.2 (a) Illustration of the gelatin phantom (left-7% and right-9% gelatin), (b) Chronogram of SER-GRE MRE and (c) GRE-MRE sequences, integrating MSG and time-harmonic motion generated by an external acoustic exciter. $1/f_{MSG}$ is the MSG period. $\Delta\theta$ is the step of phase-offset, spaced equally over a vibration cycle.

3.2.4 HIFU-ablation experiment in a phantom

To evaluate the ability of the SER-GRE sequence to monitor both temperature and elasticity, HIFU ablation was performed in an 8% gelatin-milk phantom (1.3% fat milk 1 L and water 1.4 L). The spin coil was used as the only receive coil in order to mimic the condition of the clinical MR-guided intervention (Sedaghat and Tuncali, 2018).

As shown in Figure 3.3, two interleaved acquisitions were employed to cover the whole volume of the focal spot with 4 contiguous slices. Each acquisition provided two slices with a slice gap of 100%, the two acquisitions being set-up one slice apart. The slice acquisition order was slice 3, 1, 4 and 2, with slices 1 and 2 acquired with TE 14.6 ms and slices 3 and 4 acquired with TE 11.1 ms. The 4 contiguous slices were positioned around the HIFU focal spot, positioned in slice 2. The temporal sequence of events in the experiment was defined as Rest 0-76 s, HIFU heating 77-256 s, and cooling 257-480 s.

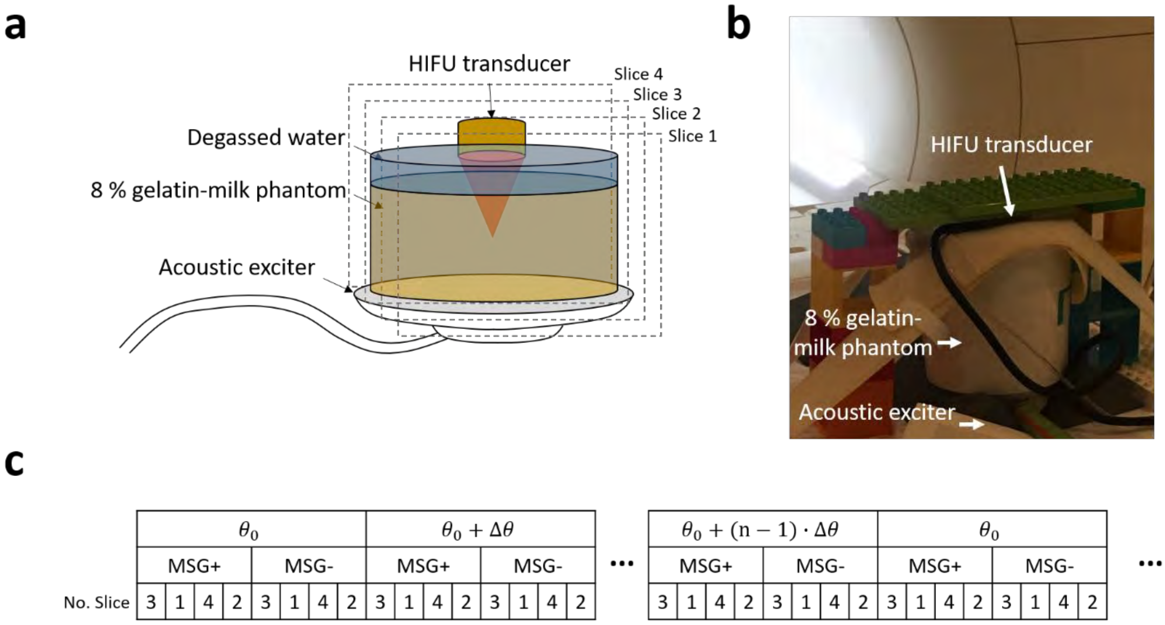

	θ_0								$\theta_0+\Delta\theta$									$\theta_0+(n-1)\cdot\Delta\theta$								θ_0								
	MSG+				MSG-				MSG+				MSG-				•••	MSG+				MSG-				MSG+				MSG-				•••
No. Slice	3	1	4	2	3	1	4	2	3	1	4	2	3	1	4	2		3	1	4	2	3	1	4	2	3	1	4	2	3	1	4	2	

Figure 3.3 (a-b) Illustration and photo of the experimental setup. Acoustic exciter is placed on the bottom of the phantom, and HIFU transducer is placed on the top, immersed in degassed water. (c) Image acquisition scheme. θ_0 is an initial phase-offset between MSG and mechanical wave. $\Delta\theta$ is the step of phase-offset, spaced equally over a vibration cycle. n is the number of phase-offset.

The SER-GRE MRE sequence was applied with parameters as follows: mechanical excitation frequency 100 Hz, MSG frequency 122 Hz, MSG amplitude 20 mT/m, MRE encoding direction Readout, 3 phase offsets for temporal Fourier transform, TR 20 ms, TE 14.6 ms/11.1 ms, FOV 350 mm × 350 mm, slice thickness 7 mm, 128 × 128 matrix size, Partial Fourier 7/8, Phase resolution 90 %, 15° flip angle and bandwidth 590 Hz/pixel. The acquisition time for 2 slices is 2 secs, i.e. the total acquisition time for all 4 slices is 4 secs. A HIFU ablation of power 220 W was operated with a single point.

3.2.5 HIFU-ablation experiment in ex-vivo chicken tissue

To monitor the changes in biomechanical properties with the SER-GRE MRE sequence, a HIFU ablation of power 150 W was performed in an 8% gelatin phantom containing a chicken breast sample. The same image acquisition as the previous HIFU experiment in a phantom was performed. As shown in Figure 3.4, all slices are sequentially obtained from the top of a chicken tissue and a HIFU target is defined between slices 2 and 3 (slice1: gelatin, slice 2: gelatin and tissue, slice 3: tissue, slice 4: tissue). The temporal sequence of events in the experiment was defined as Rest 2 min, HIFU heating 3 min, and cooling 8 min.

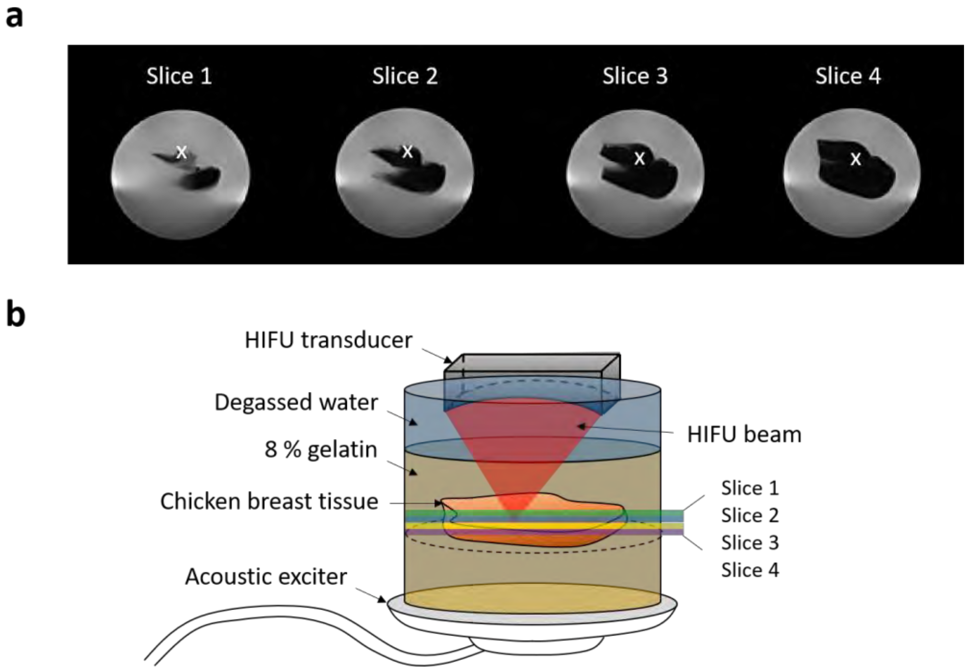

Figure 3.4 (a) T_2-weighted BLADE images before HIFU ablation, (b) scheme of the experimental setup. White-x symbols show the location of the HIFU focus (slice1: gelatin, slice 2: gelatin and tissue, slice 3: tissue, slice 4: tissue).

The SER-GRE MRE sequence was applied with parameters as follows: mechanical excitation frequency 125 Hz, MSG frequency 152 Hz, MSG amplitude 23 mT/m, 3 MRE phase offsets (θ) for temporal Fourier transform, Slice selection MSG encoding direction, TR 16 ms, TE 13.5 ms/10.2 ms, FOV 350 mm × 350 mm, thickness 6 mm, matrix 128 × 128, 15° flip angle and bandwidth = 690 Hz/pixel. The acquisition time for 2 slices is 2048 ms, i.e. the acquisition time for all 4 slices is 4096 ms. T_2-weighted images were acquired for the evaluation of HIFU ablations, using a turbo spin-echo sequence with BLADE acquisition. Parameters are used as follows: TR 2000 ms, TE 179 ms, Echo train length 58, FOV 350 mm × 350 mm, slice thickness 6 mm, matrix 192 × 192, 121° flip angle, and bandwidth = 605 Hz/pixel.

3.3 Results

3.3.1 Comparison experiment in a phantom

Figure 3.5 shows elastograms obtained with the SER-GRE MRE sequence and the 1- and 2-period GRE MRE sequences. In the case of the SER-GRE sequence, slices 1 and 2 were obtained with TE = 11.4 / 8.6 ms, respectively. The 2 different halves of the gel can be distinguished through their stiffness in both slices for all three acquisition schemes.

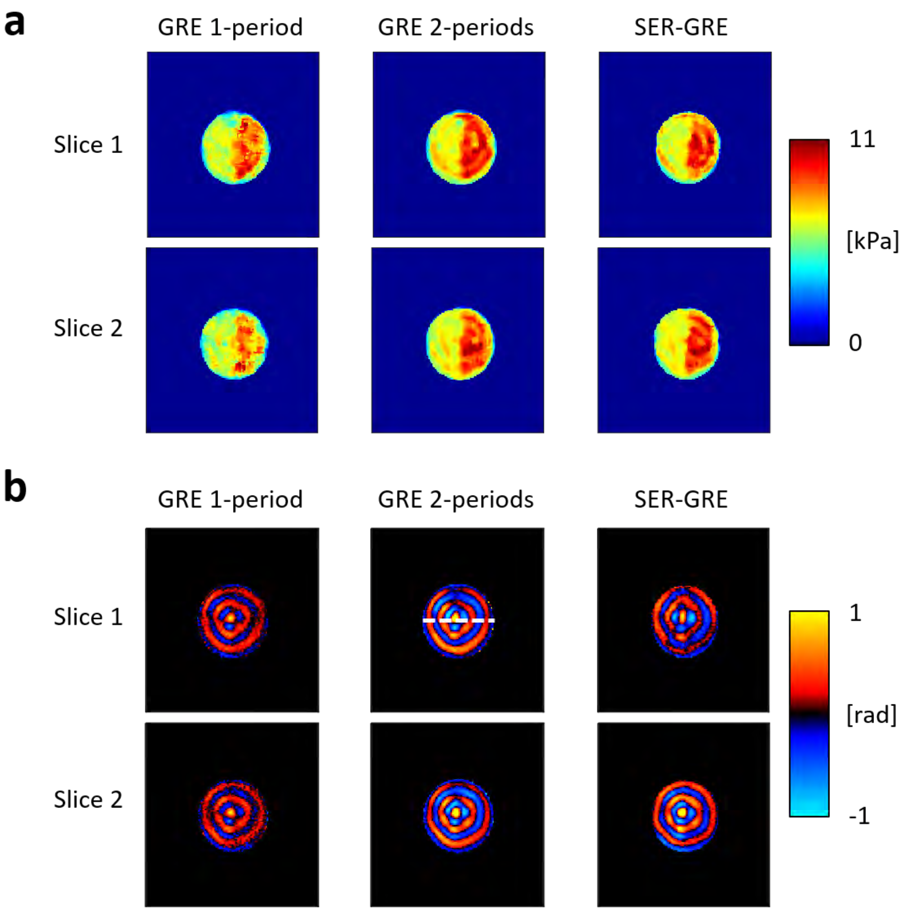

Figure 3.5 (a) Elastograms and (b) phase difference image (phase-offset #1) in slices 1 and 2 obtained from GRE and SER-GRE sequences on measurement #2. The difference of shear modulus in 7% and 9% gelatin parts are visible, as reflected by differences in wavelength.

The mean and standard deviation of the shear modulus in ROIs 1 and 2 for all 10 measurements are shown in Table 3.2.

Table 3.2 Mean and standard deviation of the shear modulus in 7% and 9% gelatin parts.

	7% gelatin		**9% gelatin**	
	Slice 1	**Slice 2**	**Slice 1**	**Slice 2**
GRE 1-period	6.2±0.7 kPa	6.1±0.9 kPa	8.2±1.3 kPa	7.6±1.4 kPa
GRE 2-periods	6.7±0.7 kPa	6.6±0.8 kPa	8.9±1.2 kPa	8.7±1.2 kPa
SER-GRE	6.3±1.0 kPa	6.5±0.9 kPa	8.6±1.5 kPa	8.7±1.4 kPa

Figure 3.6 shows the horizontal centerline profiles (1-pixel width, averaged across 4 phase difference images with phase offset #1) of the phase difference images acquired in slices 1 and 2 with all three acquisition sequences. This line is represented in Figure 3.5b, GRE 2-periods, Slice 1. As expected, the phase motion encoding of SER-GRE and GRE 2-periods are similar and higher than the one of the GRE-1 period sequence.

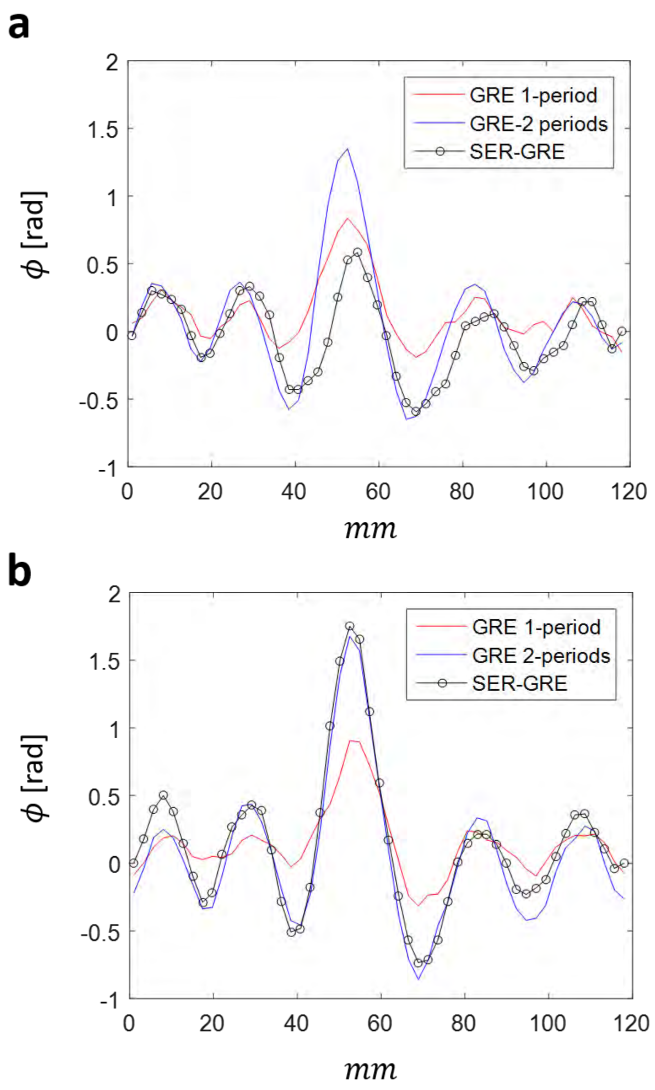

Figure 3.6 Horizontal centerline profiles of phase difference image in slices 1 (a) and 2 (b) (Figure 3.5-white dashed line). In the case of the SER-GRE, slices 1 and 2 are acquired with different echo times (slice 1: 11.4 ms, slice 2: 8.6 ms).

A Bland-Altman analysis was plotted to evaluate agreement with the GRE-2 period sequence, defined as the gold standard (Figure 3.7). The mean of the shear modulus of each measurement was used for the analysis. The difference of shear modulus between GRE 1-period and GRE 2-periods was found to be -0.3±0.2 kPa / -0.7±0.4 kPa (region 1 /region 2) in slice 1 and -0.4±0.1 kPa / -1.2±0.3 kPa (region 1 /region 2) in slice 2. The difference between SER-GRE and GRE 2-periods was found to be -0.4±0.1 kPa / -0.5±0.3 kPa (region 1 /region 2) in slice 1 and 0±0.03 kPa / 0.1±0.1 kPa (region 1 /region 2) in slice 2.

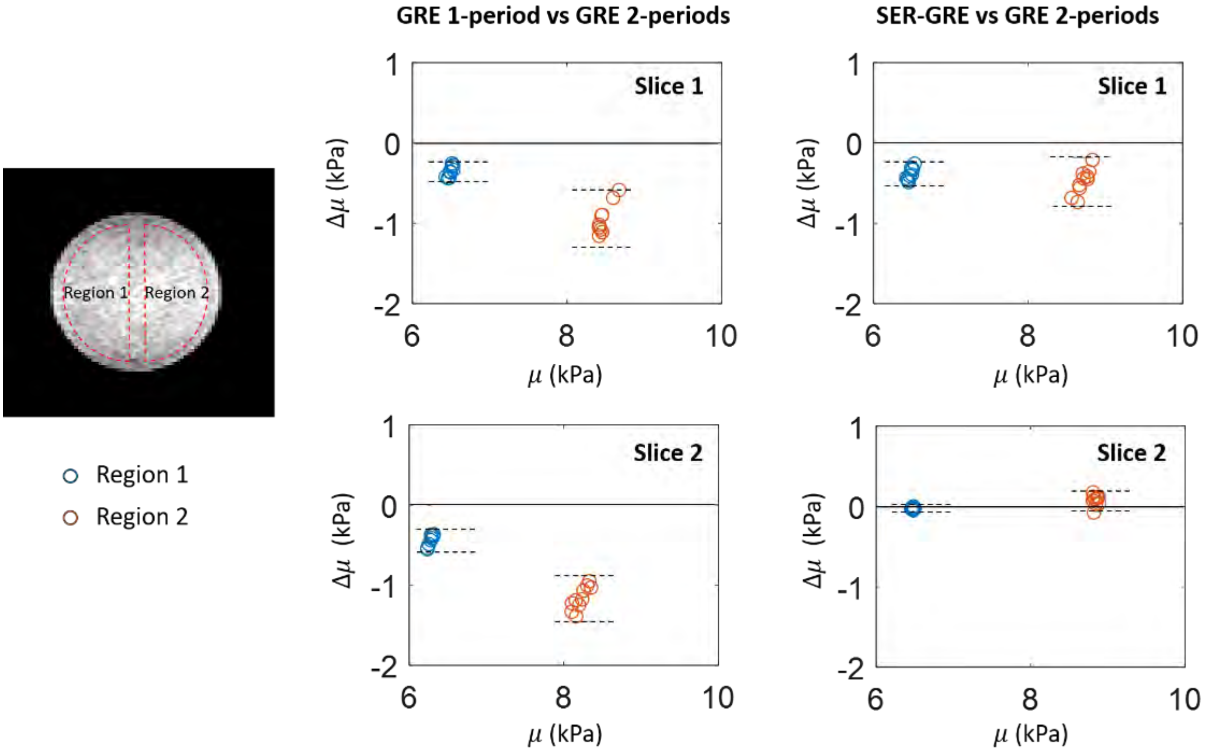

Figure 3.7 For comparison with GRE 2-periods, Bland-Altman plots obtained using the average of the shear modulus of each measurement in 7% gelatin (region 1) and 9 % gelatin parts (region 2). The mean 95 % confidence interval for $\Delta\mu$ is plotted as a dashed line.

The SER method allows two slices to have different TE values, which means each slice has different SNR. The SNR is proportional to PNR that can directly affect the noise of the displacement image. Figure 3.6 shows that the displacement of slice 2 (TE: 8.6 ms) is in better agreement with that of GRE-2 period than that of slice 1 (TE: 11.4 ms).

The PNR is proportional to TE and the tissue-dependent T_2* relaxation time (Guenthner and Kozerke, 2018).

$$PNR \propto e^{-\frac{\Delta TE}{T_2^*}} \cdot \frac{\phi}{\pi} \qquad \text{Equ. 3.2}$$

Where ϕ denotes the encoded motion phase (radian) and ΔTE is the echo time. The slice excited by the first RF pulse has a lower PNR value than the slice excited by the second RF pulse that has a shorter TE. For example, if a SER GRE sequence is used for liver imaging (T_2* of normal liver= ~20 ms (Anderson et al., 2001)) and echo time difference between the two slices ΔTE = ~3.5 ms, PNR of the slice by the first RF excitation would be 84 % of the PNR of the slice acquired with the second RF pulse and shorter TE. Therefore, for further experiments in certain organs, the selection of TE and readout bandwidth should take T_2* values into consideration.

In Figure 3.6, the SER GRE displacement profile in slice 2 (TE: 8.6 ms) appears to be in better agreement with the one of GRE-2 periods, when compared to the ones in slice 1 (TE: 11.4 ms). However, this decrease in SNR in one slice due to its longer TE may have a limited effect on elasticity estimates, as the LFE algorithm estimates the spatial periodicity of the displacement profile. In contrast, low phase encoding efficiency with high fractional encoding (GRE 1-period) results in much noise in the displacement image (phase difference), and in poor wave-to-noise ratio, which is directly linked to the quality of elastogram (Figure 3.5). In MRE, poor PNR is acceptable as long as wave to noise ratio is high enough for proper elasticity estimation with LFE. In other words, high fractional encoding allows decreasing TE, at the expense of wave encoding. Inversely, optimal fractional encoding allows high wave to noise, at the expense of longer TE. In our phantom experiments, the latter case was clearly better, as seen by the fact that SER-MRE outperformed 1-period GRE-MRE in terms of wave to noise ratio.

3.3.2 HIFU-ablation experiment in a phantom

In Figure 3.8, the changes in temperature (ΔT) are clearly visible in all 4 slices. The focal spot appears to be located in slice 2 and the effect of heat diffusion is observed in slices 1, 3, and 4. Corresponding changes in shear modulus (μ and $\Delta\mu$) and wave are found in the 4 contiguous slices. $\Delta\mu$ corresponds to the elasticity difference compared to the reference image acquired before heating. The first elastogram and temperature map were reconstructed 24 s after MR acquisition started and used as the reference. Both elastogram and temperature map can be then updated every 8 s based on the sliding window scheme (Corbin et al., 2016b).

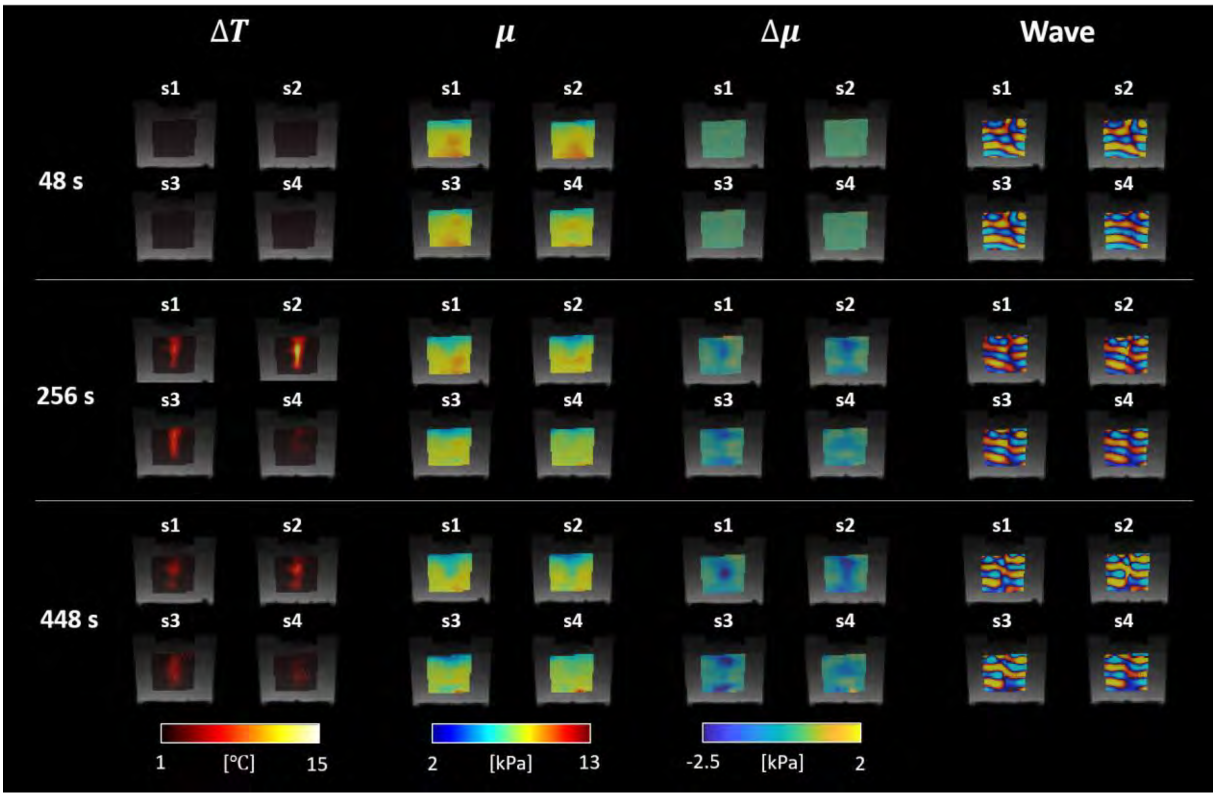

Figure 3.8 Results of HIFU ablation in the phantom. From left to right, ΔT, μ, $\Delta\mu$ and wave images overlaid with the magnitude image, before (time 48 s), after the HIFU shot (time 256 s) and during the cooling time (time 448 s). s1-4 in the figure correspond to slices 1 to 4, respectively. Temperature maps showed a local temperature increase resulting from the HIFU heating. Corresponding changes in shear modulus ($\Delta\mu$) were observed in the heated zone, corresponding to wavelength decreasing locally.

Figure 3.9 shows time-dependent profiles of ΔT, μ, and $\Delta\mu$ calculated by averaging within an ROI of 2×7 pixels, selected around the focal spot. The temperature was found to increase by about 7 ℃, 12 ℃, 7 ℃, and 2 ℃ in slices 1 to 4 respectively, at the end of HIFU heating (peak temperatures). This led to gel softening in which shear modulus decreased by 1.1 kPa, 1.9 kPa, 1.1 kPa, and 0.7 kPa from an initial shear modulus of about 8 kPa, 8.5 kPa, 8.7 kPa, and 8 kPa, in slices 1 to 4, respectively. After HIFU heating, shear modulus continued decreasing down to 6.0 kPa, 5.9 kPa, 6.6 kPa, and 6.6 kPa (448 s) until a steady state was reached. The shear modulus in the 4 slices had different dynamic behaviors over time (Figure 3.9). The elasticity in slice 2 started to decease first since the focal spot was centered in slice 2. In slice 4, the effect of HIFU ablation on elasticity appeared about 132 s after HIFU heating started since it was about 14 mm away from the focal spot.

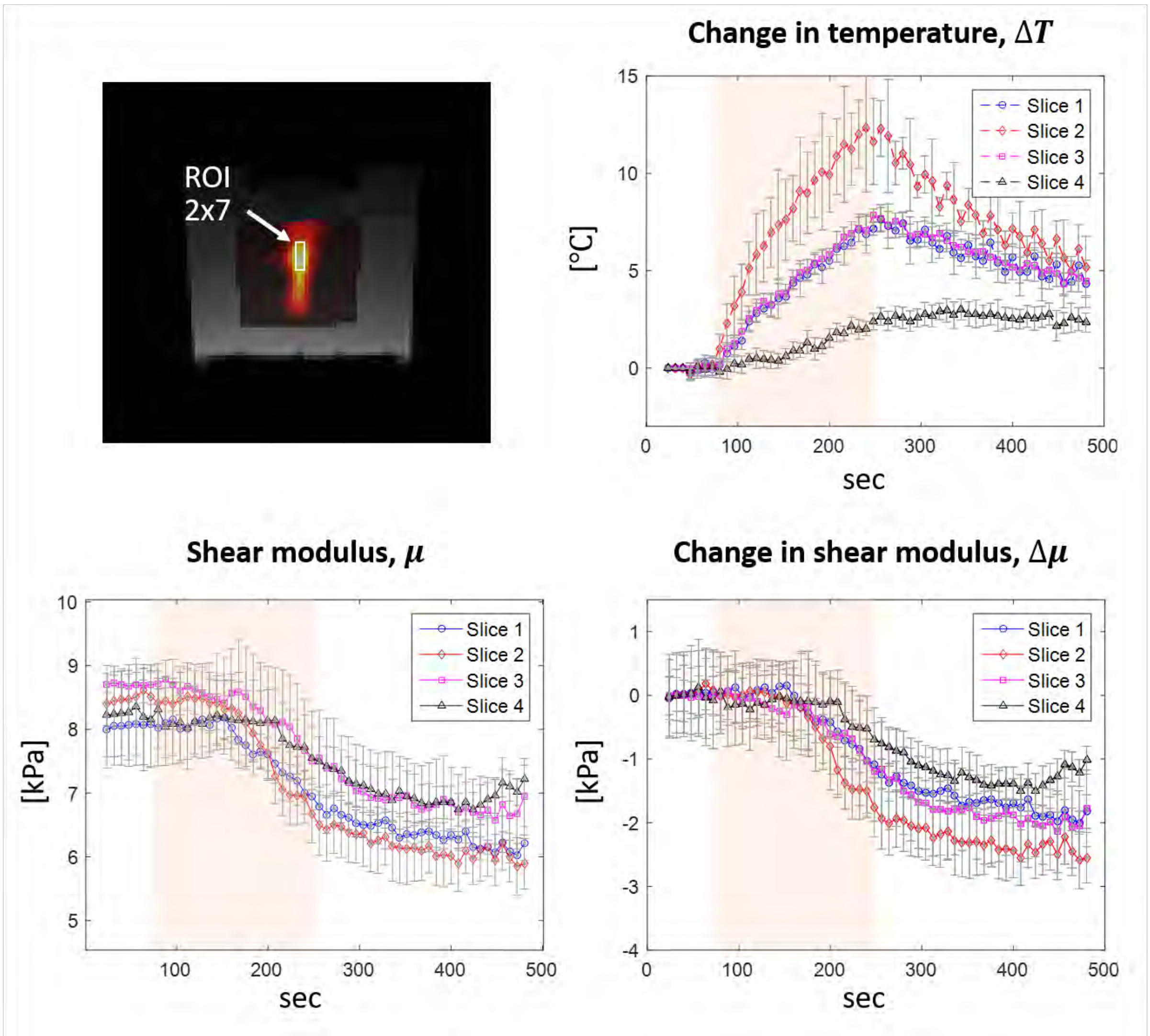

Figure 3.9 Time-dependent profiles of ΔT, μ, and $\Delta\mu$ calculated by averaged value within an ROI of 2×7 pixels. The ROI is depicted in the temperature map of slice 2 at 256 s (top left). The faded red color in three plots represents the HIFU heating phase.

Gel-softening first occurred in slices 1-3, while shear modulus in slice 4 started to decrease after a few seconds. This delay was most certainly due to thermal diffusion, as slice 4 is the furthest one from the focus. Furthermore, this experiment was designed to be realistic compared to MR-guided interventions in terms of RF coils: no additional RF receive coils were used. Despite this restriction, it was shown that monitoring tissue elasticity and temperature continuously in 4 contiguous slices was possible using the SER-MRE sequence.

3.3.3 HIFU-ablation experiment in ex-vivo chicken tissue

Figure 3.10 illustrates temperature and elasticity maps obtained in 4 contiguous slices after HIFU heating ended (300 s). The focal spot was supposed to be centered between slices 2 and 3, however, heat-affected zones are visible in 4 slices as shown in Figure 3.10a. The first elastogram was reconstructed 24.5 s after MR acquisition started, and then updated every 8.2 s based on the sliding window scheme. Similarly, temperature maps were displayed every 8.2 s after acquiring the reference phase image.

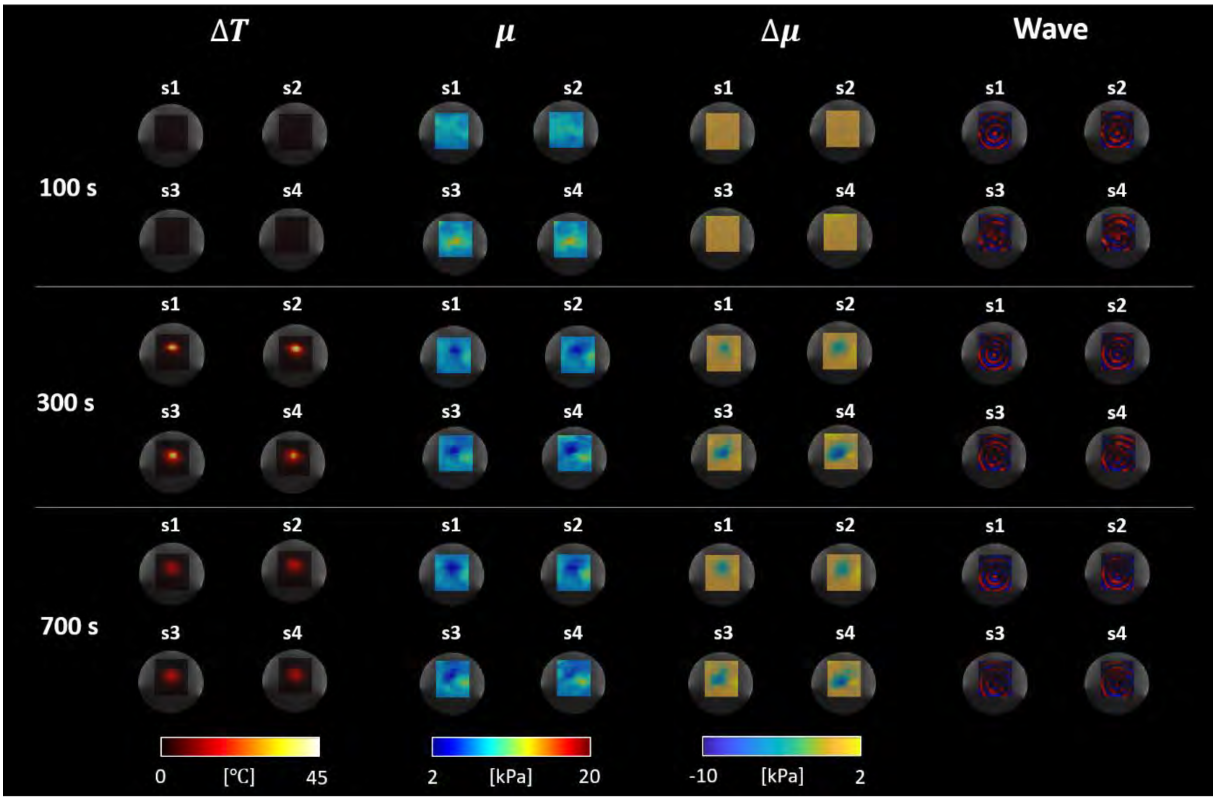

Figure 3.10 Results of HIFU ablation in ex-vivo chicken tissue. From left to right, ΔT, μ, $\Delta\mu$ and wave images overlaid with the magnitude image, before (time 100 s), after the HIFU shot (time 300 s) and during the cooling time (time 700 s). s1-4 in the figure correspond to slices 1 to 4, respectively. Temperature maps showed a local temperature increase resulting from the HIFU heating. Corresponding changes in shear modulus ($\Delta\mu$) were observed in the heated zone, corresponding to local wavelength decrease.

As shown in Figure 3.11, the profiles of shear modulus (μ) and temperature change (ΔT) are calculated through averaging value within an ROI of 2 x 2 pixels, selected at the center of the focal spot. Before heating, the shear modulus was measured to 8.6±0.3 kPa, 8.1±0.1 kPa, 11.6±1.3 kPa, 13.0±1.4 kPa for slices 1 to 4 respectively. At the end of heating, shear modulus decreased to 4.1±0.1 kPa, 4.0±0.2 kPa, 4.3±0.3 kPa, 4.9±0.8 kPa for a temperature increase ΔT of 32°C to 46°C, and then after cooling down, the shear modulus reached 3.6±1.3 kPa, 3.6±1.7 kPa, 4.4±0.8 kPa, 8.2±1.5 kPa for slices 1 to 4 respectively.

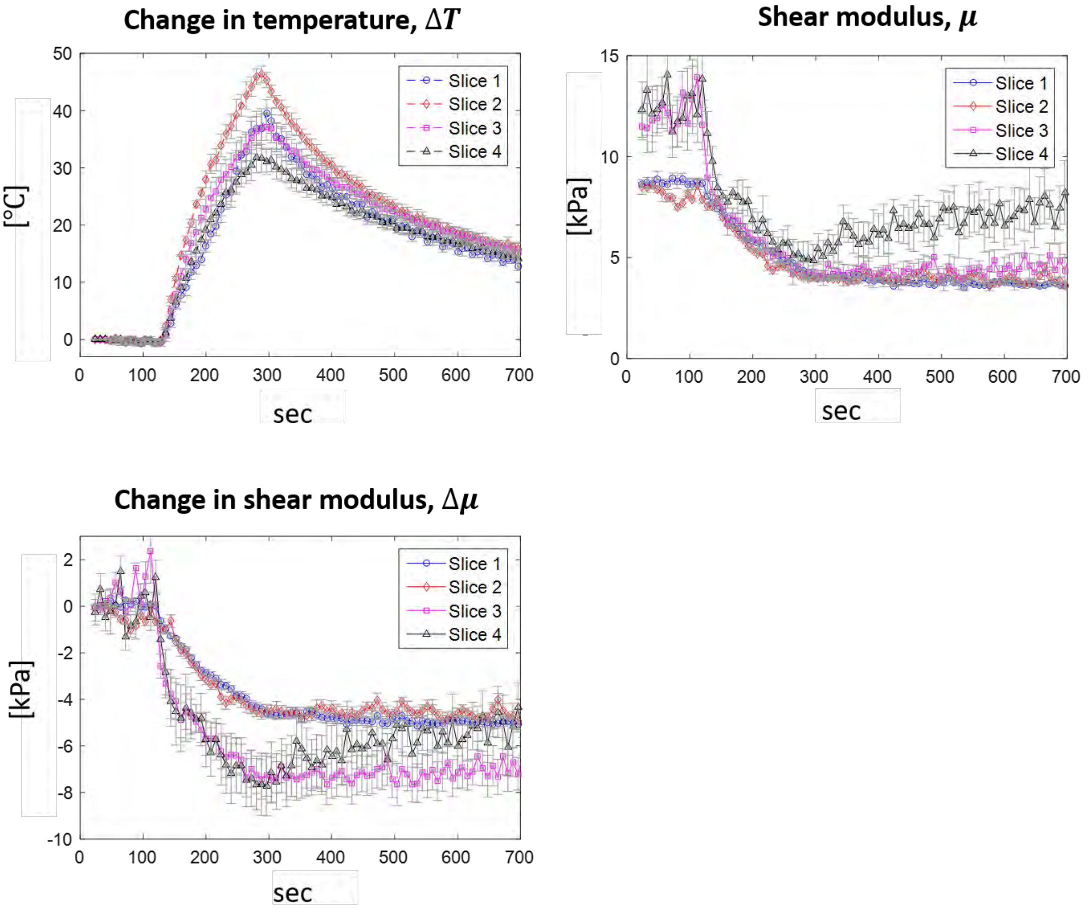

Figure 3.11 Time-dependent profiles of ΔT, μ, and $\Delta\mu$ calculated by averaged value within an ROI of 2×2 pixels as shown in Figure 3.4a.

The observed tissue softening during heating could be explained by reversible protein denaturation during heating, as already observed in vitro in muscle tissue (Wu et al., 2001). However, this phenomenon has been observed at low temperature elevation, which is not the case here. An explanation of the results reported here is that we measured changes of elasticity in voxels containing chicken and gelatin. This is clearly visible in slices 1 and 2, in which the shear modulus seems to be predominantly changed by gel-softening, with an irreversible softening. The shear modulus in slices 3 and 4 seems to increase back after HIFU heating, suggesting this could be due to predominant contribution of chicken tissue in the global response. Additional experiments would be needed to fully understand these observations. However, from a methodological point-of-view, we showed it was feasible to measure elasticity and temperature changes in 4 contiguous slices using the proposed SER MRE/MRT method.

3.4 Discussion

This study proposes the use of the SER method as an acceleration means for multi-slice interventional MRE/MRT monitoring of thermal ablations. As previously mentioned, GRE MRE sequence with EPI can be used for fast multislice acquisition. However, the increased echo train length and TE result in a decrease in SNR that can have an impact on the quality of the elastogram (Weidensteiner et al., 2003). Spiral readout acquisition has also received much interest in 3D imaging but still remains difficult to implement because the reconstruction depends upon gradient performance (Fielden et al., 2018). Another approach is the use of parallel imaging with simultaneous multislice excitation (SMS) (Breuer et al., 2005; Feinberg and Setsompop, 2013; Larkman et al., 2001; Setsompop et al., 2011; Zhang et al., 2015). SMS combined with sensitivity-encoding (SENSE) has been investigated for PRFS thermometry. Borman et al (Borman et al., 2016) evaluated temperature measurement of SENSE, SMS, and SMS/SENSE and concluded that SMS with the acceleration factor 2 was comparable to the reference measurement. However, the SMS method is potentially limited by the g-factor that depends on the number and location of coils. Currently, most MR-guided interventions are conducted with limited additional coils and rely on the built-in-spine coils only or the body coils. The g-factor is hence high for parallel imaging, and certainly too high for the SMS method (Borman et al., 2016; Sedaghat and Tuncali, 2018). Additionally, this limitation is even more critical in interventional MRE because the mechanical driver adds further spatial constraints. In this situation, GRE MRE sequence combined with the SER method holds potential for accelerated multislice MRE/MRT acquisition. The SER GRE MRE sequence brings the same temporal resolution as the GRE 1-period sequence while allowing for optimal wave to noise ratio similar to the GRE 2-period acquisition.

A major limitation of the SER method may be that the slice-selection gradients of the second RF excitation (for slice 2 - Figure 3.2b) could have an MSG-like effect as it could encode motion into phase images obtained with ADC1 in Figure 3.2b. However, this effect should not impact temperature estimates: in PRFS calculation, phase-added images are subtracted from the references corresponding to the same phase-offset (Figure 3.1). Therefore, motion-induced phase errors in phase-added images can be canceled by this difference with respect to the reference images bearing the same errors.

Finally, partial volume effects are a well-known problem in all kind of thermal ablations, and particularly in HIFU ablations, which justifies the need for multislice acquisitions. This preliminary study has shown that the SER method holds potential for being a good accelerating option in interventional MRE sequences. The SER-GRE MRE sequence enables to acquire elastograms and temperature maps of contiguous slices, within a shorter acquisition time than regular GRE-MRE sequences as well as keeping good sensitivity to motion. Two slices are acquired within each single TR, sharing a single MSG to encode the mechanical motion. Thus, it is feasible to monitor simultaneously the wave propagation and temperature changes in different slices. This technique will provide another acceleration option for fast multislice acquisition in MR-guided interventions.

In this chapter, 4 contiguous slices can be acquired using two interleaved acquisitions. However, alternative strategy should be investigated if more than 4 slices are required. For example, the SMS technique can be used with the SER technique in order to acquire 4 slices in a single TR period. Alternatively, a third RF pulse and a third echo can be added in the sequence, but further study should be led to find out the effect of TE difference across 3 slices on temperature maps.

Chapter 4

4. Simultaneous fat referenced PRFS Thermometry and MR Elastography

Contents

4.1 Introduction

MR Thermometry based on the Proton Resonance Frequency Shift (PRFS) is the most commonly used method for the monitoring of thermal therapies because it offers high temperature sensitivity within the temperature range of interest and allows fast acquisitions in the order of a few seconds (Rosenberg et al., 2013).

4.1.1 Limits of PRFS MR Thermometry

Fundamental limitations of PRFS thermometry need to be considered when applying this method for thermal ablation monitoring. First, PRFS temperature information provides temperature changes through the difference between the current phase and a baseline phase image. Hence, time-varying field drift and motion between successive scans can result in temperature errors, if not corrected for. Second, PRFS provides an instantaneous parameter, namely, temperature changes, which does not directly relate to tissue damage. The cumulative thermal dose (TD) represents an integration of temperature over time and has been shown to be a reliable marker of tissue damage (Sapareto and Dewey, 1984). However, fundamental limitations when using TD alone for monitoring thermal ablations over time need to be mentioned, such as the fact that TD thresholds are tissue-dependent (van Rhoon et al., 2013), and that TD is particularly sensitive to any uncertainty or bias due to its cumulative property (Vappou et al., 2018). TD has also been shown to be poorly correlated to non-perfused volume (NPV), a reliable marker of post-ablation tissue damage, showing potential errors of MR Thermometry due to long-term heat accrual (Bitton et al., 2016). Third, PRFS thermometry in fat-containing tissues may result in significant temperature errors depending on echo time, fat fraction, and extent of temperature increase because the temperature dependent electron-screening constant in fat is negligible compared to the one of water protons (Rieke and Pauly, 2008a; Taylor et al., 2011).

4.1.2 State of the art of temperature mapping using water/fat separation

The PRFS method using chemical shift water/fat separation has been investigated to tackle some of these limitations (Hofstetter et al., 2012; Lam et al., 2015; Soher et al., 2010; Taylor et al., 2008; Wyatt et al., 2010). Table 4.1 summarizes previous works for temperature mapping with the use of water/fat separation. The first improvement is that water-fat separation makes it possible to measure the temperature-induced PRFS from the phase of the water fraction, and no longer from the global phase of mixed water and fat protons in fatty tissues.

Signal models for water/fat separation must be carefully chosen to avoid inaccurate quantification of fat (Yu et al., 2008). Several fat peaks are present within the spectrum of living tissues.

These fat spectral peaks are present in the spectrum from 0.9 to 5.3 ppm, and they differ from the water peak at 4.7 ppm. Fat and water also differ in terms of T2 decay. Hence in tissues with both fat and water components, the actual T_2 decay can be modelled with a double exponential decay reflecting both the decays of fat and water.

As reported in a comparative study (Hernando et al., 2010), there are clear trade-offs between the choices of the model: (1) a single peak vs. multipeak fat model and (2) no decay vs. a single decay (R_2^*) vs. two decay model ($R_{2,w}^*$, $R_{2,f}^*$). A multi-peak spectral fat model is generally superior to a single-peak fat model although the simplified 6-peak fat model cannot completely describe the complex nature of fat signal.

A single decay model, matching the decay of the main component, leads to a stable estimate although the model does not closely match the actual 2-component decay. In contrast, a two-decay model allows a more accurate estimate but increases the noise sensitivity. Hernando et al. (Hernando et al., 2010) suggested that a single-decay model performed best in the case of low SNR or fat fraction close to 0 % or 100 %, while a two-decay model is more appropriate for high SNR or fat fraction close to 50 %. Taylor et al. (Taylor et al., 2008) exploited an iterative Steiglitz-McBride (SM) algorithm to find the frequency of water and fat signals (single fat peak) and their respective T_2* values. Lam et al (Lam et al., 2015) introduced another model to directly obtain the frequency difference between water and fat for temperature calculation. It therefore allowed avoiding phase wrapping, which causes discontinuities in the phase image. Their approach also provided T_2* values of water and fat.

Wyatt et al. (Wyatt et al., 2010) proposed to use fixed values for the complex amplitude of water and fat signals (ρ_w, ρ_f) as determined via a pre-scan before heating; ΔT and ψ were then estimated by the fitting algorithm. Fat-Referenced PRFS MR thermometry (FRPRFS) was also proposed using water-fat separation with multi-peak fat model but no T_2^* decay (Hofstetter et al., 2012; Soher et al., 2010). Time-varying field drifts can be estimated from the phase of the fat fraction because, as previously mentioned, temperature induced changes are negligible in fat. While the approach from Soher et al. could only correct for field drift in fat containing tissues, Hofstetter et al. extended this correction to all tissues through the calculation of the global field correction map fitted to the phase of fat in fat containing tissues. Hence, water proton only PRFS temperature estimation can be obtained while correcting for time-varying field drifts in all soft tissues (Hofstetter et al., 2012).

Table 4.1 Comparison between different studies for temperature mapping using chemical shift water-fat separation. With t: echo time, ρ_w : the complex-valued water signal, ρ_f : the complex-valued fat signal, ω_w: the angular frequency of water signal, ω_f: the angular frequency of fat signal (p is multipeak fat frequencies), $R^*_{2,w}$: relaxation rates of T_2^* of water, $R^*_{2,f}$: relaxation rates of T_2^* of fat, ψ: off-resonant precession, ΔT: temperature change, α: the electron screening thermal coefficient, $\Delta f(T)$: frequency difference between water and fat signal according to temperature. MGRE: multi gradient recalled echo sequence.

Author	**Lists**	**Contents**
(Taylor et al., 2008)	Type of thermometry	Fat referenced
	Signal model	$S(t) = \rho_w e^{-R^*_{2,w}\cdot t} e^{-i\omega_w \cdot t} + \rho_f e^{-R^*_{2,f}\cdot t} e^{-i\omega_f \cdot t}$
	Unknown parameter	$\rho_w, \rho_f, \omega_w, \omega_f, R^*_{2,w}, R^*_{2,f}$
	Pre-scan required?	No
	Fat peak spectrum /R2* decay	single-/multi-
	Sequence/TR/TE	MGRE/68 ms/3 ms; 16 echos, ΔTE = 3.5 ms
(Wyatt et al., 2010)	Type of thermometry	Reference less
	Signal model	$S(t) = (\rho_w e^{-R^*_{2,w}\cdot t} e^{-i\omega_w \cdot t \cdot \alpha \cdot \Delta T} + \rho_f e^{-R^*_{2,f}\cdot t} \sum_{p=1}^{P} \alpha_p \cdot e^{-i\omega_{f,p}\cdot t}) e^{-i2\pi\psi\cdot t}$
	Unknown parameter	$\Delta T, \psi$
	Pre-scan required?	Yes
	Fat peak spectrum /R2* decay	multi-/multi-
	Sequence/TR/TE	MGRE/50 ms/15.4, 21.8, 28.2 ms
(Hofstetter et al., 2012) (Soher et al., 2010)	Type of thermometry	Fat referenced
	Signal model	$S(t) = \left(\rho_w e^{-i\omega_w \cdot t} + \rho_f \sum_{p=1}^{P} \alpha_p \cdot e^{-i\omega_{f,p}\cdot t} \right) \cdot e^{-i2\pi\psi\cdot t}$
	Unknown parameter	ρ_w, ρ_f
	Pre-scan required?	Yes
	Fat peak spectrum /R2* decay	multi-/no-
	Sequence/TR/TE	MGRE/15.7 ms/10.9, 12.5, 14.1 ms
(Lam et al., 2015)	Type of thermometry	Fat referenced
	Signal model	$S(t) = \sqrt{|\rho_w|^2 e^{-2R^*_{2,w}\cdot t} + \left|\rho_f\right|^2 e^{-2R^*_{2,f}\cdot t} + 2|\rho_w|\left|\rho_f\right| e^{-\left(R^*_{2,w}+R^*_{2,f}\right)t} \cdot cos\,(2\pi\Delta f(T)\cdot t)}$
	Unknown parameter	$\rho_w, \rho_f, \Delta f(T)$
	Pre-scan required?	Yes
	Fat peak spectrum /R2* decay	single-/multi-
	Sequence/TR/TE	MGRE/52.5 ms/1.4 ms;32 echos, ΔTE = 1.3 ms

4.1.3 Hierarchical IDEAL

Iterative Decomposition of water and fat with Echo Asymmetry and Least (IDEAL) is usually used for the water/fat separation because of robustness in the field inhomogeneity but requires additional phase information in order to perform an iterative process (Reeder et al., 2004; Yu et al., 2008). Tsao et al (Tsao and Jiang, 2013) first introduced the hierarchical IDEAL method to perform more time effective computation than conventional IDEAL. It is based on the assumptions of a 6 fat peak model with a single R_2^*-decay. This section explains the IDEAL algorithm and how it can be used in the fat referenced PRFS thermometry.

The measured signal can be expressed in terms of the water and fat components as follows:

$$s(TE_n) = \left(\rho_w + \rho_f \sum_{p=1}^{P} \alpha_p \cdot e^{-i2\pi f_p TE_n} \right) \cdot e^{-(R_2^* + i2\pi\Psi)TE_n} \qquad \text{Equ. 4.1}$$

Where $s(TE_n)$ is the complex signal of the n$^{\text{th}}$ echo time TE_n, ρ_w and ρ_f are the complex-valued water and fat signals, f_p is the difference of spectral peaks between fat and water (-3.8, -3.4, -2.6, -1.94, -0.39, and 0.6 ppm)(Yu et al., 2008) and α_p is the relative amplitude of each spectral peak (0.087, 0.694, 0.128, 0.004, 0.039, and 0.048) (Yu et al., 2008), R_2^* is the global transversal relaxation rate ($R_2^* = 1/T_2^*$), and Ψ is the off-resonance precession frequency.

Equ. 4.1 can be transformed in a matrix representation:

$$S = D\,A\,\rho \qquad \text{Equ. 4.2}$$

$$S = \begin{bmatrix} s(TE_1) \\ s(TE_1) \\ \vdots \\ s(TE_n) \end{bmatrix}, A = \begin{bmatrix} 1 & \sum_{p=1}^{P} \alpha_p \cdot e^{-i2\pi f_p TE_1} \\ 1 & \sum_{p=1}^{P} \alpha_p \cdot e^{-i2\pi f_p TE_2} \\ & \vdots \\ 1 & \sum_{p=1}^{P} \alpha_p \cdot e^{-i2\pi f_p TE_n} \end{bmatrix}, D = diag \begin{bmatrix} e^{-(R_2^* + i2\pi\Psi)TE_1} \\ e^{-(R_2^* + i2\pi\Psi)TE_2} \\ \vdots \\ e^{-(R_2^* + i2\pi\Psi)TE_n} \end{bmatrix}, \rho = \begin{bmatrix} \rho_w \\ \rho_f \end{bmatrix}$$

The water-fat separation is achieved by determining the pure water and fat signals (ρ) from the images S acquired with multiple TEs. Hence, an estimate $\hat{\rho}$ for the water and fat signals can be calculated if the field map $D(R_2^*, \Psi)$ is known (Yu et al., 2005):

$$\hat{\rho} = A^{+}D^{-1}S \qquad \text{Equ. 4.3}$$

Where the superscript '+' indicates the Moore-Penrose inverse. The field map $D(R_2^*, \Psi)$ can be estimated by finding a minimum value for the residue R, where $R = S - \widehat{D}A\hat{\rho}$. This approach is associated with a linear least-square estimation of $\hat{\rho}$. Thus, the cost function can be written as $(D^{-1})^{T}(I - AA^{+})D^{-1}S$ by using the substitution in optimal expression for the coefficient vector. The minimized error can be expressed in a simpler manner as (Lu and Hargreaves, 2008):

$$\|\varepsilon\|^2 = \|(AA^{+} - I)diag(d)S\|^2 \qquad \text{Equ. 4.4}$$

$$d = \begin{bmatrix} 1 \\ e^{(R_2^* + i2\pi\Psi)(TE_2 - TE_1)} \\ \vdots \\ e^{(R_2^* + i2\pi\Psi)(TE_n - TE_1)} \end{bmatrix}$$

Where the diagonal matrix d is equivalent to the inverse matrix of D including the time difference with the first echo time. The inverse matrix $D^{-1}(R_2^*, \Psi)$ can be replaced with $D(-R_2^*, -\Psi)$ using the property of diagonal and complex exponentials. Equ. 4.4 can be expanded to effectively compute the algebraic formulation:

$$\|\varepsilon\|^2 = \sum\{(I - AA^{+}) \circ (SS^{H})^{*} \circ (dd^{H})^{*}\} \qquad \text{Equ. 4.5}$$

The symbol '∘' indicates the Hadamard product for the matrix N × N. The minimized error directly provides the best-fitted value for the term d. Briefly, the IDEAL algorithm estimates the field map D. Then, the matrix $A^{+}D^{-1}$ is used for the extraction of pure water and fat signal from the measured image S (Equ. 4.3).

Finding minimum error

In the Equ. 4.4, a local minima of ε is found by a multiresolution approach and the Nelder-Mead simplex algorithm (Nelder and Mead, 1965). In Figure 4.1a, the error ε depending on R_2^* and Ψ shows several local minimum regions. Finding optimal R_2^* and Ψ in the full resolution image causes large computational cost. Under the assumption that the field map varies smoothly, the multiresolution optimization was proposed (Tsao and Jiang, 2013); the optimum on a low-resolution image can predict the optimum on a high-resolution image because the spatial information of the field map is kept in the low-resolution image (Lu and Hargreaves, 2008).

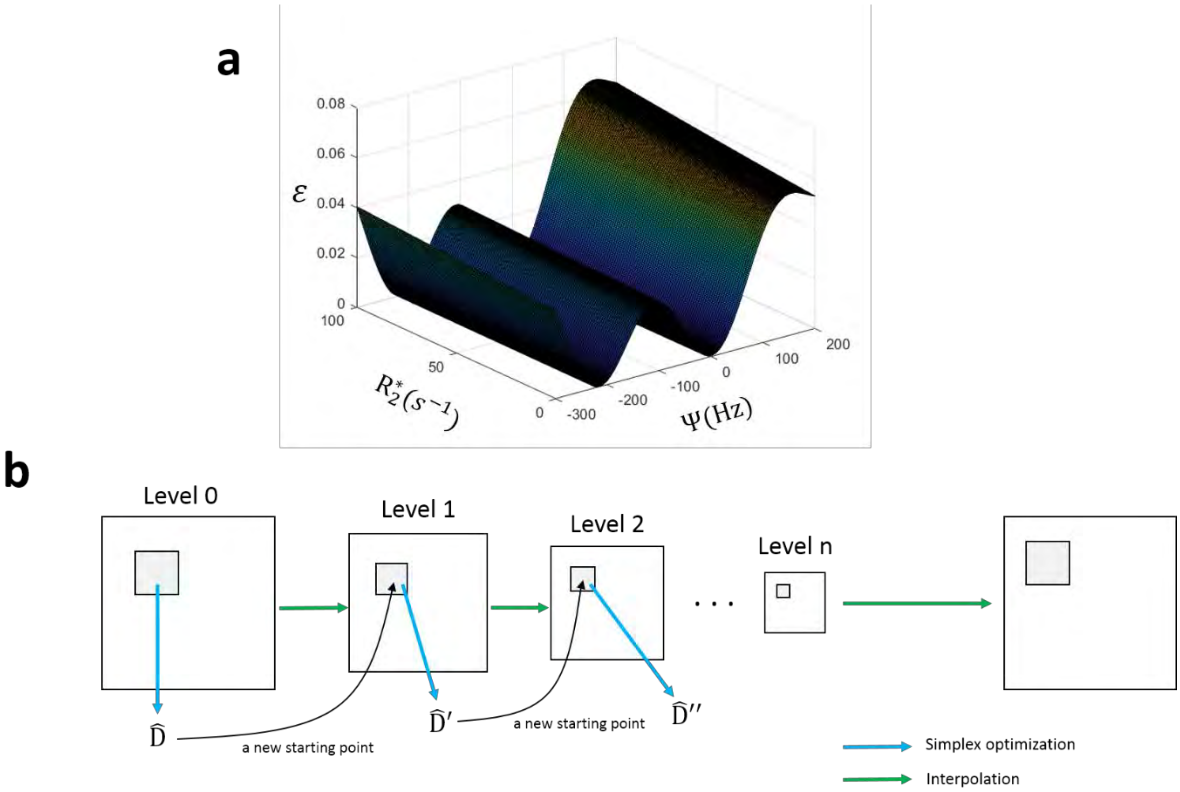

Figure 4.1 (a) An example of the error across the values of R_2^* and Ψ, (b) an illustration of multiresolution optimization. Gray rectangular box indicates the subdivided region. As reported in (Tsao and Jiang, 2013), 4096 regions at the finest image are used and the coarser image is made with a zoom factor of 67 %.

Figure 4.1b shows the procedure of the multiresolution optimization. At the finest level, 4096 subdivided regions are used to estimate the field map, and the result is applied as a starting point in the subsequent level. The Nelder-Mead simplex algorithm is applied to find the minimum value of ε at each level (Nelder and Mead, 1965). Bilinear interpolation is carried out to make the coarser image with a zoom factor of 67 %. After obtaining the final field map at the coarsest level, it is interpolated by using a Hanning window to reconstruct the full-resolution field map.

Here, we would like to acknowledge the use of the hierarchical IDEAL toolbox resulting from the fat-water toolbox initiative in the 2012 ISMRM Workshop on Fat-water Separation. In this Ph.D. thesis, this toolbox was used in its original implementation in order to derive the field map $D(R_2^*, \Psi)$.

4.1.4 Objective of this study

Current interventional MRE/MRT systems have used PRF thermometry, which is restricted to aqueous tissues only, and their use in fat-containing tissues may lead to significant errors in temperature estimation. The general objective of this chapter is to improve the accuracy of the PRFS thermometry of the interventional MRE/MRT method in all soft tissues, including fat-containing tissues. In this study, a time-efficient strategy is proposed that allows for simultaneous real-time FRPRFS thermometry with chemical shift water/fat separation and MRE. Compared to PRFS alone, FRPRFS will enable temperature estimation in fat-containing tissues while improving the overall accuracy of temperature estimation thanks to fat-reference B_0 drift correction. On one hand, an iterative least square fitting algorithm (IDEAL) is used for fast and robust water-fat separation in a dataset acquired with several varying TEs (Tsao and Jiang, 2013; Yu et al., 2008). On the other hand, MRE reconstructions require the acquisition of several images with varying phase offsets between the mechanical wave and the motion sensitive gradients (MSG), in order to capture the shear wave at different propagation times. The strategy described here takes advantage of the acquisition of several phase offsets in order to obtain the several echo times required for water-fat separation. Echo times and phase offsets are jointly incremented to enable water-fat separation for FRPRFS thermometry along with MRE. The number of MRE phase offsets and the number of TE used to solve the IDEAL algorithm are the same; hence, elastogram and FRPRFS temperature map are updated at the same time. Therefore, this method offers the opportunity to record chemical shift information into a single MRE dataset.

4.2 Theoratical framework

4.2.1 Pulse sequence

As shown in Figure 4.2, a GRE MRE sequence is modified in order to obtain varying echo times for water/fat separation: each pair of images with opposite MSG was acquired at a specific TE and its corresponding MRE phase offset. MRE phase offset θ corresponds to the trigger delay between the mechanical shear wave and the MSG. Unidirectional MSG encoding was used in order to keep the temporal resolution compatible with thermal ablation monitoring. The acquisition scheme consists of interleaved acquisitions with opposite MSG polarities (MSG$+/-$) and identical TE/phase offset; hence, both TE and phase offset change every two images.

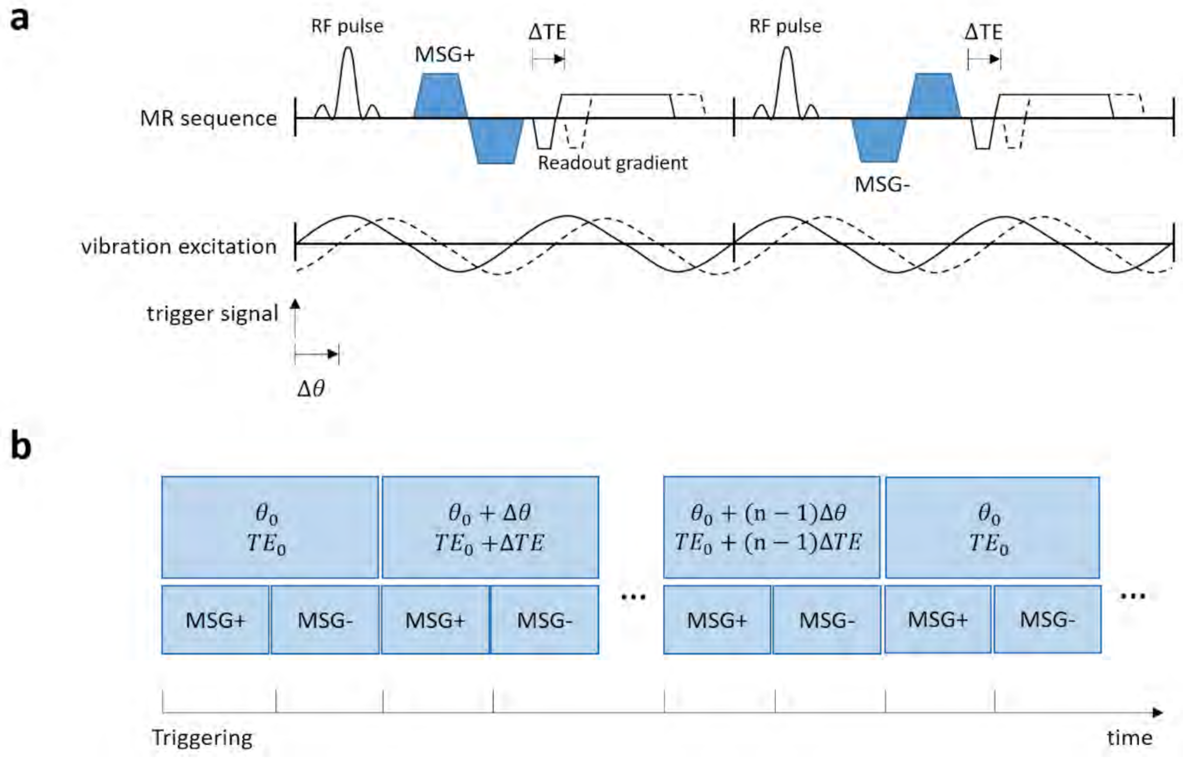

Figure 4.2 (a) Schematic chronogram of the GRE MRE sequence for simultaneous MRE and FRPRFS thermometry. For clarity, the main elements of the GRE MRE sequence are represented in a single line (RF pulse, MSG and read out gradient). TE and MRE phase offsets are shifted by ΔTE and $\Delta\theta$, respectively. (b) Summarized acquisition scheme, with n being the number of phase offsets and TEs. Images are acquired with alternating the polarity of MSG. Each pair of images is acquired with the same specific TE and phase offset.

Elastograms are reconstructed as described in chapter 2.5. Fat-referenced PRFS maps with fat-water separation are reconstructed as described in the following subchapter 4.2.2. Figure 4.3 shows the flow chart of temperature and elasticity reconstruction. If 4 phase offsets are used for the experiment, the first elastogram and temperature map are obtained once a full dataset including 4 phase offsets / 4 TEs is obtained (corresponding to the acquisition of 8 images, i.e. 4 pairs of opposite MSG polarity phase images); subsequent ones can be reconstructed with every newly obtained pair of phase images with opposite MSG (Corbin et al., 2016b).

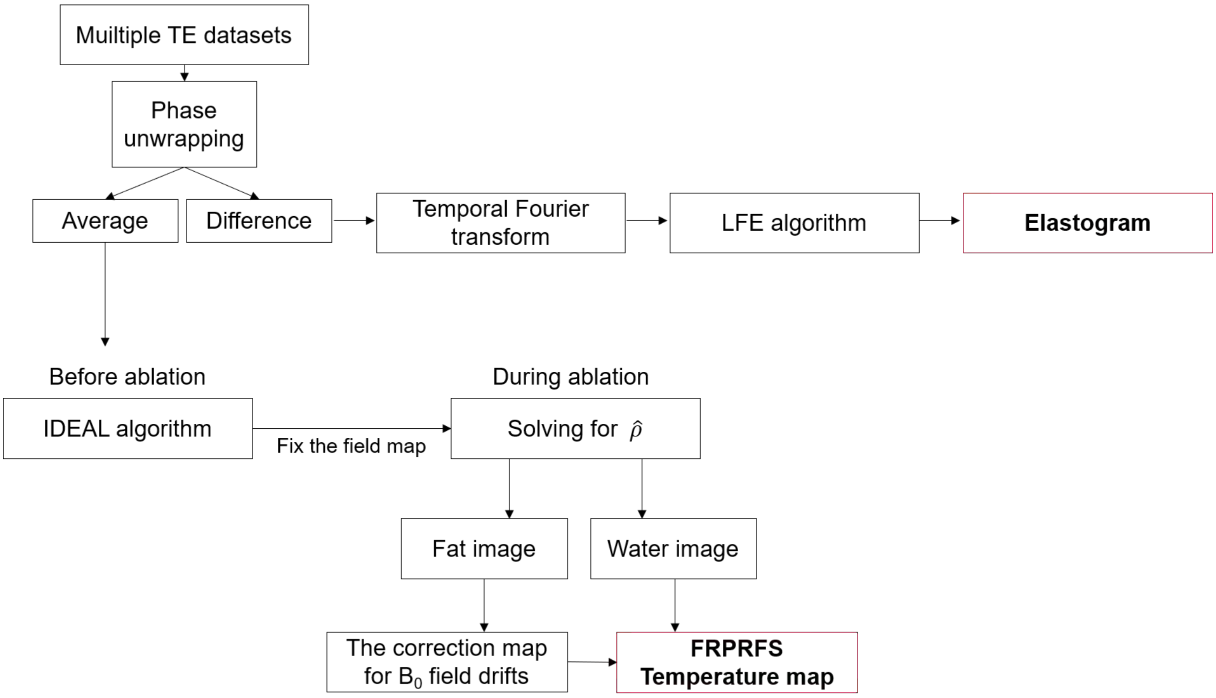

Figure 4.3 Flow chart of temperature and elasticity reconstruction. Once a full dataset is acquired, different combinations of each pair of phase images with opposite MSG polarities are used either for MRE elastogram reconstruction (difference) or for FRPRFS thermometry (average). The FRPRFS processing is detailed in the next subchapter.

4.2.2 Fat-referenced PRFS Thermometry

When temperature changes, it yields a significant phase variation in the complex water term $\rho_w = \rho_w^0 e^{i\phi_T}$, where ϕ_T is the phase shift caused by temperature and ρ_w^0 is the complex water signal in the absence of temperature change. The field map $D(R_2^*, \Psi)$ is estimated once before the ablation starts with the hierarchical IDEAL algorithm. This field map estimate is then used to extract both water and fat complex signals in all latter datasets acquired during the ablation, following Equ. 4.3. This approach aims at reducing the computational complexity during the ablation by avoiding the optimization step of the IDEAL algorithm (Figure 4.3).

This simplification is possible for two reasons. First, temperature induced R_2^* changes are neglected because they only affect the magnitude of both water and fat signals, and hence have no effect on temperature estimates. Second, time-varying B_0 field drifts affect both the phases of water and fat; the B_0 field drifts can therefore be estimated from the fat phase so that they are corrected for in the water phase map (Figure 4.4). For that purpose, the field drift correction map is estimated with spatial polynomial fitting of the fat phase map in fat-containing tissues (Equ. 4.6-7).

$$\phi_c(a, x, y) = a_0 + a_1 x + a_2 y + a_3 x^2 + a_4 y^2 + a_5 xy + \cdots \qquad \text{Equ. 4.6}$$

$$\min \left\| \phi_c(a, x, y) - \phi_f(x, y) \right\|^2 \qquad \text{Equ. 4.7}$$

Therefore, temperature changes, ΔT (°C), can be estimated from the phase of water protons, with field drift correction using FRPRFS, following (Hofstetter et al., 2012):

$$\Delta T = \frac{[\phi_w - \phi_w^0] - [\phi_C - \phi_C^0]}{\gamma \alpha B_0 TE} \qquad \text{Equ. 4.8}$$

Where ϕ_w and ϕ_w^0 are respectively the current and reference water phase maps, ϕ_C and ϕ_C^0 are respectively the current and reference field drift correction maps, γ is the gyromagnetic ratio of the hydrogen nuclei, B_0 is the main magnetic field, α is the temperature dependent water chemical shift (≈-0.01 ppm/°C), and TE is the average of the echo times used.

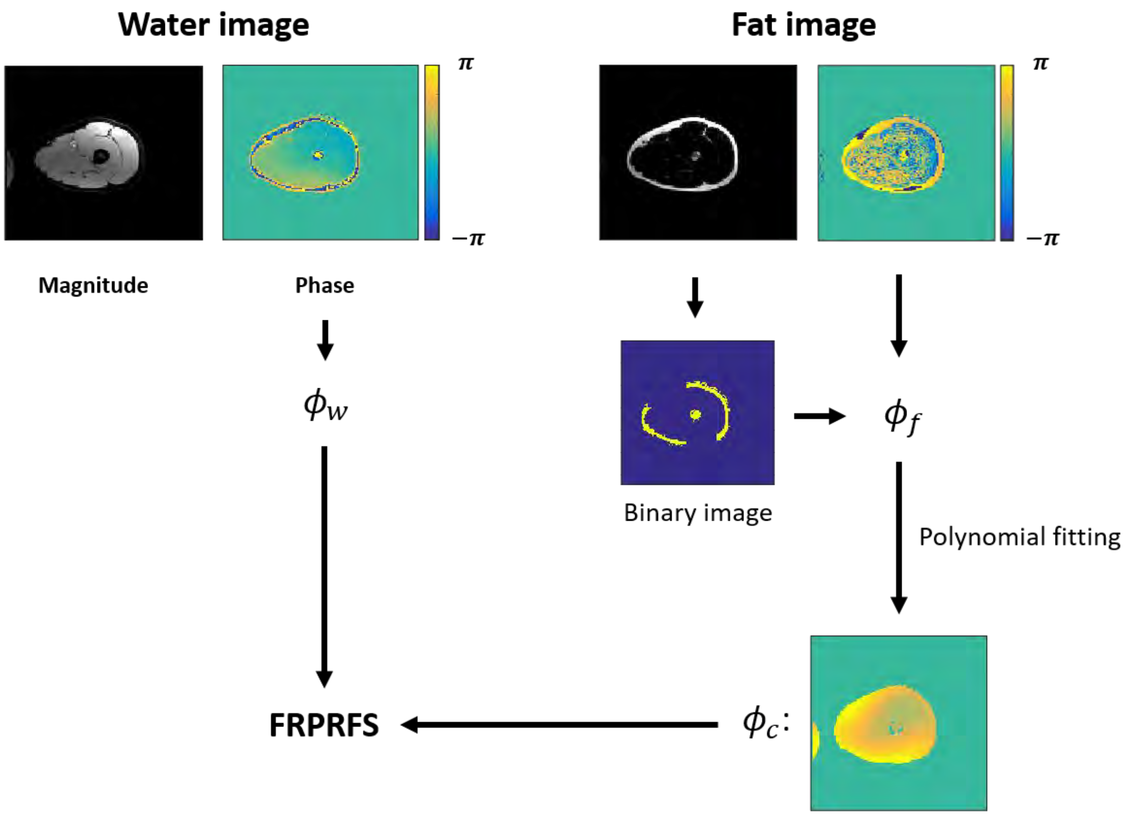

Figure 4.4 Scheme of FRPRFS Thermometry. The water phase map ϕ_w is used for temperature dependent PRFS and the fat phase map is used to estimate the correction map representing the B_0 field drift. For example, the data for polynomial fitting is selected in a binary image, which represents the region with a fat fraction over 80%.

4.2.3 MRE and water-fat separation

MRE coupled with water-fat separation was proposed for diagnostic in liver pathologies (Numano, T et al., 2017; Trzasko, J et al., 2015). Trzasko et al. combined 3D MRE acquisitions, varying MRE encoding directions and TEs together in order to obtain the 3D MRE displacement field and water-fat separation based on the IDEAL method (Trzasko, J et al., 2015). Numano et al. proposed the use of multi-echo GRE MRE sequence with 2 point-Dixon for water-fat separation (Numano, T et al., 2017). The proposed method was developed specifically for real-time monitoring of thermal ablations, and as such, is based on a third time-efficient combination of the acquisitions for MRE and IDEAL based fat-water separation allowing for FRPRFS.

4.3 Methods

4.3.1 TE selection for MRE and IDEAL processing

For the combination between MR Elastography and hierarchical IDEAL, it is essential to investigate the selection of echo times in order to obtain adequate sampling for fat-water separation while preserving the PNR for MRE. Indeed, the MSG encoding necessary for MRE determines the minimum TE of the phase images, while the TE increments necessary for chemical shift fat-water separation further degrade the PNR in phase images used for the elastrogram reconstruction.

Reeder et al. (Reeder et al., 2004) determined the optimal TE increment for IDEAL fat-water separation at 1.5 T to be 1.5 ms and 1.1 ms for three and four equally spaced echoes, respectively. Experiments were conducted in order to adapt such results to our specific combined MRE-fat/water separation framework. The phantom is made of 7% gelatin background and pure cream with different fat fractions (10%, 20%, and 30% fat fractions). Results obtained with IDEAL in 4 fat/water chemical shift acquisition protocols including 4 TEs each, varying in both $TE1$ and ΔTE are compared to a reference 2-point DIXON chemical shift fat/water separation (detailed parameters given in Table 4.2). The initial TEs, $TE1$, were chosen in the range of TEs to be expected due to MRE constraints on minimum TE in GRE sequences. The fat fraction is calculated as $|\rho_f|/(|\rho_w| + |\rho_f|) \times 100$ (%).

Table 4.2 MR acquisition parameters.

Sequence type	Method	No. Echo	TE1 (ms)	ΔTE (ms)	TR (ms)	Bandwidth (Hz/Px)	Matrix	Flip angle	FOV (mm^2)
GRE	IDEAL 1	4	8.2	1	20	500	128×128	15°	300
GRE	IDEAL 2	4	8.2	1.5	20	500	128×128	15°	300
GRE	IDEAL 3	4	11	1	20	500	128×128	15°	300
GRE	IDEAL 4	4	11	1.5	20	500	128×128	15°	300
GRE	Dixon	2	2.38	2.38	15	500	128×128	15°	300

Figure 4.5 shows fat fraction maps reconstructed with 2-point Dixon and the 4 IDEAL protocols. Cream inclusions are clearly visible in fat fraction maps for all methods.

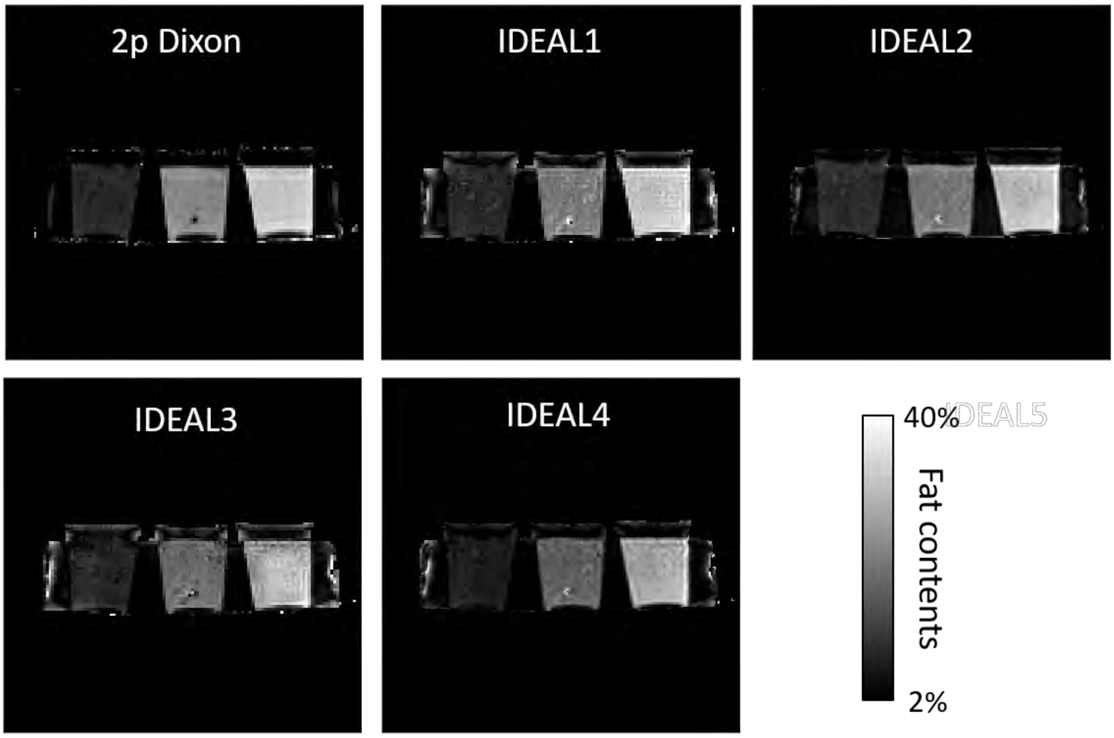

Figure 4.5 Water/fat separation with 2-point DIXON and 4-point IDEAL with different TEs: IDEAL 1 (TE1 8.2 ms, ΔTE 1 ms), IDEAL 2 (TE1 8.2 ms, ΔTE 1.5 ms), IDEAL 3 (TE1 11 ms, ΔTE 1 ms), IDEAL 4 (TE1 11 ms, ΔTE 1.5 ms), and 2-pt Dixon (TE 2.38 ms and 4.76 ms).

Figure 4.6 shows the means and standard deviations calculated in the 3 cream inclusions. Datasets with a short initial echo time (IDEAL 1 and 2) are in better agreement with the expected fat content of the cream (based on fat content provided by the manufacturer) and 2-point Dixon estimates, than the datasets with a longer initial echo time (IDEAL 3 and 4). When the initial echo time is 8.2 ms, the echo time increment 1 or 1.5 ms makes no significant difference, while when the initial echo time is 11 ms, the shorter echo time increment (1 ms) is in better agreement with reference values than the longer echo time increment (1.5 ms), reflecting the loss in SNR due to T_2^* decay with longer TEs. In conclusion, these experimental results show the influence of the SNR of images on the quality of the water/fat separation with 4-point IDEAL.

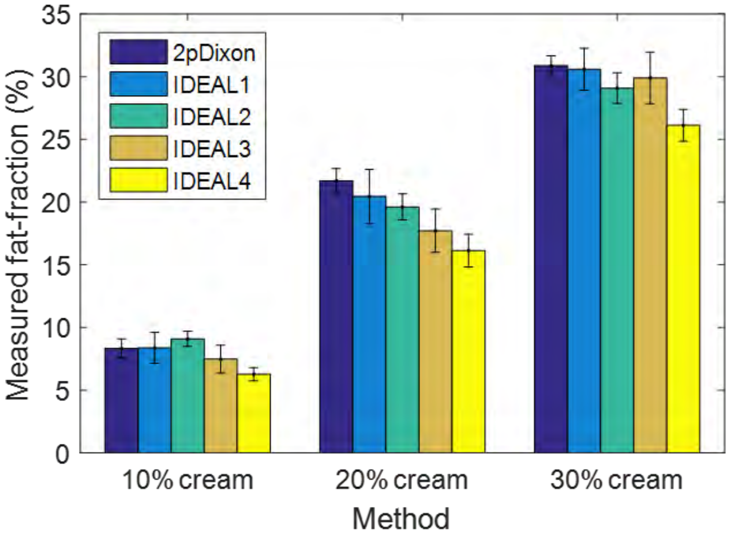

Figure 4.6 Mean and standard deviation calculated in 10 %, 20 %, and 30 % cream inclusions with 2pt-Dixon and 4 different IDEAL parameters.

Following this initial study, the initial echo times were kept within the range 8 to 10 ms, and TE increments were within the range of 1 to 1.5 ms.

4.3.2 Experiment 1: Temperature validation

The proposed method was first demonstrated in a phantom experiment with hot water circulation, mimicking a thermal ablation in fatty tissues. The phantom was made of 8% gelatin in water and contained a water/fat cylindrical inclusion (2% gelatin in milk cream, 20% fat). As shown in Figure 4.7, a cylindrical plastic tube chamber connected to a water circuit was placed inside the inclusion for hot water circulation. A syringe was used for the manual circulation of hot water (about 90°C). After baseline imaging for 100 s, hot water was circulated between 100 s and 220 s, and a second time between 370 s and 417 s. The pneumatic MRE exciter was positioned below the phantom. Relevant acquisition parameters include: 4 TEs = 8.2/9.7/11.2/12.7 ms; TR 16 ms; Flip angle 15°; FOV 300 × 300 mm; Matrix 128×128; Slice thickness 6 mm; Bandwidth 800 Hz/pixel; MSG frequency 162 Hz; mechanical wave frequency 125 Hz; MRE phase offsets 4; Readout MSG encoding direction. Images were acquired in the axial plane, 5 mm away from the hot water tube in the head-foot direction. An optical fiber thermometer (LumaSense Technologies, Inc.) was used in order to validate FRPRFS temperature measurements. The two optical fiber probes were placed on the image plane, one at the level of the center of the hot water tube, the other 1.5 cm laterally (left-right direction). The field correction maps were obtained using a second order polynomial fitting of the fat phase in the cream.

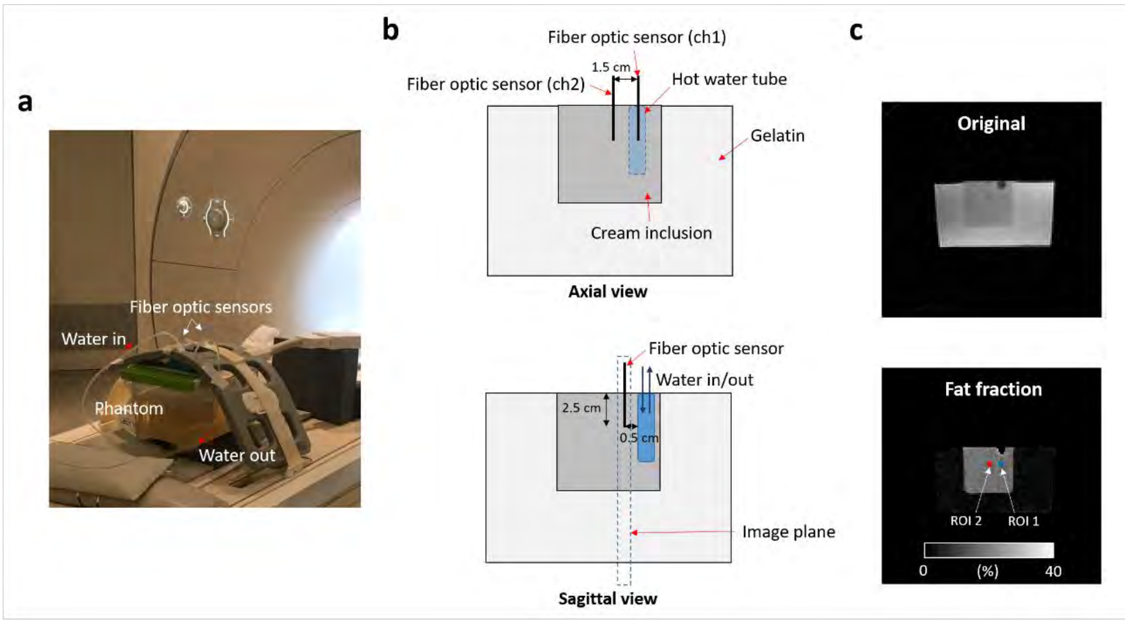

Figure 4.7 (a) Experimental setup, (b) Schematic axial (top) and sagittal views (bottom) of the experimental setup, and (c) the axial magnitude image (top) and its corresponding fat fraction map (bottom) obtained before heating. The two optical fiber thermometers are positioned 15 mm apart in the image plane located 5 mm away from the hot tube side. The pneumatic exciter was placed below the phantom. ROI 1 and 2 indicate the position of the tips of the two optical fibers.

4.3.3 Experiment 2: Comparison with single TE dataset

A second phantom experiment was investigated to study how T_2 modulation affects elastograms obtained with varying echo times, compared to those reconstructed with a single TE dataset. The phantom (8% gelatin in water) containing a water/fat cylindrical inclusion (2% gelatin in milk cream, 20% fat) was used here (Figure 4.8). Relevant acquisition parameters are: TR 16 ms; TE 8.2/9.7/11.2/12.7 ms; Flip angle 15°; FOV 300 mm × 300 mm; Matrix 128 × 128; Slice thickness 6 mm; Bandwidth 800 Hz/px; MSG frequency 162 Hz; mechanical wave frequency 125 Hz; MRE phase offsets 4; Readout encoding direction. A MR-compatible HIFU system (Image Guided Therapy, Inc., Pessac, France) was used in order to generate heat inside the phantom, and a 256-element transducer was driven at 1MHz/60W acoustic power. A multifocal, cylindrical region (10 mm height, 12 mm diameter) was heated during 5.5 s using a spiral trajectory. Heating pattern was repeated 20 times, leading to a total heating time of 110 s.

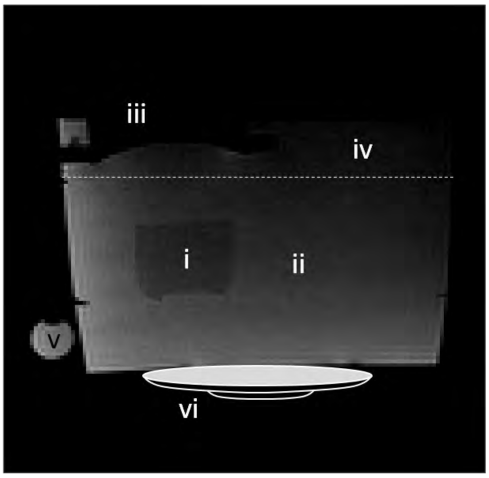

Figure 4.8 Experimental setup: cream-gelatin inclusion (2% gelatin in milk cream, 20% fat, i), background 8 % gelatin (ii), HIFU transducer (iii), degassed-water (iv), 100% sunflower oil (v), and pneumatic MRE exciter (vi).

4.3.4 Experiment 3: Ex-vivo HIFU experiment

A third experiment was performed to evaluate the proposed framework during High Intensity Focused Ultrasound (HIFU) ablation ex-vivo. Two porcine rib muscle tissue samples obtained from a local butchery were enclosed in a gel made of 7 % gelatin for the background and two lateral 2% gelatin in milk cream inclusions (Figure 4.9). The experiment was carried out in two different locations for each sample, for a total of 4 experiments. A 128-element HIFU transducer (Imasonic, Voray sur l'Ognon, France) was positioned on the top of the tissue using a degassed water layer for acoustic coupling. A pneumatic MRE exciter was placed below the container. MR parameters identical to those used for the gel phantom experiment were used in sample 1 (experiments #1 and #2). Due to substantial differences in terms of tissue elasticity, the mechanical wave frequency was changed to 100 Hz for the second sample (experiments #3 and #4), yielding a different value of TR (20 ms); images were acquired in the sagittal plane with through slice MSG encoding direction.

An MR-compatible multi-channel HIFU generator (Image Guided Therapy, Inc., Pessac, France) was used for this experiment with the 128-element transducer being driven at 1MHz. HIFU ablation was performed using a 5-point focusing pattern, following a circular trajectory (4 mm in diameter, 2 seconds per point) at an acoustic power of 45 W. The total scanning time was 10 minutes with successively 2 min baseline, 2 min HIFU heating and 6 min cooling period. The field correction maps were obtained using a second order polynomial fitting of the fat phase in the cream.

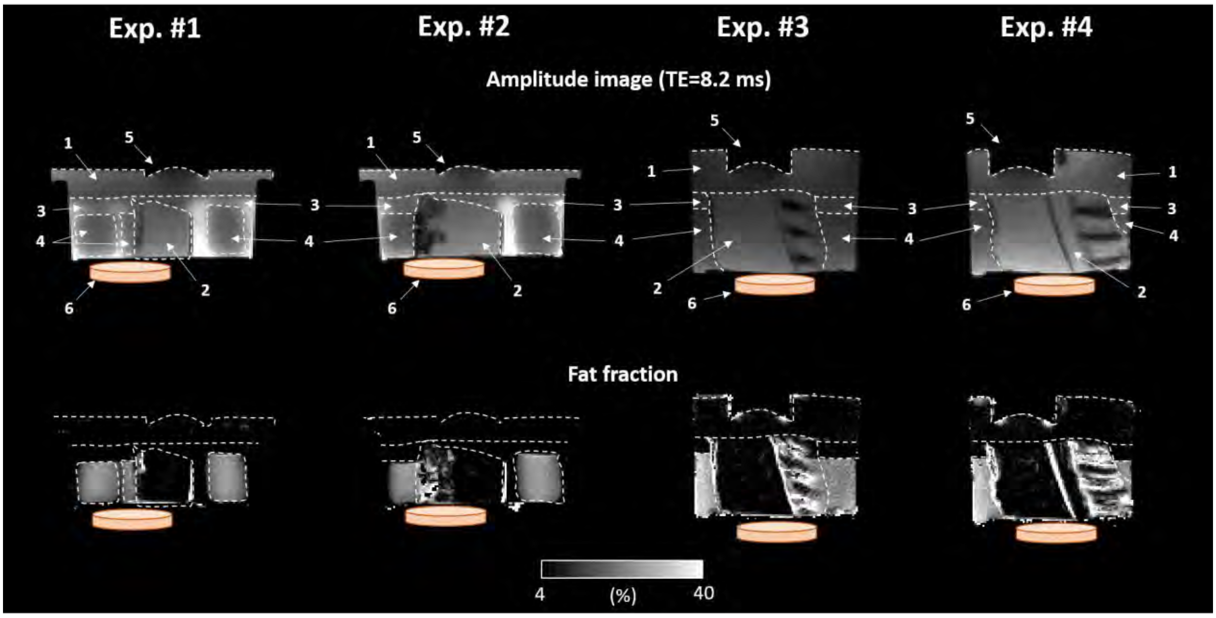

Figure 4.9 Experimental setup and fat fraction map $(|\rho_f|/(|\rho_w| + |\rho_f|) \times 100)$ before HIFU ablation. White-dashed line delineate different areas of the phantom: 1. Degassed water, 2. Pig rib muscle tissue, 3. 7% gelatin, 4. 2% gelatin in milk cream, 5. HIFU transducer, 6. Pneumatic exciter.

4.4 Results

4.4.1 Experiment 1: Temperature validation

A fat fraction value of 20.42±1.4% was measured before heating in the cream-gelatin inclusion, using the IDEAL algorithm; this result is consistent with the fat content of the cream (20% as provided by the manufacturer) used for this experiment (Figure 4.7c, bottom). Figure 4.10 shows temperature changes (ΔT), elasticity changes ($\Delta\mu$), and wave images measured at times 40 s (resting state), 200 s (first heating), and 400 s (second heating). The temperature increase (ΔT) was found to be accompanied by cream softening that corresponds to a decrease in the shear modulus, and a local decrease of the shear wavelength.

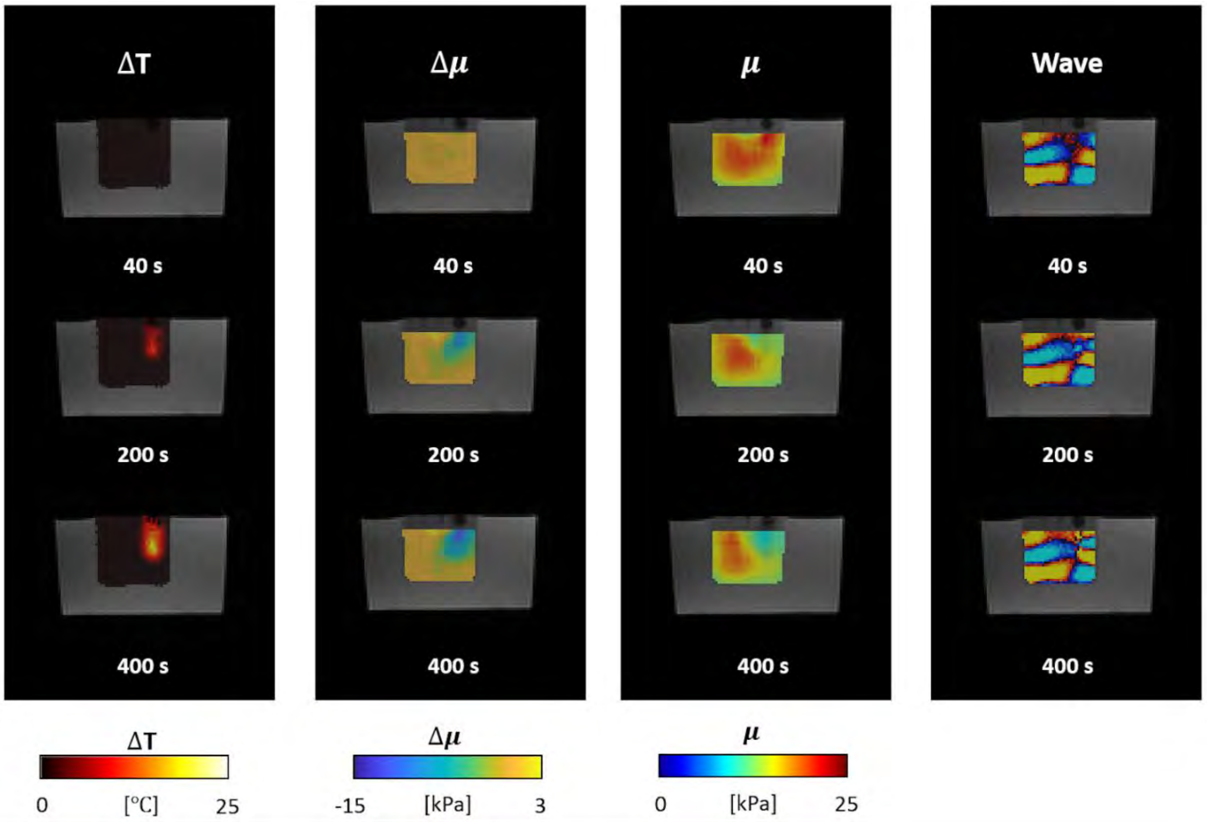

Figure 4.10 From left to right, magnitude image overlaid with temperature changes (ΔT), elasticity changes ($\Delta\mu$), elasticity maps (μ), and wave images, obtained before (time 40 s) and during heating (times 200 s and 400 s). During heating phases (200 s and 400 s), a localized increase in temperature is observed. It results in gel softening in the inclusion, as reflected by the relative decrease in the shear wavelength. Note that this axial view correspond to a slice position 5 mm away from the side of the water tube (refer to Fig. 4.7.b bottom view).

Two ROIs (2×2 pixels) were selected at the tips of the optical fiber sensors. Time-dependent profiles of temperature and elasticity measured in these ROIs are plotted in Figure 4.11. The measurements of optical fiber sensors were in good agreement with those of the FRPRFS thermometry. The mean absolute deviation between temperature changes measured with the optical fiber sensor and FRPRFS in ROI 1 and 2 were 1.5±1.3 °C and 0.9±0.7 °C, respectively. Over the course of the experiment, the shear modulus in ROI 1 was found to decrease from 21.6±1.2 kPa (0-100 s) to 10.53±0.3 kPa (500-600 s), while the shear modulus in ROI 2 decreased from 20.6±0.7 kPa to 15.4±0.7 kPa.

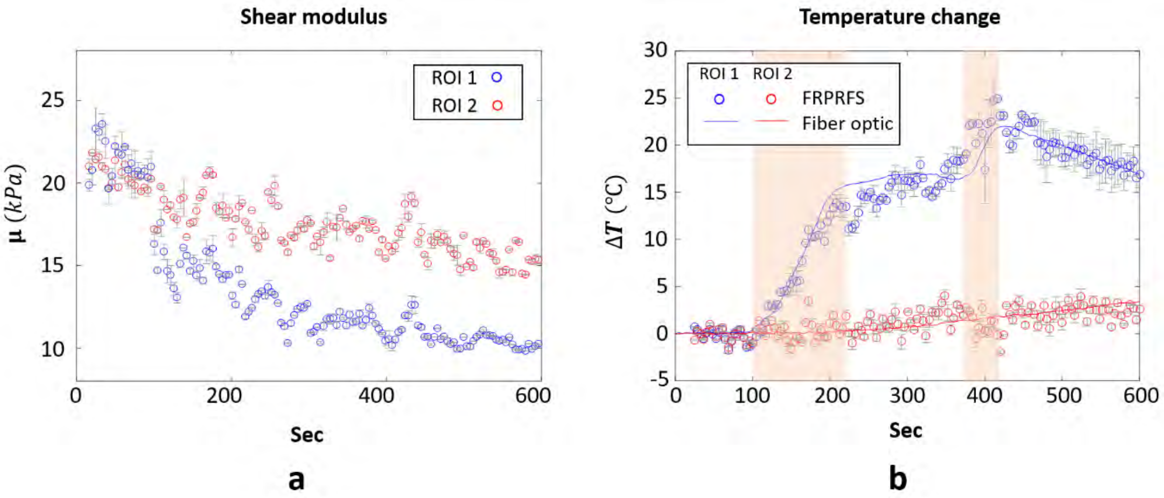

Figure 4.11 Time-dependent profiles of the shear modulus (a) and temperature changes ΔT (b) in ROI 1 and ROI 2 (2×2 pixels, shown in Figure 4.7). Solid lines correspond to optical fiber measurements (ROI 1 in blue, ROI 2 in red). Blue and red circles indicate measurements of the FRPRFS in ROI 1 and 2, respectively. The faded-orange regions in the graph indicate heating phases.

4.4.2 Experiment 2: Comparison with single TE dataset

No significant difference in wave pattern is found between phase difference images obtained from standard single TE and multiple TE datasets (Figure 4.12). The difference in absolute error results from the lengthened TE, however such low spatial frequency phase variation is filtered out during the MRE processing.

Corresponding elastograms (Figure 4.13) show excellent agreement with relative error equal to 4.7±1.8 % over the whole phantom. Thus, using multiple TE datasets appears to result in similar elastograms as single TE standard MRE.

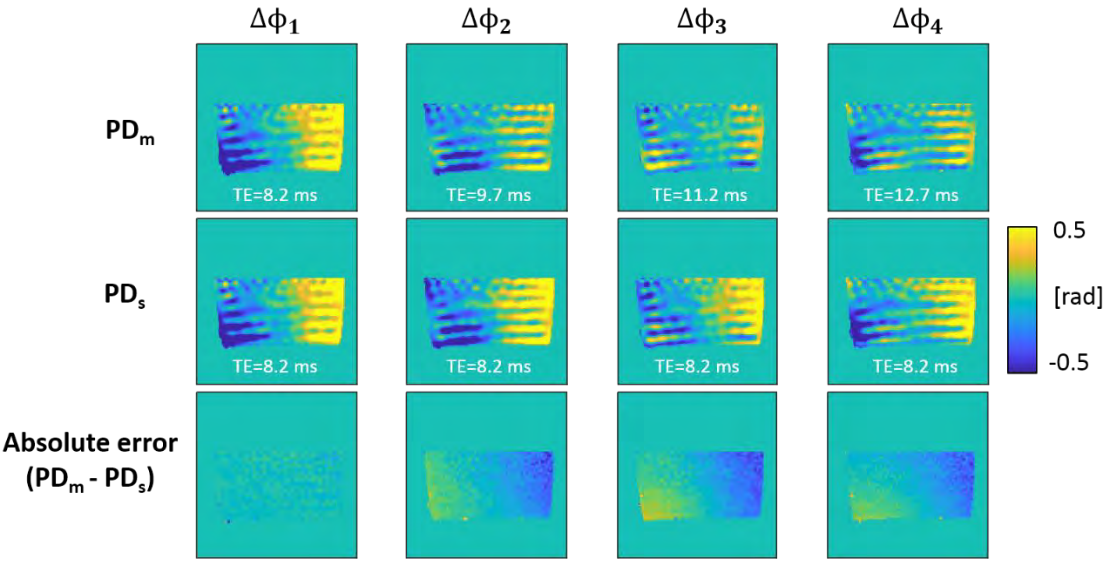

Figure 4.12 Comparison between Phase Difference (PD) images obtained with standard single TE (PD_s, center row) and multiple TE (PD_m, top row) datasets. Wave patterns appear to be similar. The difference in absolute error (bottom row) results from the lengthened TE, however such low spatial frequency phase variation is filtered out during the MRE processing.

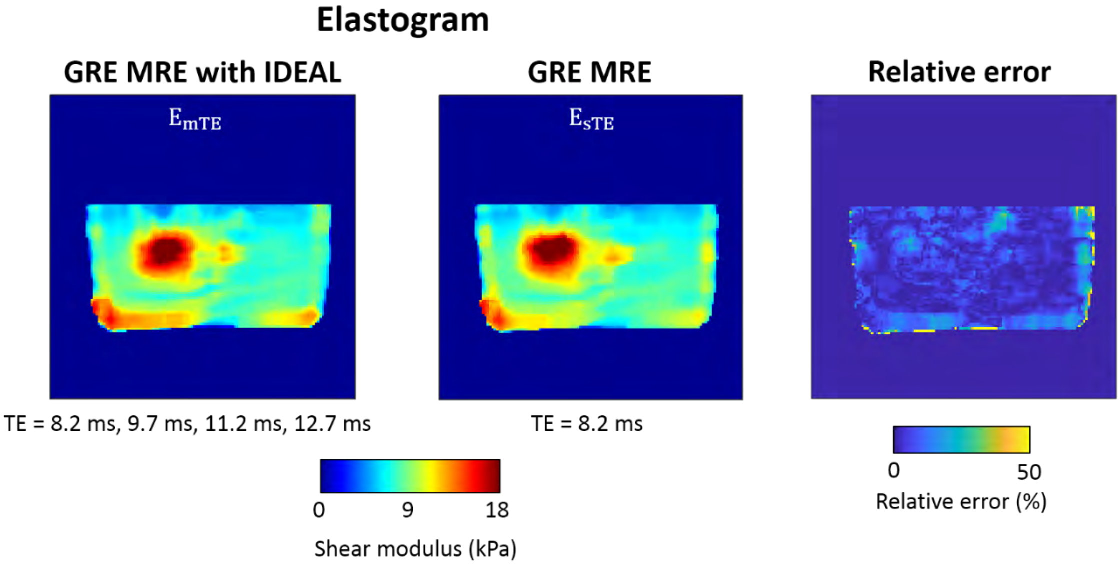

Figure 4.13 Elastograms reconstructed with multiple TE (E_{mTE}) and single TE (E_{sTE}) datasets. Relative error is calculated by $|E_{mTE} - E_{sTE}|/E_{sTE} \times 100$. The mean and standard deviations of relative error

are measured as 4.7±1.8 % in the whole region of the phantom. Hence, GRE MRE with IDEAL provides elastograms that are similar to those obtained by conventional GRE MRE.

During HIFU ablation, the temperature rise at the focal spot is accompanied by a decrease of the shear modulus within the inclusion, as seen through local changes in shear wavelength (Figure 4.14). Fat-referenced temperature and elasticity measured over time are plotted in Figure 4.15. Shear moduli in ROIs 1-3 decrease from 18.8/17.5/18.5 kPa to 7.5/10/11 kPa with maximal heating 30/17/11 °C, respectively.

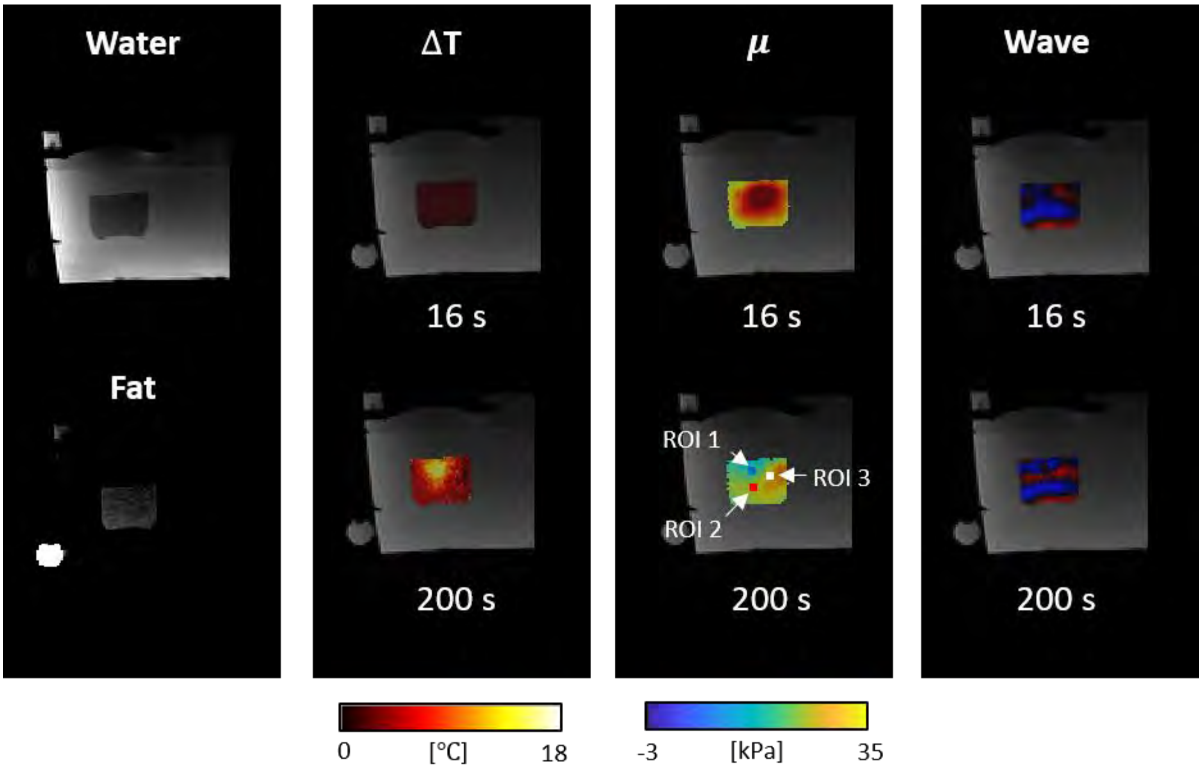

Figure 4.14 Water, fat, elasticity, wave, and temperature change (ΔT) images before and after HIFU heating, overlaid with the magnitude image. The HIFU heating starts at time 90 s, lasts 110 s and is stopped at time 200 s. Before heating, the stiffer inclusion is visible in the elastograms. At the end of HIFU heating, PRFS shows the temperature increase at the focal spot, which results in gel softening in the inclusion and is reflected by relative decrease in the shear wavelength.

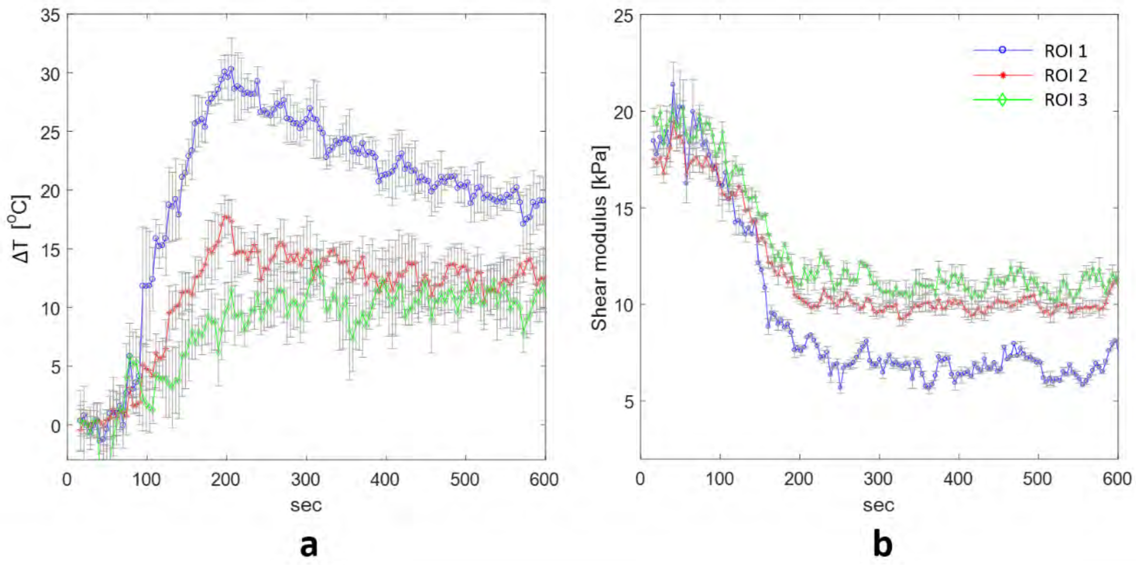

Figure 4.15 Time-dependent profiles of (a) shear modulus and (b) temperature changes (ΔT) during and after HIFU heating in ROI 1, 2, and 3 (2×2 pixels, blue, red, and white boxes shown in Figure 4.14) at focal spot. As expected, temperature increases at the focal spot during heating, and then slowly goes back to its original value, while mechanical properties at the focal spot are durably altered.

4.4.3 Experiment 3: Ex-vivo HIFU experiment

Because of high variability across the muscle samples, changes in mechanical properties are displayed in terms of relative stiffness changes (RSC = $\Delta\mu/\mu_0$, where μ_0 is the initial stiffness). Figure 4.16-19 show ΔT, RSC, elasticity maps, and wave images measured before (100 s), after HIFU heating (250 s), and during cooling down (570 s) in 4 experiments, respectively. In total, shear modulus was found to decrease at the focal spot, as shown in the RSC maps.

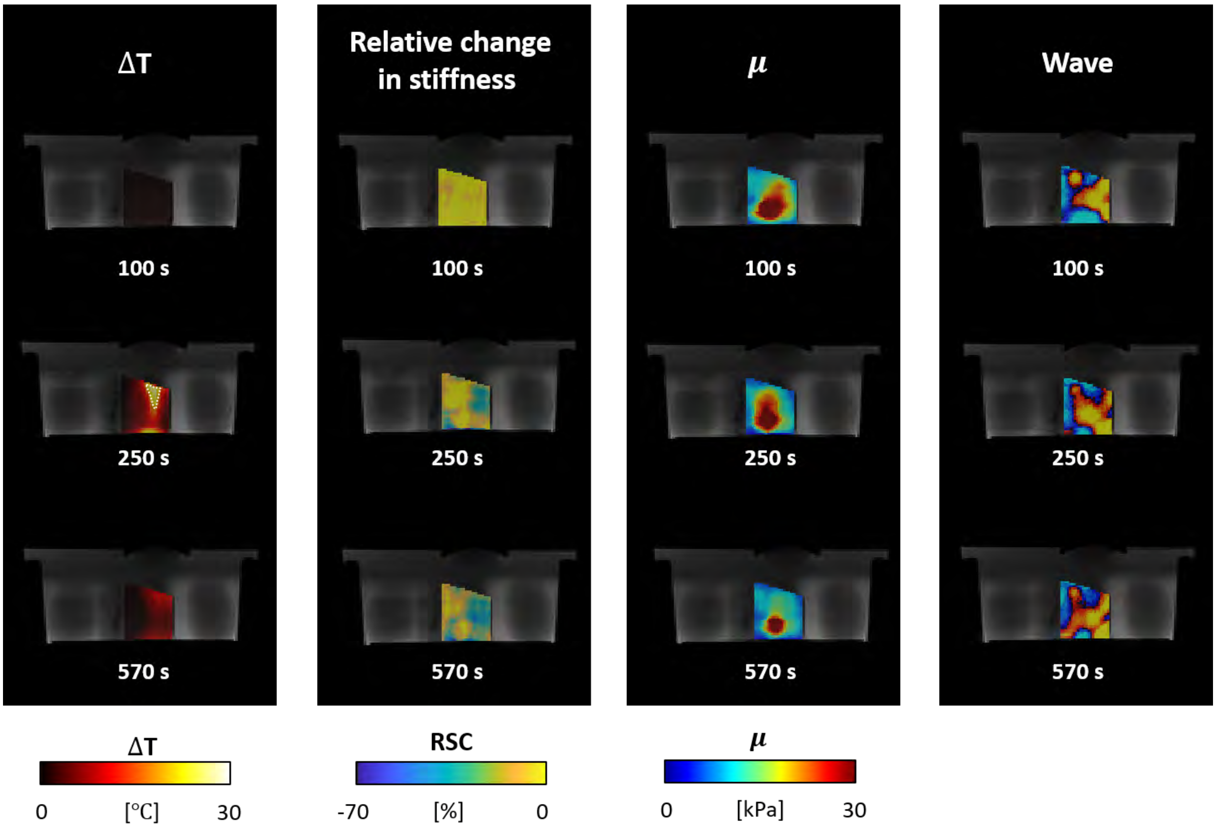

Figure 4.16 Result of experiment #1(first heating / Sample 1). From left to right, temperature changes (ΔT), relative stiffness change (RSC), elasticity maps (μ), and wave images overlaid with the magnitude image at the first TE, before (time 100 s), during (time 250 s) HIFU heating and after, during the cooling time (time 570 s). Temperature maps showed local temperature increase because of the HIFU heating. Corresponding relative changes in the shear modulus (RSC) were observed in the heated zone, corresponding to wavelength decreasing locally.

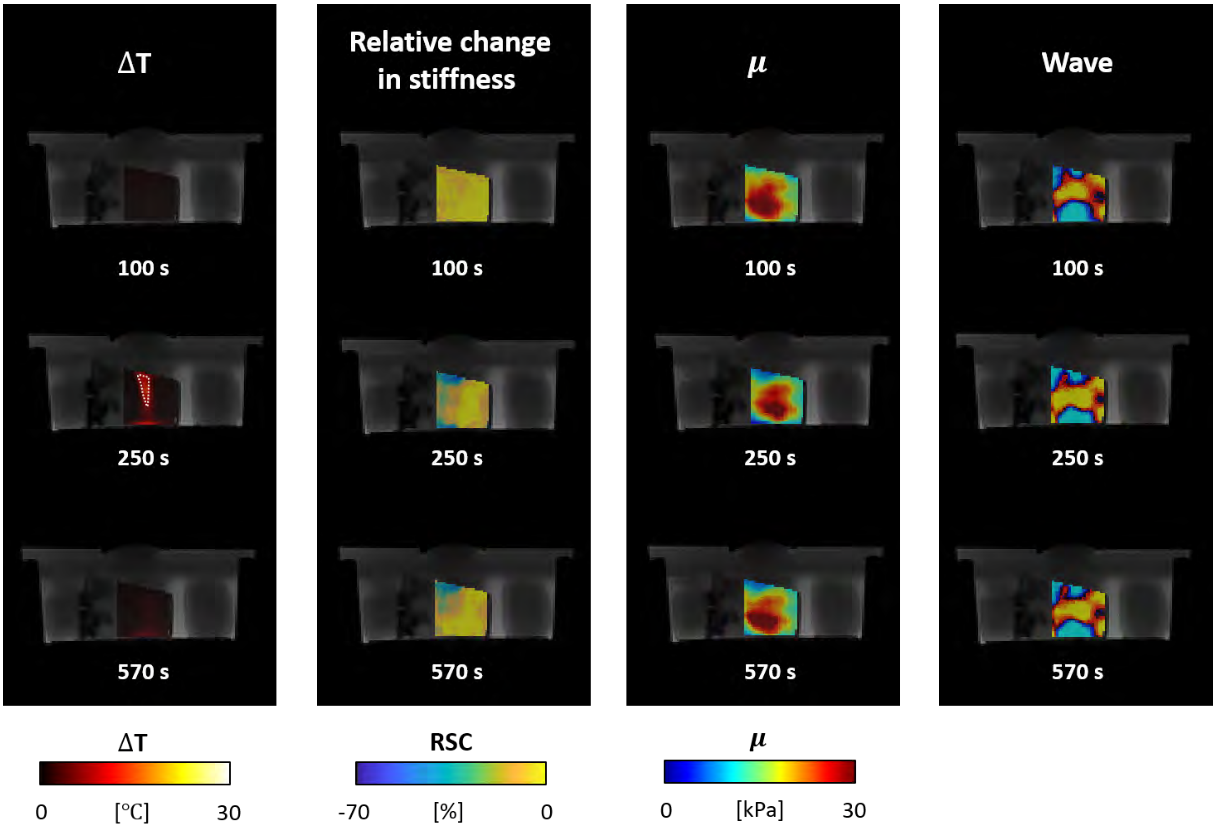

Figure 4.17 Result of experiment #2 (second heating / Sample 1). From left to right, temperature changes (ΔT), relative stiffness change (RSC), elasticity maps (μ), and wave images overlaid with the magnitude image at the first TE, before (time 100 s), during (time 250 s) HIFU heating and after, during the cooling time (time 570 s).

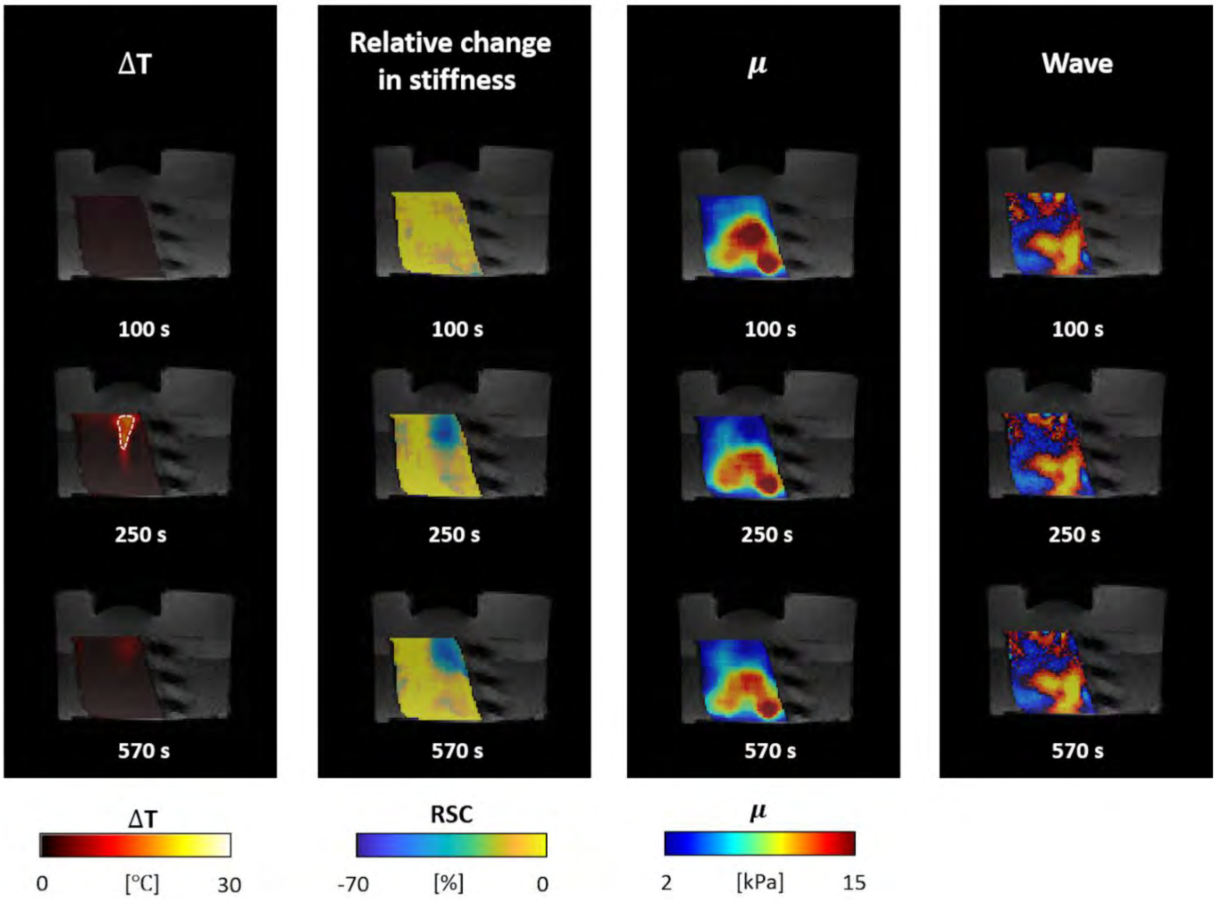

Figure 4.18 Result of experiment #3 (first heating / Sample 2). From left to right, temperature changes (ΔT), relative stiffness change (RSC), elasticity maps (μ), and wave images overlaid with the magnitude image at the first TE, before (time 100 s), during (time 250 s) HIFU heating and after, during the cooling time (time 570 s).

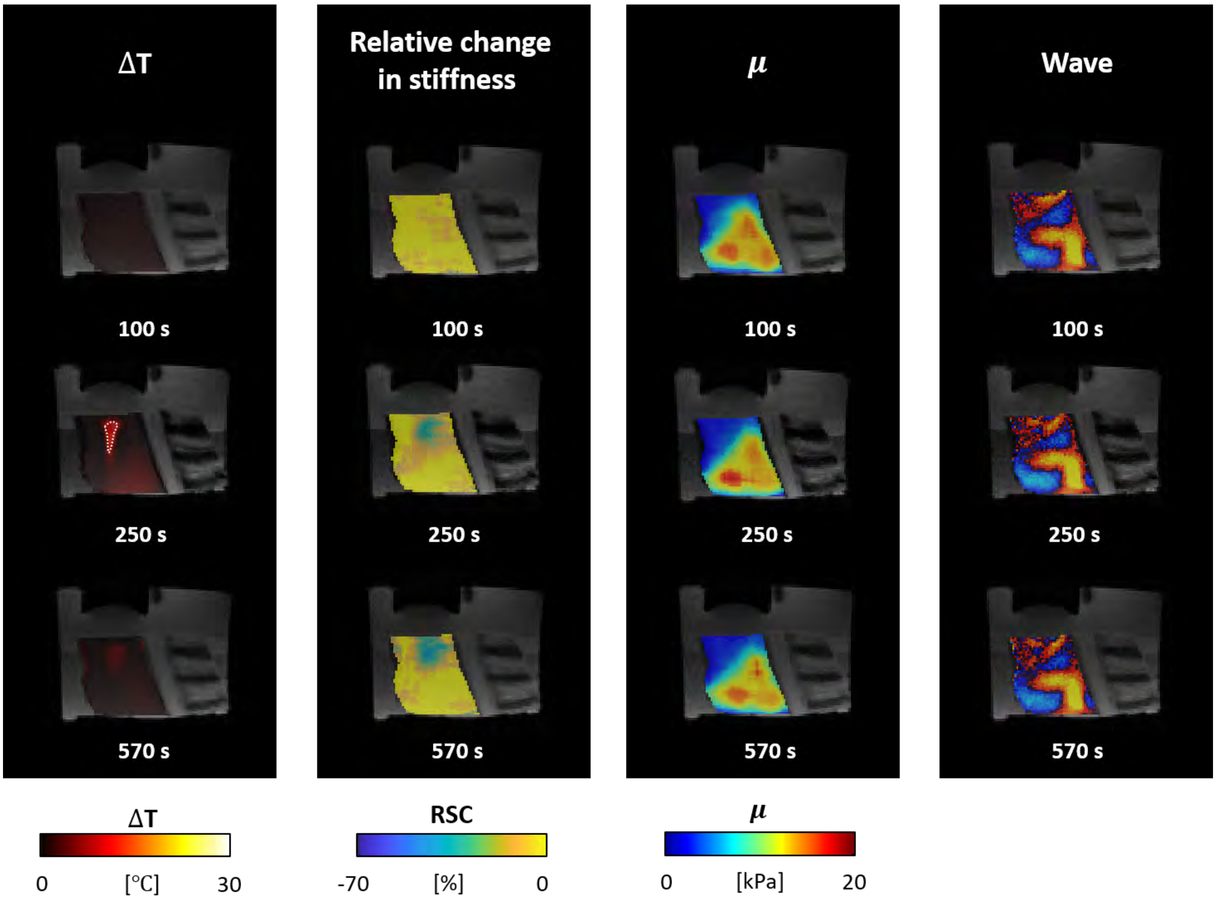

Figure 4.19 Result of experiment #4 (second heating / Sample 2). From left to right, temperature changes (ΔT), relative stiffness change (RSC), elasticity maps (μ), and wave images overlaid with the magnitude image at the first TE, before (time 100 s), during (time 250 s) HIFU heating and after, during the cooling time (time 570 s).

ΔT and RSC were averaged within an ROI that was automatically computed as the region including all pixels exceeding 66.7% of the maximum peak temperature around the focal spot. Time-dependent profiles of ΔT and RSC for the four samples are plotted in Figure 4.20. Shear moduli were found to decrease by 34.3±7.7 % (Exp.#1), 17.9±10.0 % (Exp.#2), 58.7±3.9 % (Exp.#3), and 36.7±6.7 % (Exp.#4) as a result of moderate temperature increase of 22.5±4.2℃, 14.0±2.8℃, 14.7±3.7℃, and 14.5±3.0℃ (Exp.#1-#4).

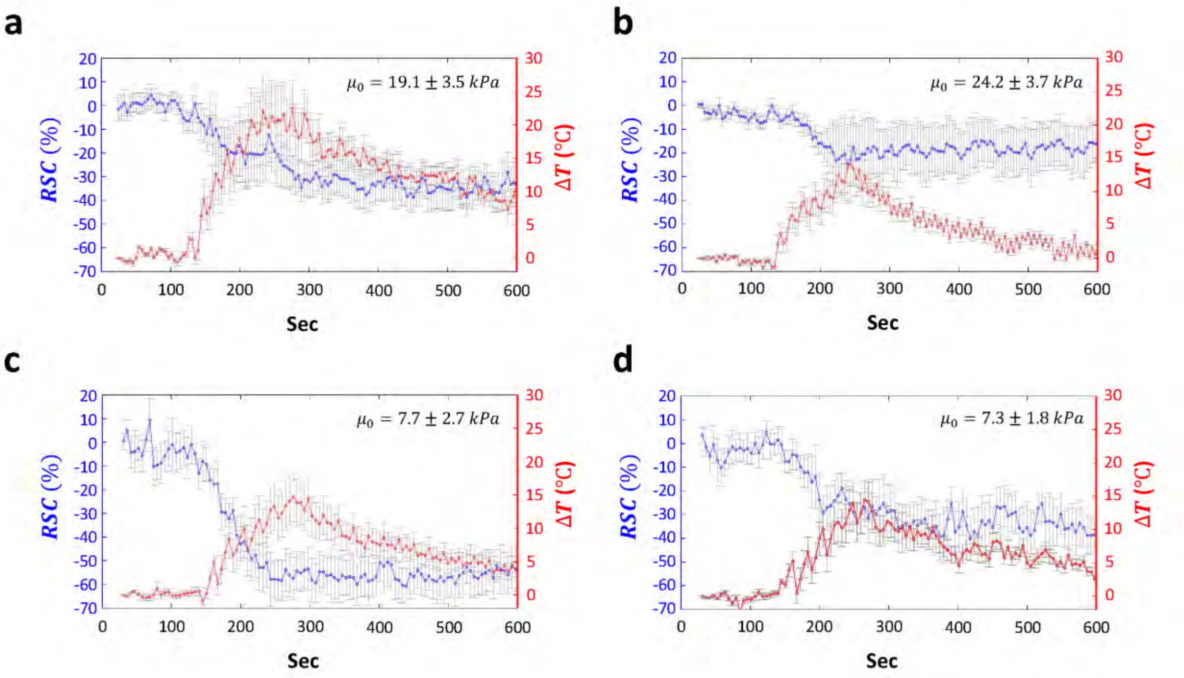

Figure 4.20 Time-dependent profiles of relative stiffness change (RSC) and temperature change ΔT for Exp.#1 (a), #2 (b), #3 (c), and #4 (d). ROIs were selected at the region over 66.7% of peak temperature in the focal spot (White-dashed line in Figure 4.16-19).

4.5 Discussion

In this study, the proposed method for simultaneous FRPRFS thermometry and MRE allows monitoring changes in both elasticity and temperature. In addition, this technique allows for correcting field drifts and for measuring temperature in all soft tissues, including fatty tissues. Standard MRE sequences rely on image acquisitions at a single echo time for all MRE phase offsets. In this study, the echo time is increased at each MRE phase offset. This approach with varying echo time makes it possible to perform chemical shift water-fat separation that will be used for FRPRFS thermometry. In MRE reconstruction, the LFE algorithm is processed on the spatial wave patterns created in the phase images and their spatial periodicity. Thus, varying TE has a minimum impact in the calculation of the elasticity maps.

Standard MRE sequences include specific high amplitude bipolar MSG, which may lead to further field drifts when repeated over time. FRPRFS allows correcting errors induced by such field drifts and by fat in tissues (Hofstetter et al., 2012). The proposed acquisition scheme keeps the acquisition time identical to previously developed real-time PRFS thermometry and MRE, while allowing for robust FRPRFS thermometry (Corbin et al., 2016b).

In PRFS calculation, temperature estimation is based on phase shifts of water protons. However, in fatty tissues, the global phase of mixed water and fat protons does not follow this phase shift by 0.01 ppm/℃ because the resonance frequency of the fat is not sensitive to temperature. (Rieke and Pauly, 2008a) investigated PRFS errors induced by the presence of fat and they proposed a method using echo combination to reduce the errors. This approach is based on the fact that PRFS errors due to the presence of fat display a periodicity with respect to temperature variation and echo time. In contrast, FRPRFS Thermometry can measure temperature from phase shifts of water protons present in fat containing tissue. In our experiment for temperature validation, we observed that regular PRFS measurements had significant errors in fat containing phantoms compared to the fiber optic measurements as shown in Figure 4.21. In addition, as expected, the errors were found to be dependent on the echo time.

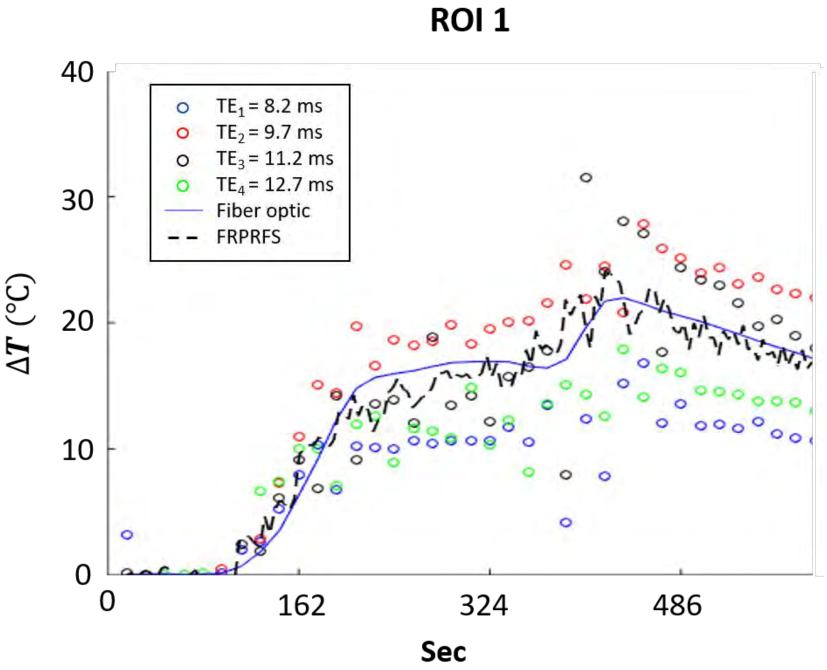

Figure 4.21 PRFS Thermometry in ROI 1. This shows the influence on the TE on the error of temperature estimates. B_0 field drifts are corrected using phase changes in an ROI distant from the heating region.

All experiments demonstrated that the proposed method can be an interesting monitoring solution during hyperthermia, and particularly during HIFU heating. Different changes of temperature and shear modulus were observed in muscle tissue because of its heterogeneity, due to variability in the organization of the muscular fibers or fat infiltration. These variations may be found in other muscle tissues, even in other parts of the same tissue (Sapin-de Brosses et al., 2010). Muscle tissue was found to soften during limited hyperthermia. This behavior has already been reported previously by several teams. Wu et al. reported a decrease of bovine muscle shear modulus by almost 50% up to 60 °C ex-vivo, followed by significant stiffening at temperatures higher than 60°C. Similar trends were reported by (Sapin-de Brosses et al., 2010) and (Arnal et al., 2011) in ex-vivo tissue. These studies suggest that muscle tissue softening occurring at moderate temperature elevation may be due to protein structure unfolding. Although this study did not illustrate the effect of heating at higher temperatures, it demonstrated clearly the thermal effects on tissue biomechanical properties.

In this study, a new framework was developed for FRPRFS thermometry coupled with MRE for the monitoring of thermal ablations in real time. This protocol was validated in gel phantoms and in porcine rib tissue ex-vivo. The acquisition strategy relies on the combination of multiple TEs and MRE phase offsets. The FRPRFS method is intended to provide accurate temperature measurements in all soft tissues, including fat-containing tissues. FRPRFS thermometry coupled with MRE may therefore help clinicians to monitor and evaluate thermal treatments in various types of tissues.

Chapter 5

5. General discussion

This chapter will describe important discussions that may deserve further attention.

1) Spatial constraints

The position of the pneumatic exciter is important to generate sufficient shear wave propagation. Combining an external MRE exciter with interventional material in vivo (HIFU or percutaneous) may be particularly challenging in terms of spatial access. This has led to alternative strategies, such as using percutaneous needles as a source of MRE excitation (Corbin et al., 2016b) or such as using the acoustic radiation force generated by the HIFU transducer (Hofstetter et al., 2019). In this Ph.D. study, it was possible to place both the HIFU transducer and the MRE exciter. With this setup, the built-in-spine coils or the in-bore body coils can be used for MR imaging. Translating this setup into an in vivo configuration would certainly require further considerations in order to enable simultaneous use of MRE together with an ablation device.

2) Elasticity reconstruction

In this Ph.D. study, elasticity maps are reconstructed by the LFE algorithm under the assumption of linear elastic material and incompressibility. The LFE algorithm is well-appreciated for clinical studies thanks to its fast and robust reconstruction. However, LFE methods may have lower spatial resolution and higher averaging effect than other reconstruction algorithms (Venkatesh and Ehman, 2014). This may lead to errors in shear modulus estimates around the focal region, especially at the onset of elasticity changes, as the region where such changes occur is very limited in size. Accuracy could be improved by increasing shear wave excitation frequency, thus decreasing the wavelength and improving MRE resolution. However, increasing excitation frequency affects shear wave penetration and may result in lower wave to noise ratio due to increased attenuation. Despite such potential limitations, the LFE algorithm is used in this study because its processing time is well suited for the monitoring of thermal ablations.

In chapters 3 and 4, echo times depended on both MSG frequency and additional TE lengthening due to SER or fat-water separation. The range of the selected TEs is acceptable to obtain sufficient SNR in gelatin phantom and ex-vivo tissue. Therefore, the various TEs used in this Ph.D. study do not cause a significant difference of the displacement sensitivity between slices with different TEs. However, some serious considerations remain for in-vivo studies, where T2* values may be substantially shorter than T2* of our phantoms. In such cases, it will be necessary to study the relationship between TE differences on elastogram quality.

3) *Temperature-induced susceptibility changes*

Changes in the magnetic field can lead to particularly significant errors in PRFS-based Thermometry, as well as in FRPRFS Thermometry. The field changes can be categorized by two parts: one is time-varying field inhomogeneities (B_0 field drifts) and the other is the effect of the magnetic susceptibility change.

In FRPRFS Thermometry, pure fat phase is used as a field camera, which can measure B_0 field variations without any temperature influence (not sensitive to temperature change). However, it doesn't take into account for the effect of the magnetic susceptibility change. (Sprinkhuizen et al., 2010) reported that temperature changes resulted in changes in the susceptibility distribution. This phenomenon becomes more evident for heterogeneous distributions of water and fat. For example, if pure water and pure fat parts are placed in heating area, temperature errors may vary in the range of -2.9 ℃ to +2.3 ℃ (Sprinkhuizen et al., 2010). However, the errors are highly variable depending on the spatial distribution of water and fat, the degree of homogeneity in that distribution, and size of heating area. In chapter 4, both phantom and rib tissue have homogeneous water-fat distributions so that temperature-induced susceptibility changes in the fat might be slight in these experiments. The FRPRFS measurement in the hot water tube experiment also showed no significant difference when compared to the optical fiber measurement. Further study is needed to compensate for temperature induced susceptibility changes of the fat when thermal ablation is applied to a tissue with heterogeneous fat distribution.

4) *Conclusion*

In this Ph.D. thesis, we have presented two different developments dedicated to interventional MRE and MRT. These works aimed at overcoming some of the current limitations of interventional MRE and MRT. In chapter 3, fast multislice MRE technique was investigated. The proposed method relied on the simultaneous echo refocusing MR technique. We have explored its potential for monitoring temperature and elasticity, simultaneously in several contiguous slices. The shear modulus in 4 slices was monitored and updated every 8.2 s. The results of all experiments presented in this study show how elasticity and temperature varied differently across slices, demonstrating therefore the importance of being able to monitor such changes in several slices. In chapter 4, a new acquisition scheme was presented that combines simultaneously the need for multiple TE acquisitions for the water-fat separation of FRPRFS, and for multiple MRE phase offsets for elastogram reconstructions. This study demonstrated the feasibility of monitoring thermal ablations with FRPRFS Thermometry together with MRE at a frame rate of 4.1s, even in fat-containing tissues. This allows improving PRFS MR Thermometry, while keeping the acquisition time unchanged. Although the results shown in this Ph.D. study are preliminary, the proposed methods show that it is possible to overcome some of the most significant limitations of prior MRT and MRE methods for monitoring thermal ablations. As a further, more fundamental study, it would be interesting to study the relationship between elasticity, temperature, and thermal dose using the proposed techniques. In this study, temperature has increased by 14 ℃ to 44 ℃. This temperature range may cause tissue coagulation with an initial temperature is 37 ℃. However, all experiments in this Ph.D. study were performed with an initial temperature of around 19 ℃ (room temperature). Hence the reached temperature is not sufficient to reach protein coagulation or tissue necrosis. Further ex-vivo studies at higher temperature are highly desirable to monitor elasticity changes in the ablated tissues. Alternatively, in-vivo study can be performed to observe changes in biological tissue during thermal ablations. The proposed methods presented here were not combined with compensation for susceptibility- and motion-related signal errors. To expand into in-vivo study, further improvements need to include these compensations.

Bibliography

Aarts, B.M., Klompenhouwer, E.G., Rice, S.L., Imani, F., Baetens, T., Bex, A., Horenblas, S., Kok, M., Haanen, J.B.A.G., Beets-Tan, R.G.H., Gómez, F.M., 2019. Cryoablation and immunotherapy: an overview of evidence on its synergy. Insights Imaging 10. https://doi.org/10.1186/s13244-019-0727-5

Abragam, A., 1961. The Principles of Nuclear Magnetism. Clarendon Press.

Anderson, L.J., Holden, S., Davis, B., Prescott, E., Charrier, C.C., Bunce, N.H., Firmin, D.N., Wonke, B., Porter, J., Walker, J.M., Pennell, D.J., 2001. Cardiovascular T2-star (T2*) magnetic resonance for the early diagnosis of myocardial iron overload. Eur. Heart. J. 22, 2171–2179. https://doi.org/10.1053/euhj.2001.2822

Arani, A., Arunachalam, S.P., Chang, I.C.Y., Baffour, F., Rossman, P.J., Glaser, K.J., Trzasko, J.D., McGee, K.P., Manduca, A., Grogan, M., Dispenzieri, A., Ehman, R.L., Araoz, P.A., 2017. Cardiac MR elastography for quantitative assessment of elevated myocardial stiffness in cardiac amyloidosis. J. Magn. Reson. Imaging 46, 1361–1367. https://doi.org/10.1002/jmri.25678

Arnal, B., Pernot, M., Tanter, M., 2011. Monitoring of thermal therapy based on shear modulus changes: II. Shear wave imaging of thermal lesions. IEEE Trans. Ultrason. Ferroelectr. Freq. Control 58, 1603–1611. https://doi.org/10.1109/TUFFC.2011.1987

Baron, P., Ries, M., Deckers, R., de Greef, M., Tanttu, J., Köhler, M., Viergever, M.A., Moonen, C.T.W., Bartels, L.W., 2014. In vivo T2 -based MR thermometry in adipose tissue layers for high-intensity focused ultrasound near-field monitoring. Magn. Reson. Med. 72, 1057–1064. https://doi.org/10.1002/mrm.25025

Baust, J.G., Gage, A.A., Johansen, T.E.B., Baust, J.M., 2014. Mechanisms of Cryoablation: Clinical Consequences on Malignant Tumors. Cryobiology 68, 1–11. https://doi.org/10.1016/j.cryobiol.2013.11.001

Bernstein, M., King, K., Zhou, X., 2004. Handbook of MRI Pulse Sequences. Academic Press.

Bitton, R.R., Webb, T.D., Pauly, K.B., Ghanouni, P., 2016. Improving thermal dose accuracy in magnetic resonance-guided focused ultrasound surgery: Long-term thermometry using a prior baseline as a reference. J. Magn. Reson. Imaging 43, 181–189. https://doi.org/10.1002/jmri.24978

Bleier, A.R., Jolesz, F.A., Cohen, M.S., Weisskoff, R.M., Dalcanton, J.J., Higuchi, N., Feinberg, D.A., Rosen, B.R., McKinstry, R.C., Hushek, S.G., 1991. Real-time magnetic resonance imaging of laser heat deposition in tissue. Magn. Reson. Med. 21, 132–137.

Borman, P.T.S., Bos, C., de Boorder, T., Raaymakers, B.W., Moonen, C.T.W., Crijns, S.P.M., 2016. Towards real-time thermometry using simultaneous multislice MRI. Phys. Med. Biol. 61, N461-477. https://doi.org/10.1088/0031-9155/61/17/N461

Brace, C., 2011. Thermal Tumor Ablation in Clinical Use. IEEE Pulse 2, 28–38. https://doi.org/10.1109/MPUL.2011.942603

Brace, C.L., 2009. Radiofrequency and Microwave Ablation of the Liver, Lung, Kidney, and Bone: What Are the Differences? Curr. Probl. Diagn. Radiol. 38, 135–143. https://doi.org/10.1067/j.cpradiol.2007.10.001

Breuer, F.A., Blaimer, M., Heidemann, R.M., Mueller, M.F., Griswold, M.A., Jakob, P.M., 2005. Controlled aliasing in parallel imaging results in higher acceleration (CAIPIRINHA) for multi-slice imaging. Magn. Reson. Med. 53, 684–691. https://doi.org/10.1002/mrm.20401

Carpentier, A., Chauvet, D., Reina, V., Beccaria, K., Leclerq, D., McNichols, R.J., Gowda, A., Cornu, P., Delattre, J.Y., 2012. MR-guided laser-induced thermal therapy (LITT) for recurrent glioblastomas. Laser. Surg. Med. 44, 361–368. https://doi.org/10.1002/lsm.22025

Chatelin, S., Charpentier, I., Corbin, N., Meylheuc, L., Vappou, J., 2016. An automatic differentiation-based gradient method for inversion of the shear wave equation in magnetic resonance elastography: specific application in fibrous soft tissues. Phys. Med. Biol. 61, 5000–5019. https://doi.org/10.1088/0031-9155/61/13/5000

Chen, J., Woodrum, D.A., Glaser, K.J., Murphy, M.C., Gorny, K., Ehman, R., 2014. Assessment of in vivo laser ablation using MR elastography with an inertial driver. Magn. Reson. Med. 72, 59–67. https://doi.org/10.1002/mrm.24891

Clasen, S., Pereira, P.L., 2008. Magnetic resonance guidance for radiofrequency ablation of liver tumors. J. Magn. Reson. Imaging 27, 421–433. https://doi.org/10.1002/jmri.21264

Corbin, N., Pramod, R., Barbé, L., Renaud, P., Mathelin, M. de, Breton, E., Vappou, J., 2016a. In vivo monitoring of percutaneous thermal ablation by simultaneous MR Elastography and Thermometry. Proc. Intl. Soc. Mag. Reson. Med. 24, Singapore.

Corbin, N., Vappou, J., Breton, E., Boehler, Q., Barbé, L., Renaud, P., de Mathelin, M., 2016b. Interventional MR elastography for MRI-guided percutaneous procedures. Magn. Reson. Med. 75, 1110–1118. https://doi.org/10.1002/mrm.25694

d'Arsonval, M., 1891. Action physiologique des courants alternatifs. CR. Soc. Biol. 43, 283–286.

Decruze, S.B., Green, J.A., 2007. Hormone therapy in advanced and recurrent endometrial cancer: a systematic review. Int. J. Gyn. Cancer 17, 964–978. https://doi.org/10.1111/j.1525-1438.2007.00897.x

Dick, E.A., Joarder, R., de Jode, M., Taylor-Robinson, S.D., Thomas, H.C., Foster, G.R., Gedroyc, W.M.W., 2003. MR-guided Laser Thermal Ablation of Primary and Secondary Liver Tumours. Clin. Radiol. 58, 112–120. https://doi.org/10.1053/crad.2002.1129

Diederich, C.J., 2005. Thermal ablation and high-temperature thermal therapy: Overview of technology and clinical implementation. Int. J. Hyperthermia 21, 745–753. https://doi.org/10.1080/02656730500271692

Dubinsky, T.J., Cuevas, C., Dighe, M.K., Kolokythas, O., Hwang, J.H., 2008. High-intensity focused ultrasound: current potential and oncologic applications. AJR. Am. J. Roentgenol 190, 191–199. https://doi.org/10.2214/AJR.07.2671

Ebersole, C., Ahmad, R., Rich, A.V., Potter, L.C., Dong, H., Kolipaka, A., 2018. A bayesian method for accelerated magnetic resonance elastography of the liver. Magn. Reson. Med. 80, 1178–1188. https://doi.org/10.1002/mrm.27083

Feinberg, D.A., Reese, T.G., Wedeen, V.J., 2002. Simultaneous echo refocusing in EPI. Magn. Reson. Med. 48, 1–5. https://doi.org/10.1002/mrm.10227

Feinberg, D.A., Setsompop, K., 2013. Ultra-fast MRI of the human brain with simultaneous multi-slice imaging. J. Magn. Reson. 229, 90–100. https://doi.org/10.1016/j.jmr.2013.02.002

Ferlay, J., Colombet, M., Soerjomataram, I., Dyba, T., Randi, G., Bettio, M., Gavin, A., Visser, O., Bray, F., 2018. Cancer incidence and mortality patterns in Europe: Estimates for 40 countries and 25 major cancers in 2018. Eur. J. Cancer 103, 356–387. https://doi.org/10.1016/j.ejca.2018.07.005

Fielden, S.W., Feng, X., Zhao, L., Miller, G.W., Geeslin, M., Dallapiazza, R.F., Elias, W.J., Wintermark, M., Butts Pauly, K., Meyer, C.H., 2018. A spiral-based volumetric acquisition for MR temperature imaging. Magn. Reson. Med. 79, 3122–3127. https://doi.org/10.1002/mrm.26981

Fry, W.J., Fry, F.J., Barnard, J.W., Krumins, R.F., Brennan, J.F., 1955. Ultrasonic Lesions in the Mammalian Central Nervous System. Science 122, 517–518. https://doi.org/10.1126/science.122.3168.517

Garnon, J., Tsoumakidou, G., Enescu, I., Buy, X., Gangi, A., 2013. Overview of Thermal Ablation Devices: HIFU, Laser Interstitial, Chemical Ablation, in: Clark, T., Sabharwal, T., Interventional Radiology Techniques in Ablation, Techniques in Interventional Radiology. Springer London, London, pp. 29–41. https://doi.org/10.1007/978-0-85729-094-6_5

Garteiser, P., Sahebjavaher, R.S., Beek, T., C, L., Salcudean, S., Vilgrain, V., Beers, V., E, B., Sinkus, R., 2013. Rapid acquisition of multifrequency, multislice and multidirectional MR elastography data with a fractionally encoded gradient echo sequence. NMR. Biomed. 26, 1326–1335. https://doi.org/10.1002/nbm.2958

Goldstein, R.M., Zebker, H.A., Werner, C.L., 1988. Satellite radar interferometry: Two-dimensional phase unwrapping. Radio. Science 23, 713–720. https://doi.org/10.1029/RS023i004p00713

Guenthner, C., Kozerke, S., 2018. Encoding and readout strategies in magnetic resonance elastography. NMR. Biomed. 31, e3919. https://doi.org/10.1002/nbm.3919

Guenthner, C., Runge, J., Sinkus, R., Kozerke, S., 2017. Simultaneous Multislice Acquisition for Magnetic Resonance Elastography. Proc. Intl. Soc. Mag. Reson. Med. 25, Honolulu, HI, USA.

Guenthner, C., Sethi, S., Troelstra, M., Dokumaci, A.S., Sinkus, R., Kozerke, S., 2019. Ristretto MRE: A generalized multi-shot GRE-MRE sequence. NMR. Biomed. 32, e4049. https://doi.org/10.1002/nbm.4049

Hayashi, A.H., Silver, S.F., van der Westhuizen, N.G., Donald, J.C., Parker, C., Fraser, S., Ross, A.C., Olivotto, I.A., 2003. Treatment of invasive breast carcinoma with ultrasound-guided radiofrequency ablation. Am. J. Surg. 185, 429–435. https://doi.org/10.1016/S0002-9610(03)00061-8

Hernando, D., Liang, Z.P., Kellman, P., 2010. Chemical Shift-Based Water/Fat Separation: A Comparison of Signal Models. Magn. Reson. Med. 64, 811–822. https://doi.org/10.1002/mrm.22455

Hibst, R., 1992. Mechanical effects of erbium:YAG laser bone ablation. Laser. Surg. Med. 12, 125–130. https://doi.org/10.1002/lsm.1900120203

Hindman, J.C., 1966. Proton Resonance Shift of Water in the Gas and Liquid States. J. Chem. Phys. 44, 4582–4592. https://doi.org/10.1063/1.1726676

Hofstetter, L.W., Odéen, H., Bolster, B.D., Mueller, A., Christensen, D.A., Payne, A., Parker, D.L., 2019. Efficient shear wave elastography using transient acoustic radiation force excitations and MR displacement encoding. Magn. Reson. Med. 81, 3153–3167. https://doi.org/10.1002/mrm.27647

Hofstetter, L.W., Yeo, D.T.B., Dixon, W.T., Kempf, J.G., Davis, C.E., Foo, T.K., 2012. Fat-referenced MR thermometry in the breast and prostate using IDEAL. J. Magn. Reson. Imaging 36, 722–732. https://doi.org/10.1002/jmri.23692

Ishihara, Y., Calderon, A., Watanabe, H., Okamoto, K., Suzuki, Yoshinori, Kuroda, K., Suzuki, Yutaka, 1995. A precise and fast temperature mapping using water proton chemical shift. Magn. Reson. Med. 34, 814–823. https://doi.org/10.1002/mrm.1910340606

Jain, R.K., Ward-Hartley, K., 1984. Tumor Blood Flow-Characterization, Modifications, and Role in Hyperthermia. IEEE Trans. Son. Ultra. 31, 504–525. https://doi.org/10.1109/T-SU.1984.31536

Johnson, C.L., Holtrop, J.L., Anderson, A.T., Sutton, B.P., 2016. Brain MR elastography with multiband excitation and nonlinear motion-induced phase error correction. Presented at the Proc. Intl. Soc. Mag. Reson. Med. 24, Singapore.

Jolesz, F.A., 2009. MRI-Guided Focused Ultrasound Surgery. Annu. Rev. Med. 60, 417–430. https://doi.org/10.1146/annurev.med.60.041707.170303

Kahn, T., Busse, H. 2012. Interventional Magnetic Resonance Imaging, Diagnostic Imaging. Springer-Verlag, Berlin Heidelberg.

Kruse, S.A., Smith, J.A., Lawrence, A.J., Dresner, M.A., Manduca, A., Greenleaf, J.F., Ehman, R.L., Kruse, S.A., Smith, J.A., Lawrence, A.J., Dresner, M.A., Manduca, A., Greenleaf, J.F., 2000. Tissue characterization using magnetic resonance elastography: preliminary results. Phys. Med. Biol. 45, 1579. https://doi.org/10.1088/0031-9155/45/6/313

Kwon, O.I., Chauhan, M., Kim, H.J., Jeong, W.C., Wi, H., Oh, T.I., Woo, E.J., 2014. Fast conductivity imaging in magnetic resonance electrical impedance tomography (MREIT) for RF ablation monitoring. Int. J. Hyperthermia 30, 447–455. https://doi.org/10.3109/02656736.2014.966337

Lake, R.A., Robinson, B.W.S., 2005. Immunotherapy and chemotherapy-a practical partnership. Nat. Rev. Cancer 5, 397–405. https://doi.org/10.1038/nrc1613

Lam, M.K., Greef, M. de, Bouwman, J.G., Moonen, C.T.W., Viergever, M.A., Bartels, L.W., 2015. Multi-gradient echo MR thermometry for monitoring of the near-field area during MR-guided high intensity focused ultrasound heating. Phys. Med. Biol. 60, 7729. https://doi.org/10.1088/0031-9155/60/19/7729

Lande, M.B., Donovan, J.M., Zeidel, M.L., 1995. The relationship between membrane fluidity and permeabilities to water, solutes, ammonia, and protons. J. Gen. Physiol. 106, 67–84. https://doi.org/10.1085/jgp.106.1.67

Larkman, D.J., Hajnal, J.V., Herlihy, A.H., Coutts, G.A., Young, I.R., Ehnholm, G., 2001. Use of multicoil arrays for separation of signal from multiple slices simultaneously excited. J. Magn. Reson. Imaging 13, 313–317. https://doi.org/10.1002/1522-2586(200102)13:2<313::AID-JMRI1045>3.0.CO;2-W

Le Bihan, D., Delannoy, J., Levin, R.L., 1989. Temperature mapping with MR imaging of molecular diffusion: application to hyperthermia. Radiology 171, 853–857. https://doi.org/10.1148/radiology.171.3.2717764

Le, Y., Glaser, K., Rouviere, O., Ehman, R.L., Felmlee, J.P., 2006. Feasibility of simultaneous temperature and tissue stiffness detection by MRE. Magn. Reson. Med. 55, 700–705. https://doi.org/10.1002/mrm.20801

Lorenzato, C., Oerlemans, C., Cernicanu, A., Ries, M., de Senneville, B.D., Moonen, C., Bos, C., 2014. Rapid dynamic R1/R2*/temperature assessment: a method with potential for monitoring drug delivery. NMR Biomed. 27, 1267–1274. https://doi.org/10.1002/nbm.3182

Lu, W., Hargreaves, B.A., 2008. Multiresolution field map estimation using golden section search for water-fat separation. Magn. Reson. Med. 60, 236–244. https://doi.org/10.1002/mrm.21544

Lubner, M.G., Brace, C.L., Hinshaw, J.L., Lee, F.T., 2010. Microwave Tumor Ablation: Mechanism of Action, Clinical Results, and Devices. Journal of Vascular and Interventional Radiology, Thermal Ablation 2010: At the Crossroads of Past Success, Current Goals, and Future Technology 21, S192–S203. https://doi.org/10.1016/j.jvir.2010.04.007

MacLellan, C.J., Fuentes, D., Prabhu, S., Rao, G., Weinberg, J.S., Hazle, J.D., Stafford, R.J., 2018. A methodology for thermal dose model parameter development using perioperative MRI. Int. J. Hyperthermia 34, 687–696. https://doi.org/10.1080/02656736.2017.1363418

Manduca, A., Muthupillai, R., Rossman, P.J., Greenleaf, J.F., Ehman, R.L., 1996. Image processing for magnetic-resonance elastography, in: Medical Imaging 1996: Image Processing. Presented at the Medical Imaging 1996: Image Processing, International Society for Optics and Photonics, pp. 616–624. https://doi.org/10.1117/12.237965

Mariani, A., Kwiecinski, W., Pernot, M., Balvay, D., Tanter, M., Clement, O., Cuenod, C.A., Zinzindohoue, F., 2014. Real time shear waves elastography monitoring of thermal ablation: in vivo evaluation in pig livers. J. Surg. Res. 188, 37–43. https://doi.org/10.1016/j.jss.2013.12.024

Mariappan, Y.K., Glaser, K.J., Hubmayr, R.D., Manduca, A., Ehman, R.L., McGee, K.P., 2011. MR elastography of human lung parenchyma: technical development, theoretical modeling and in vivo validation. J. Magn. Reson. Imaging 33, 1351–1361. https://doi.org/10.1002/jmri.22550

McGahan, J.P., Dodd, G.D., 2001. Radiofrequency Ablation of the Liver. Am. J. Roentgenology 176, 3–16. https://doi.org/10.2214/ajr.176.1.1760003

McGarry, M.D.J., Johnson, C.L., Sutton, B.P., Georgiadis, J.G., Houten, E.E.W.V., Pattison, A.J., Weaver, J.B., Paulsen, K.D., 2015. Suitability of poroelastic and viscoelastic mechanical models for high and low frequency MR elastography. Med. Phys. 42, 947–957. https://doi.org/10.1118/1.4905048

Murphy, M.C., Huston, J., Glaser, K.J., Manduca, A., Meyer, F.B., Lanzino, G., Morris, J.M., Felmlee, J.P., Ehman, R.L., 2013. Preoperative assessment of meningioma stiffness using magnetic resonance elastography. J. Neurosurg. 118, 643–648. https://doi.org/10.3171/2012.9.JNS12519

Murphy, M.C., Huston, J., Jack, C.R., Glaser, K.J., Manduca, A., Felmlee, J.P., Ehman, R.L., 2011. Decreased brain stiffness in Alzheimer’s disease determined by magnetic resonance elastography. J. Magn. Reson. Imaging 34, 494–498. https://doi.org/10.1002/jmri.22707

Napoli, A., Anzidei, M., Marincola, B.C., Brachetti, G., Noce, V., Boni, F., Bertaccini, L., Passariello, R., Catalano, C., 2013a. MR Imaging–guided Focused Ultrasound for Treatment of Bone Metastasis. RadioGraphics 33, 1555–1568. https://doi.org/10.1148/rg.336125162

Napoli, A., Cartocci, G., Boni, F., Del Monte, M., Noce, V., Anzidei, M., Catalano, C., 2013b. Focused Ultrasound Therapy of the Prostate with MR Guidance. Curr. Radiol. Rep. 1, 154–160. https://doi.org/10.1007/s40134-013-0011-2

Nelder, J.A., Mead, R., 1965. A Simplex Method for Function Minimization. Comput. J. 7, 308–313. https://doi.org/10.1093/comjnl/7.4.308

Numano, T, Ito, D, Onishi, T, Mizuhara, K, Takamoto, K, Nishijyo, H, Misawa, M, Nitta, N, 2017. Integration of MR Elastography and Fat/Water Separation Imaging. Proc. Intl. Soc. Mag. Reson. Med. 25, Honolulu, HI, USA.

Nutting, C., Dearnaley, D.P., Webb, S., 2000. Intensity modulated radiation therapy: a clinical review. BJR 73, 459–469. https://doi.org/10.1259/bjr.73.869.10884741

Oliphant, T.E., Manduca, A., Ehman, R.L., Greenleaf, J.F., 2001. Complex-valued stiffness reconstruction for magnetic resonance elastography by algebraic inversion of the differential equation. Magn. Reson. Med. 45, 299–310.

Osaki, Y., Ikeda, K., Izumi, N., Yamashita, S., Kumada, H., Hatta, S., Okita, K., 2013. Clinical effectiveness of bipolar radiofrequency ablation for small liver cancers. J. Gastroenterol. 48, 874–883. https://doi.org/10.1007/s00535-012-0685-x

Oto, A., Sethi, I., Karczmar, G., McNichols, R., Ivancevic, M.K., Stadler, W.M., Watson, S., Eggener, S., 2013. MR Imaging–guided Focal Laser Ablation for Prostate Cancer: Phase I Trial. Radiology 267, 932–940. https://doi.org/10.1148/radiol.13121652

Ozhinsky, E., Han, M., Bucknor, M., Krug, R., Rieke, V., 2016. T2-based temperature monitoring in bone marrow for MR-guided focused ultrasound. J. Ther. Ultrasound 4, 26. https://doi.org/10.1186/s40349-016-0073-8

Pardoll, D.M., 2012. The blockade of immune checkpoints in cancer immunotherapy. Nat. Rev. Cancer 12, 252–264. https://doi.org/10.1038/nrc3239

Peng, H.-H., Huang, T.-Y., Tseng, W.-Y.I., Lin, E.-L., Chung, H.-W., Wu, C.-C., Wang, Y.-S., Chen, W.-S., 2009. Simultaneous temperature and magnetization transfer (MT) monitoring during high-intensity focused ultrasound (HIFU) treatment: preliminary investigation on ex vivo porcine muscle. J. Magn. Reson. Imaging 30, 596–605. https://doi.org/10.1002/jmri.21860

Pennes, H.H., 1948. Analysis of Tissue and Arterial Blood Temperatures in the Resting Human Forearm. Journal of Applied Physiology 1, 93–122. https://doi.org/10.1152/jappl.1948.1.2.93

Pepin, K.M., Ehman, R.L., McGee, K.P., 2015. Magnetic resonance elastography (MRE) in cancer: Technique, analysis, and applications. Prog. Nucl. Magn. Reson. Spectrosc. 0, 32–48. https://doi.org/10.1016/j.pnmrs.2015.06.001

Quesson, B., Laurent, C., Maclair, G., de Senneville, B.D., Mougenot, C., Ries, M., Carteret, T., Rullier, A., Moonen, C.T.W., 2011. Real-time volumetric MRI thermometry of focused ultrasound ablation in vivo: a feasibility study in pig liver and kidney. NMR Biomed. 24, 145–153. https://doi.org/10.1002/nbm.1563

Reeder, S.B., Wen, Z., Yu, H., Pineda, A.R., Gold, G.E., Markl, M., Pelc, N.J., 2004. Multicoil Dixon chemical species separation with an iterative least-squares estimation method. Magn. Reson. Med. 51, 35–45. https://doi.org/10.1002/mrm.10675

Rieke, V., Pauly, K.B., 2008a. Echo Combination to Reduce PRF Thermometry Errors From Fat. J. Magn. Reson. Imaging 27, 673–677. https://doi.org/10.1002/jmri.21238

Rieke, V., Pauly, K.B., 2008b. MR thermometry. J. Magn. Reson. Imaging 27, 376–390. https://doi.org/10.1002/jmri.21265

Rosenberg, C., Kickhefel, A., Mensel, B., Pickartz, T., Puls, R., Roland, J., Hosten, N., 2013. PRFS-Based MR Thermometry Versus an Alternative T1 Magnitude Method – Comparative Performance Predicting Thermally Induced Necrosis in Hepatic Tumor Ablation. PLOS ONE 8, e78559. https://doi.org/10.1371/journal.pone.0078559

Rouvière, O., Souchon, R., Pagnoux, G., Ménager, J.-M., Chapelon, J.-Y., 2011. MR Elastography of the kidneys: feasibility and reproducibility in young healthy adults. J. Magn. Reson. Imaging 34, 880–886. https://doi.org/10.1002/jmri.22670

Rump, J., Klatt, D., Braun, J., Warmuth, C., Sack, I., 2007. Fractional encoding of harmonic motions in MR elastography. Magn. Reson. Med. 57, 388–395. https://doi.org/10.1002/mrm.21152

Sack, I., Beierbach, B., Hamhaber, U., Klatt, D., Braun, J., 2008. Non-invasive measurement of brain viscoelasticity using magnetic resonance elastography. NMR Biomed. 21, 265–271. https://doi.org/10.1002/nbm.1189

Sapareto, S.A., Dewey, W.C., 1984. Thermal dose determination in cancer therapy. Int. J. Radiat. Oncol. Biol. Phys. 10, 787–800.

Sapin-de Brosses, E., Gennisson, J.-L., Pernot, M., Fink, M., Tanter, M., 2010. Temperature dependence of the shear modulus of soft tissues assessed by ultrasound. Phys. Med. Biol. 55, 1701–1718. https://doi.org/10.1088/0031-9155/55/6/011

Sedaghat, F., Tuncali, K., 2018. Enabling Technology for MRI-Guided Intervention. Top. Magn. Reson. Imaging 27, 5–8. https://doi.org/10.1097/RMR.0000000000000148

Setsompop, K., Gagoski, B.A., Polimeni, J.R., Witzel, T., Wedeen, V.J., Wald, L.L., 2011. Blipped-controlled aliasing in parallel imaging for simultaneous multislice echo planar imaging with reduced g-factor penalty. Magn. Reson. Med. 67, 1210–1224. https://doi.org/10.1002/mrm.23097

Shah, T.T., Arbel, U., Foss, S., Zachman, A., Rodney, S., Ahmed, H.U., Arya, M., 2016. Modeling Cryotherapy Ice Ball Dimensions and Isotherms in a Novel Gel-based Model to Determine Optimal Cryo-needle Configurations and Settings for Potential Use in Clinical Practice. Urology 91, 234–240. https://doi.org/10.1016/j.urology.2016.02.012

Shi, Y., Glaser, K.J., Venkatesh, S.K., Ben-Abraham, E.I., Ehman, R.L., 2015. Feasibility of using 3D MR elastography to determine pancreatic stiffness in healthy volunteers. J. Magn. Reson. Imaging 41, 369–375. https://doi.org/10.1002/jmri.24572

Simon, C.J., Dupuy, D.E., Mayo-Smith, W.W., 2005. Microwave Ablation: Principles and Applications. RadioGraphics 25, S69–S83. https://doi.org/10.1148/rg.25si055501

Sinkus, R., Tanter, M., Xydeas, T., Catheline, S., Bercoff, J., Fink, M., 2005. Viscoelastic shear properties of in vivo breast lesions measured by MR elastography. Magn. Reson. Imaging 23, 159–165. https://doi.org/10.1016/j.mri.2004.11.060

Soher, B.J., Wyatt, C., Reeder, S.B., MacFall, J.R., 2010. Noninvasive temperature mapping with MRI using chemical shift water-fat separation. Magn. Reson. Med. 63, 1238–1246. https://doi.org/10.1002/mrm.22310

Souchon, R., Salomir, R., Beuf, O., Milot, L., Grenier, D., Lyonnet, D., Chapelon, J.-Y., Rouvière, O., 2008. Transient MR elastography (t-MRE) using ultrasound radiation force: Theory, safety, and initial experiments in vitro. Magn. Reson. Med. 60, 871–881. https://doi.org/10.1002/mrm.21718

Sprinkhuizen, S.M., Konings, M.K., Bom, M.J. van der, Viergever, M.A., Bakker, C.J.G., Bartels, L.W., 2010. Temperature-induced tissue susceptibility changes lead to significant temperature errors in PRFS-based MR thermometry during thermal interventions. Magn. Reson. Med. 64, 1360–1372. https://doi.org/10.1002/mrm.22531

Stafford, R.J., Kallel, F., Price, R.E., Cromeens, D.M., Krouskop, T.A., Hazle, J.D., Ophir, J., 1998. Elastographic imaging of thermal lesions in soft tissue: a preliminary study in vitro. Ultrasound Med. Bio. 24, 1449–1458. https://doi.org/10.1016/S0301-5629(98)00099-4

Sui, Y., Yin, Z., Rossman, P., Murphy, M., Trzasko, J.D., Scott, J., Glaser, K., McGee, K.P., Bernstein, M., Ehman, R.L., Huston, J., 2019. Fast Brain MR Elastography Using a Simultaneous Multislice EPI Acquisition on a Compact 3T Scanner. Proc. Intl. Soc. Mag. Reson. Med. 27, Montreal, QC, Canada.

Taouli, B., Ehman, R.L., Reeder, S.B., 2009. Advanced MRI Methods for Assessment of Chronic Liver Disease. Am. J. Roentgenology 193, 14–27. https://doi.org/10.2214/AJR.09.2601

Taylor, B.A., Elliott, A.M., Hwang, K.P., Shetty, A., Hazle, J.D., Stafford, R.J., 2011. Measurement of temperature dependent changes in bone marrow using a rapid chemical shift imaging technique. J. Magn. Reson. Imaging 33, 1128–1135. https://doi.org/10.1002/jmri.22537

Taylor, B.A., Hwang, K.P., Elliott, A.M., Shetty, A., Hazle, J.D., Stafford, R.J., 2008. Dynamic chemical shift imaging for image-guided thermal therapy: analysis of feasibility and potential. Med. Phys. 35, 793–803. https://doi.org/10.1118/1.2831915

Tempel, N. van den, Horsman, M.R., Kanaar, R., 2016. Improving efficacy of hyperthermia in oncology by exploiting biological mechanisms. Int. J. Hyperthermia 32, 446–454. https://doi.org/10.3109/02656736.2016.1157216

Todd, N., Diakite, M., Payne, A., Parker, D.L., 2014. In vivo evaluation of multi-echo hybrid PRF/T1 approach for temperature monitoring during breast MR-guided focused ultrasound surgery treatments. Magn. Reson. Med. 72, 793–799. https://doi.org/10.1002/mrm.24976

Toraya-Brown, S., Fiering, S., 2014. Local tumour hyperthermia as immunotherapy for metastatic cancer. Int. J. Hyperthermia 30, 531–539. https://doi.org/10.3109/02656736.2014.968640

Trzasko, J, Kugel, J, Grimm, R, Glaser, K, Manduca, A, Araoz, P, Ehman R. L., 2015. Simultaneous MR Elastography and Fat+Water Imaging. Proc. Intl. Soc. Mag. Reson. Med. 23, Toronto, Ontario, Canada.

Tsao, J., Jiang, Y., 2013. Hierarchical IDEAL: Fast, robust, and multiresolution separation of multiple chemical species from multiple echo times. Magn. Reson. Med. 70, 155–159. https://doi.org/10.1002/mrm.24441

Tsoumakidou, G., Breton, E., Garnon, J., Buy, X., Mathelin, M. de, Gangi, A., 2012. Interventional non-vascular MRI: magnet designs, equipment requirements, materials, technical considerations, and sequences. ECR 2012. http://dx.doi.org/10.1594/ecr2012/C-2499

Uffmann, K., Abicht, C., Grote, W., Quick, H.H., Ladd, M.E., 2002. Design of an MR-compatible piezoelectric actuator for MR elastography. Concepts in Magnetic Resonance 15, 239–254. https://doi.org/10.1002/cmr.10045

Van Houten, E.E., Paulsen, K.D., Miga, M.I., Kennedy, F.E., Weaver, J.B., 1999. An overlapping subzone technique for MR-based elastic property reconstruction. Magn. Reson. Med. 42, 779–786.

van Rhoon, G.C., Samaras, T., Yarmolenko, P.S., Dewhirst, M.W., Neufeld, E., Kuster, N., 2013. CEM43°C thermal dose thresholds: a potential guide for magnetic resonance radiofrequency exposure levels? Eur. Radiol. 23, 2215–2227. https://doi.org/10.1007/s00330-013-2825-y

Vappou, J., Bour, P., Marquet, F., Ozenne, V., Quesson, B., 2018. MR-ARFI-based method for the quantitative measurement of tissue elasticity: application for monitoring HIFU therapy. Phys. Med. Biol. 63, 095018. https://doi.org/10.1088/1361-6560/aabd0d

Vappou, J., Breton, E., Choquet, P., Goetz, C., Willinger, R., Constantinesco, A., 2007. Magnetic resonance elastography compared with rotational rheometry for in vitro brain tissue viscoelasticity measurement. Magn. Reson. Mater. Phy. 20, 273. https://doi.org/10.1007/s10334-007-0098-7

Vaupel, P., Kallinowski, F., 1987. Physiological Effects of Hyperthermia, in: Streffer, C. (Ed.), Hyperthermia and the Therapy of Malignant Tumors, Recent Results in Cancer Research. Springer Berlin, Berlin, Heidelberg, pp. 71–109. https://doi.org/10.1007/978-3-642-82955-0_3

Vaupel, P., Kallinowski, F., Okunieff, P., 1989. Blood Flow, Oxygen and Nutrient Supply, and Metabolic Microenvironment of Human Tumors: A Review. Cancer. Res. 49, 6449–6465.

Venkatesh, S.K., Ehman, R.L., 2014. Magnetic Resonance Elastography. Springer-Verlag.

Venkatesh S.K., Yin M., Ehman R. L., 2013. Magnetic resonance elastography of liver: Technique, analysis, and clinical applications. J. Magn. Reson. Imaging 37, 544–555. https://doi.org/10.1002/jmri.23731

Vígh, L., Maresca, B., 2002. Chapter 12 - Dual Role of Membranes in Heat Stress: As Thermosensors They Modulate the Expression of Stress Genes and, by Interacting with Stress Proteins, Re-organize Their Own Lipid Order and Functionality, in: Storey, K.B., Storey, J.M. (Eds.), Cell and Molecular Response to Stress, Sensing, Signaling and Cell Adaptation. Elsevier, pp. 173–187. https://doi.org/10.1016/S1568-1254(02)80014-6

Weidensteiner, C., Quesson, B., Caire-Gana, B., Kerioui, N., Rullier, A., Trillaud, H., Moonen, C.T.W., 2003. Real-time MR temperature mapping of rabbit liver in vivo during thermal ablation. Magn. Reson. Med. 50, 322–330. https://doi.org/10.1002/mrm.10521

Wells, P.N.T., 1975. Absorption and dispersion of ultrasound in biological tissue. Ultrasound Med. Bio. 1, 369–376. https://doi.org/10.1016/0301-5629(75)90124-6

Wood, R.W., Loomis, A.L., 1927. The physical and biological effects of high-frequency sound-waves of great intensity. Lond. Edinb. Dubl. Phil. Mag. 4, 417–436. https://doi.org/10.1080/14786440908564348

Wu, T., Felmlee, J.P., Greenleaf, J.F., Riederer, S.J., Ehman, R.L., 2001. Assessment of thermal tissue ablation with MR elastography. Magn. Reson. Med. 45, 80–87. https://doi.org/10.1002/1522-2594(200101)45:1<80::AID-MRM1012>3.0.CO;2-Y

Wu, T., Felmlee, J.P., Greenleaf, J.F., Riederer, S.J., Ehman, R.L., 2000. MR imaging of shear waves generated by focused ultrasound. Magn. Reson. Med. 43, 111–115. https://doi.org/10.1002/(SICI)1522-2594(200001)43:1<111::AID-MRM13>3.0.CO;2-D

Wu, X., Zhang, K., Chen, Y., Wang, R., Chen, L., Zhang, A., Hu, B., 2018. Theoretical and experimental study of dual-fiber laser ablation for prostate cancer. PLOS ONE 13. https://doi.org/10.1371/journal.pone.0206065

Wyatt, C.R., Soher, B.J., MacFall, J.R., 2010. Correction of breathing-induced errors in magnetic resonance thermometry of hyperthermia using multiecho field fitting techniques. Med. Phys. 37, 6300–6309. https://doi.org/10.1118/1.3515462

Yin, M., Woollard, J., Wang, X., Torres, V.E., Harris, P.C., Ward, C.J., Glaser, K.J., Manduca, A., Ehman, R.L., 2007. Quantitative assessment of hepatic fibrosis in an animal model with magnetic resonance elastography. Magn. Reson. Med. 58, 346–353. https://doi.org/10.1002/mrm.21286

Yu, H., Reeder, S.B., Shimakawa, A., Brittain, J.H., Pelc, N.J., 2005. Field map estimation with a region growing scheme for iterative 3-point water-fat decomposition. Magn. Reson. Med. 54, 1032–1039. https://doi.org/10.1002/mrm.20654

Yu, H., Shimakawa, A., McKenzie, C.A., Brodsky, E., Brittain, J.H., Reeder, S.B., 2008. Multiecho water-fat separation and simultaneous R 2* estimation with multifrequency fat spectrum modeling. Magn. Reson. Med. 60, 1122–1134. https://doi.org/10.1002/mrm.21737

Zhang, K., Yun, S.D., Shah, N.J., 2015. Tripled Readout Slices in Multi Time-Point pCASL Using Multiband Look-Locker EPI. PLOS ONE 10, e0141108. https://doi.org/10.1371/journal.pone.0141108

Zhu, M., Sun, Z., Ng, C.K., 2017. Image-guided thermal ablation with MR-based thermometry. Quant. Imaging Med. Surg. 7, 356–368. https://doi.org/10.21037/qims.2017.06.06

List of Publications arising from this thesis

Peer-viewed journal

[1] **Kisoo Kim**, Elodie Breton, Afshin Gangi, Jonathan Vappou, "Simultaneous fat-referenced PRFS thermometry and MR Elastography for the monitoring of thermal ablations", *Magnetic resonance in medicine*, 2019. Doi:https://doi.org/10.1002/mrm.28130

International Conference proceeding

[1] Jonathan Vappou, Paolo Cabras, **Kisoo Kim**, Pramod Rao, Afshin Gangi, and Elodie Breton "Monitoring high intensity focused ultrasound ablations in real time using interventional MR Elastography", *ISMRM 26th Annual Meeting & Exhibition-Paris*, 7458, 2018. *(Poster)*

[2] **Kisoo Kim**, Elodie Breton, Afshin Gangi, Jonathan Vappou, "Interventional MR Elastography and thermometry using simultaneous image refocusing (SIR) for multislice monitoring of thermal therapies", *ISMRM 26th Annual Meeting & Exhibition-Paris*, 7867, 2018. *(Poster)*

[3] **Kisoo Kim**, Elodie Breton, Afshin Gangi, Jonathan Vappou, "Simultaneous fat-referenced PRFS thermometry and MR Elastography for the monitoring of thermal ablation", *ISMRM 27th Annual Meeting & Exhibition-Montréal*, 0971, 2019. *(Oral)*

France national conference proceeding

[1] **Kisoo Kim**, Elodie Breton, Afshin Gangi, Jonathan Vappou, "Elastographie et Thermométrie par Résonance Magnétique simultanées avec séparation eau/graisse pour le suivi des ablations thermiques", *SFRMBM 4ème Congrès annuel*, Strasbourg, *(Oral)*

[2] **Kisoo Kim**, Elodie Breton, Afshin Gangi, Jonathan Vappou, "multislice interventional MR Elastography using Simultaneous Image Refocusing (SIR) ", 6ème journées scientifiques de la FMTS, Strasbourg, 2018. *(Oral)*

Prizes and honors

[1] 2018: SFRMBM stipend for the ISMRM 26th Annual Meeting, Paris, France

[2] 2018: ISMRM Trainee (Educational) stipend for the ISMRM 26th Annual Meeting, Paris, France

[3] 2019: SFRMBM stipend for the ISMRM 27th Annual Meeting, Montréal, Canada

[4] 2019: ISMRM Trainee (Educational) stipend for the ISMRM 27th Annual Meeting, Montréal, Canada

[5] 2019: Best student abstract, 3rd place, MRE study group meeting, ISMRM 27th Annual Meeting, Montréal, Canada

[6] 2019: Best student abstract, 2nd place, Interventional MR study group meeting, ISMRM 27th Annual Meeting, Montréal, Canada

[7] 2019: Magna Cum Laude Merit Award, ISMRM 27th Annual Meeting, Montréal, Canada

List of Figures

List of Tables

Biography

Kisoo Kim was born on August 2, 1989 in Gwacheon city, the Republic of Korea. He followed the secondary education in Korea and completed his bachelor and master study in the department of biomedical engineering, Kyung-Hee University, Korea. In 2016, he started his Ph.D. study at ICube-UMR7357, CNRS, University of Strasbourg. His project was the development of MRI techniques dedicated to interventional MR Elastography and MR Thermometry. In 2019, he was awarded Best student abstract and Magna Cum Laude Merit Award at ISMRM 27th Annual Meeting, Montréal, Canada.

UNIVERSITÉ DE STRASBOURG

ÉCOLE DOCTORALE MSII
ICube – UMR 7357

THÈSE présentée par :

Kisoo KIM

pour obtenir le grade de : **Docteur de l'Université de Strasbourg**
Discipline/ Spécialité : **Imagerie physique**
La date de soutenance : **26/11/2019**

Interventional MR Elastography for the monitoring of thermal ablations

THÈSE dirigée par :	
VAPPOU Jonathan	Chargé de Recherche, CNRS, Université de Strasbourg
GANGI Afshin	Professeur, Hôpitaux Universitaires de Strasbourg
RAPPORTEURS :	
PARKER Dennis L.	Professeur, University of Utah, UT
SALAMEH Najat	Professeur, University of Basel, CH

EXAMINATEURS :	
BRETON Elodie	Ingénieur de recherche, CNRS, Université de Strasbourg
FELBLINGER Jacques	Professeur, Université de Lorraine, Nancy

Introduction

Le cancer est récemment devenu la principale cause de décès dans les pays les plus développés. On estime à 3,9 millions le nombre de nouveaux cas de cancers et à 1,93 million le nombre de décès en 2018 en Europe. Parmi les procédures de traitement les plus répandues, les ablations thermiques des tumeurs (ou thermothérapie) présentent l'avantage de cibler précisément les zones à traiter tout en évitant le plus possible d'endommager les tissus sains environnants. La thermothérapie est souvent combinée à une méthode d'imagerie telle que la tomodensitométrie, l'échographie ou l'imagerie par résonance magnétique (IRM). Ce suivi par l'imagerie est nécessaire car il permet au radiologue de repérer les lésions, de décider d'une stratégie de traitement et de veiller au bon déroulement de la procédure. L'IRM est une modalité permettant d'étudier avec précision les tissus mous, fournissant des images avec un meilleur contraste comparées à celles obtenues par scanner ou échographie. De plus, il s'agit d'une technique d'imagerie non invasive et non ionisante permettant d'imager des organes profonds en trois dimensions et selon n'importe quelle orientation.

Le suivi des ablations thermiques par IRM a deux objectifs spécifiques : 1) le suivi en temps réel de l'évolution de la température dans la région traitée, afin de contrôler la quantité d'énergie déposée 2) l'évaluation en temps réel des effets du traitement sur les tissus, telle qu'une dégradation. La thermométrie IRM (TRM) est couramment utilisée pour contrôler le dépôt d'énergie thermique et estimer les dommages infligés aux tissus au cours des ablations thermiques guidées par IMR. Plus récemment, l'élasticité ou la rigidité des tissus, pouvant être mesurée par élastographie IRM (ERM), a fait l'objet d'une attention croissante en tant que biomarqueur complémentaire de la température.

Bien que le suivi de l'évolution de la température et de l'élasticité des tissus soit une technique récente largement exploitée dans le domaine de la recherche, cette technique n'est pas encore adoptée en tant que standard clinique pour le suivi des thermothérapies. Sa limitation à certains types de tissus et son faible taux de rafraichissement d'images ne répondent pas encore aux conditions d'utilisation clinique standard.

Développement d'une séquence ERM multicoupe rapide (Chapitre 3)

La première partie de ce travail a été consacrée au développement d'une séquence ERM multicoupe rapide permettant une meilleure couverture spatiale de la région concernée par la thermothérapie. Un système d’ablation HIFU (ultrasons focalisés de haute intensité) compatible IRM a été utilisé dans le cadre de cette thèse. Une couverture spatiale 3D complète de la zone d'ablation est privilégiée à un simple mode d'imagerie 2D pour deux raisons. Premièrement, les images 2D peuvent se retrouver décentrées par rapport à la région d’observation et ne pas rendre compte précisément de l’échauffement réel subi par les tissus au point focal, de sorte que l'augmentation maximale de la température et la localisation exacte du point focal peuvent être faussées. Deuxièmement, l’imagerie tridimensionnelle peut fournir avec précision la structure de la zone d'ablation, déterminée par la structure locale des tissus (flux sanguin, dépôt de chaleur, physiologie des tissus, etc.), que seule l’imagerie tridimensionnelle peut fournir. L'acquisition d'ERM est intrinsèquement lente en raison du nombre d'images acquises, à la fois à cause de l’utilisation de gradients bipolaires de sensibilité au mouvement (MSG +/-) et de la nécessité d’employer plusieurs décalages de phase entre l’onde mécanique et le MSG. Ce premier projet vise à proposer l'utilisation de la technique appelée SER pour « Simultaneous echo refocusing » (Feinberg et al., 2002) qui permet l’encodage ERM simultané et l’acquisition de 2 coupes par TR, afin d’obtenir un suivi multi-coupe des changements de température et d'élasticité au cours des ablations thermiques.

Cette technique consiste à utiliser deux impulsions d'excitation (RF) consécutives et leurs gradients de sélection de coupe (SS) respectifs pour sélectionner deux coupes (Figure R.1). Combinés à des gradients de lecture (RO) ayant subi une préparation adéquate de pré-déphasage, deux échos consécutifs (un par coupe) sont acquis. Plus spécifiquement, les gradients appliqués entre les deux impulsions RF n'affectent que l'aimantation excitée par la première impulsion RF, soit uniquement la première coupe, tandis que les gradients appliqués après la seconde impulsion RF affectent les deux coupes à la fois. L’aire consacrée au pré-déphasage des gradients de lecture correspond respectivement à la moitié et au quart de l’aire totale du gradient de lecture, afin de générer successivement l’écho nº2 (ADC 2, associé à l’impulsion RF nº2) et l’écho nº1 (ADC 1, impulsion RF nº1). Ainsi, deux échos sont générés au cours de la lecture à différents moments, chaque écho étant acquis avec un TE différent associé à une coupe.

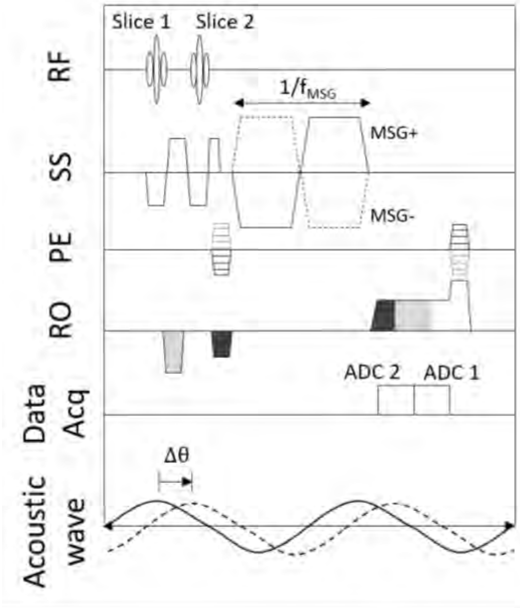

Figure R.1 Chronogramme de la séquence SER-GRE, intégrant le MSG et l'onde harmonique générée par un excitateur acoustique externe. 1 / f_{MSG} correspond à la période du MSG, qui permet l'encodage dit fractionnel du mouvement. Δθ représente le décalage de phase entre le MSG et l'excitation mécanique, les pas de phase employés étant répartis de manière égale sur un cycle de vibration.

Une première expérience réalisée sur fantôme a d'abord permis de confronter notre nouvelle séquence d'ERM à la méthode standard. Cette étape a permis de valider l'approche proposée, en montrant l'équivalence entre ERM classique et la séquence proposée, pour un gain de temps d'acquisition d'un facteur deux. Une deuxième série d'expériences a eu pour but de valider l'utilisation de la méthode SER pour le suivi des changements de température et d'élasticité pendant un échauffement par HIFU dans un fantôme constitué de gélatine et de muscle de poulet. Nous avons montré l'intérêt d'acquérir plusieurs coupes pour évaluer de manière précise les changements de température et de propriétés mécaniques lors d'une ablation par HIFU.

Résultats obtenus (Chapitre 3)

La figure R.2 présente les élastogrammes obtenus selon 3 méthodes d'acquisition ERM : notre séquence SER-GRE et deux séquences GRE à encodage fractionnel (TR = 1 ou 2 périodes mécaniques). Dans le cas de la séquence SER-GRE, les coupes nº1 et 2 ont été respectivement obtenues avec un TE égal à 11.4 / 8.6 ms. Pour chacune des 2 coupes, une différence d'élasticité entre les différents compartiments du fantôme (gel à 7% et 9%) est observée sur les élastogrammes reconstruits à partir des trois schémas d'acquisition, telle que reflétée par la longueur d'onde au sein des images de différence de phase. (Voir Chapitre 3.3.1.)

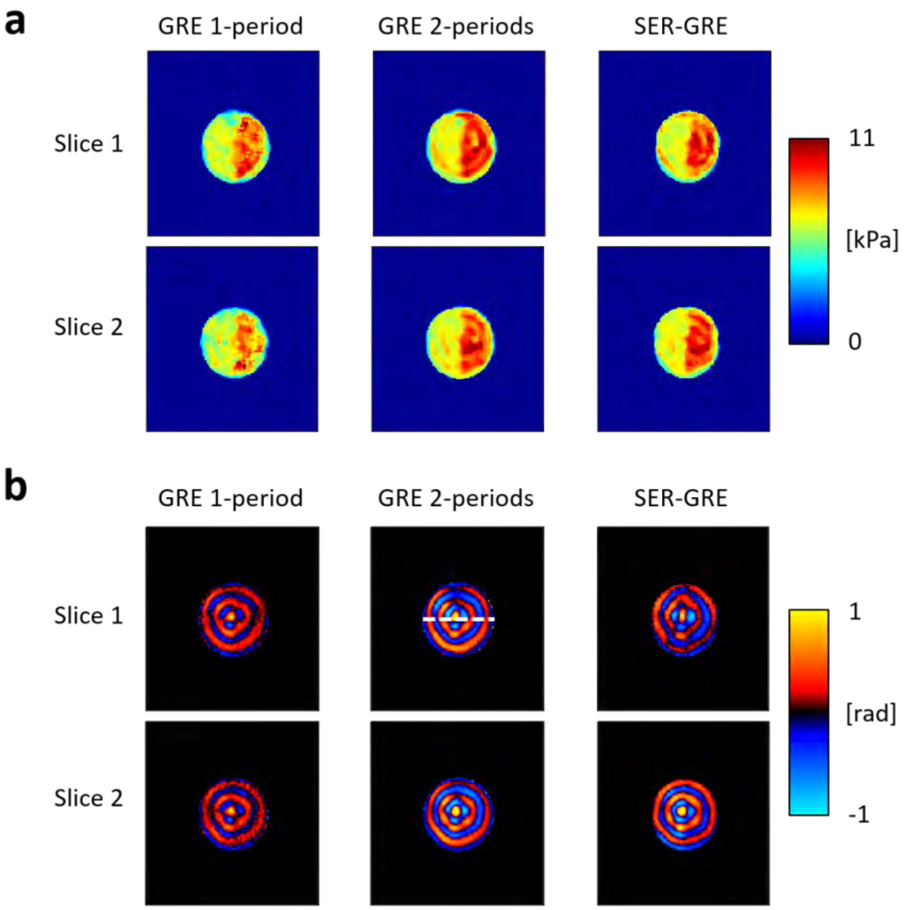

Figure R.2 (a) Élastogrammes et (b) Images de différence de phase (déphasage n°1) des coupes 1 et 2 obtenues à partir des séquences GRE et SER-GRE à la mesure nº2. La différence d'élasticité entre les compartiments à 7% et 9% de gélatine est visible aussi bien sur les élastogrammes que les images d'onde.

Figure R.3, les variations de température (ΔT) sont clairement visibles dans les 4 coupes. La tache focale est représentée au sein de la coupe nº2 et l'effet de la diffusion de chaleur est observé dans les coupes 1, 3 et 4. Des variations de l'onde et du module de cisaillement (μ et Δμ) sont mises en évidence au sein des 4 coupes. Utilisés comme références, le premier élastogramme et la première carte de température ont pu être reconstruits 24 s après le début de l'acquisition de l'IRM. L'élastogramme, tout comme la carte de température, peut ensuite être mis à jour toutes les 8 s selon le principe de la fenêtre glissante (Corbin et al., 2016b). Une analyse détaillée est décrite au Chapitre 3.3.2.

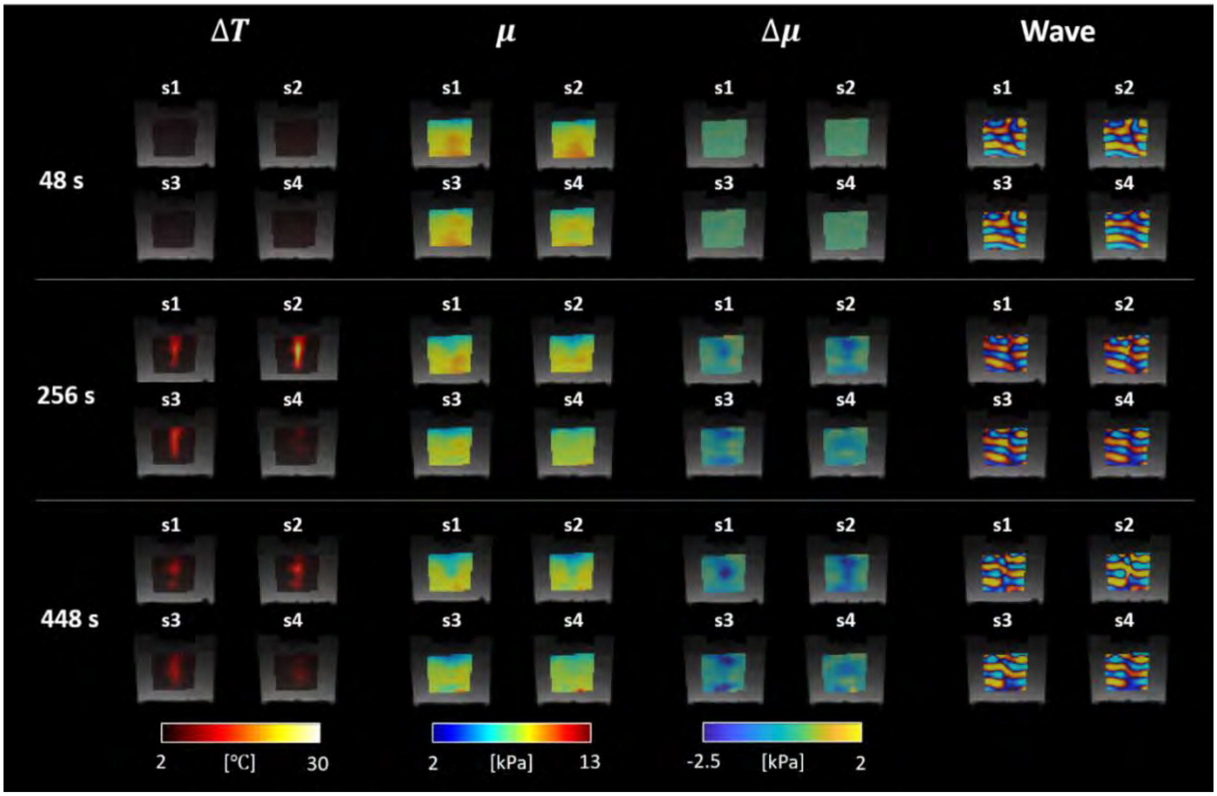

Figure R.3 Résultats de l'ablation HIFU. De gauche à droite, images des variations de température ΔT, cartes d'élasticité μ, cartes des variations d'élasticité Δμ et images d'onde (wave) superposées à l'image d'amplitude, avant (t=48 s), après le tir HIFU (t=256 s) et au cours de la phase de refroidissement (t=448 s). S1 à 4 sur la figure représentent respectivement les coupes 1 à 4. Les cartes de température témoignent d'une augmentation de la température très localisée en raison du tir HIFU. Des modifications du module de cisaillement (Δμ) sont observées dans la zone chauffée, correspondant à une longueur d'onde localement décroissante.

La figure R.4 illustre les cartes de température et d'élasticité obtenues pour 4 coupes contiguës une fois terminée la phase de chauffe par HIFU (300 s). La zone de l'ablation thermique a été repérée entre les coupes 2 et 3, toutefois, des zones affectées par un échauffement sont visibles sur les 4 coupes, comme le montre la figure R.4. Le premier élastogramme a pu être reconstruit 24,5 s après le début de l'acquisition

IRM, puis rafraîchi toutes les 8,2 s selon le principe de la fenêtre glissante. Les cartes d'évolution de la température s'affichaient toutes les 8,2 s après l'acquisition de l'image de phase de référence.

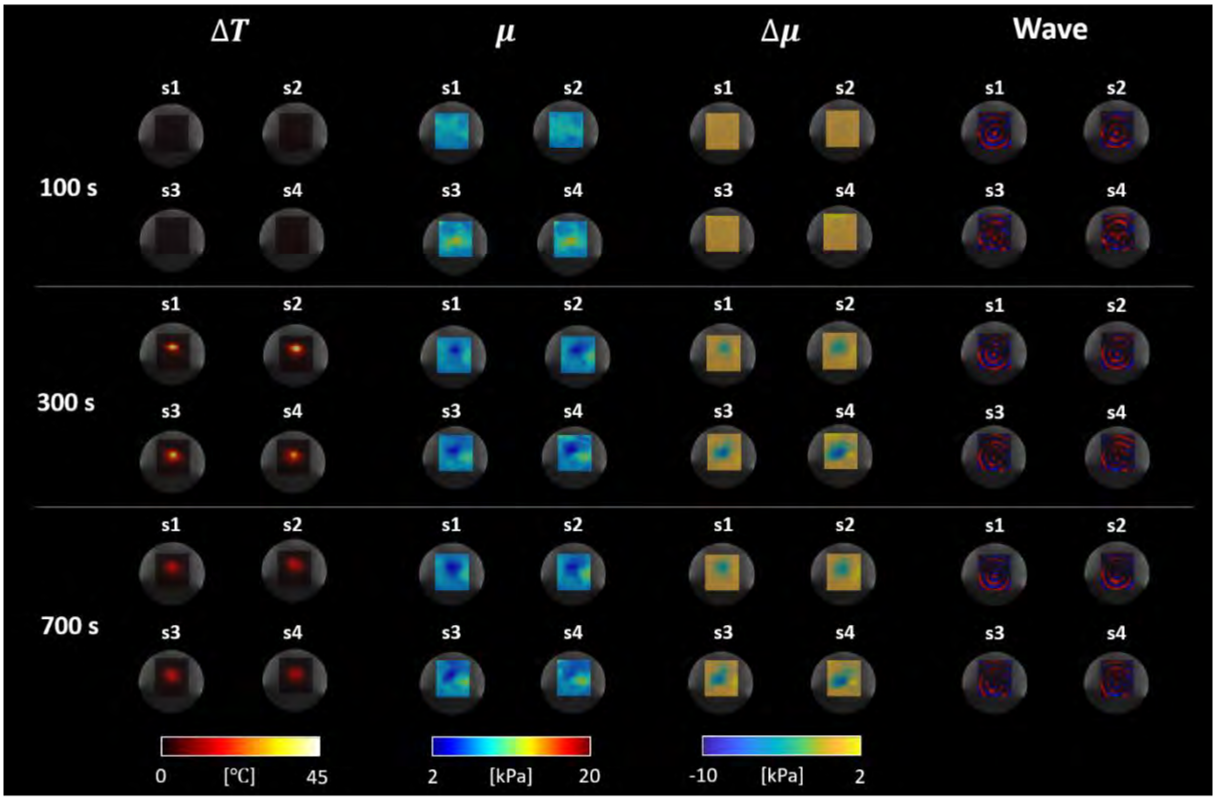

Figure R.4 Résultats de l'ablation HIFU. De gauche à droite, images des variations de température ΔT, cartes d'élasticité μ, cartes des variations d'élasticité Δμ et images d'onde (wave) superposées à l'image d'amplitude, avant (t=100 s), après le tir HIFU (t=300 s) et au cours de la phase de refroidissement (t=700 s). S1 à 4 sur la figure représentent respectivement les coupes 1 à 4. Les cartes de température témoignent d'une augmentation de la température très localisée en raison du tir HIFU. Des modifications du module de cisaillement (Δμ) sont observées dans la zone chauffée, correspondant à une longueur d'onde localement décroissante.

Conclusion (Chapitre 3)

Cette étude préliminaire présentée dans le Chapitre 3 a montré que la méthode SER pouvait être une bonne option d'accélération des séquences d'ERM interventionnelles. La méthode SER-GRE proposée ici permet d'acquérir des élastogrammes et des cartes de température pour des coupes contiguës, dans un délai d'acquisition plus court que les séquences d'ERM ordinaires. Deux coupes par TR sont acquises, partageant un seul MSG d’encodage du mouvement mécanique. Ainsi, il est possible de suivre simultanément la propagation des ondes et les changements de température dans différentes coupes. Cette technique fournira une autre option d’accélération pour une acquisition rapide multi-coupe lors d’une intervention guidée par IRM.

La thermométrie PRFS référencée à la graisse (Chapitre 4)

La deuxième partie de cette thèse présente une nouvelle stratégie d'acquisition IRM rendant possible la thermométrie et l'élastographie simultanées pour le suivi des ablations thermiques dans les tissus mous, incluant ceux contenant de la graisse. Dans ce but, une séquence d'acquisition mêlant ERM et séparation eau/graisse a été développée. En effet, les méthodes d'ERM/TRM interventionnelles actuelles exploitent la thermométrie PRFS (*Proton Resonance Frequency Shift*), qui est limitée aux tissus aqueux, car leur utilisation dans des tissus contenant de la graisse peut entraîner des erreurs importantes d'estimation de la température. L'objectif général de ce chapitre est d'étendre la méthode d'ERM/TRM interventionnelle à n'importe quel type de tissu mou, y compris les tissus contenant de la graisse. À cette fin, la thermométrie PRFS exploitant la méthode de séparation eau / graisse (FR-PRFS, *Fat-Referenced-PRFS*) par déplacement chimique doit être combinée avec l'ERM / TRM interventionnelle actuelle. La stratégie proposée offre une amélioration du suivi combiné ERM/TRM en temps réel des ablations thermiques, en élargissant sa précision dans les tissus mous, y compris les tissus contenant des graisses, tout en maintenant le temps d'acquisition similaire. D'une part, un algorithme itératif exploitant la méthode des moindres carrés (IDEAL) est utilisé pour une séparation rapide et robuste du signal de l'eau et de la graisse (Tsao and Jiang, 2013; Yu et al., 2008). Le modèle de signal eau-graisse est résolu en utilisant des jeux de données à TE multiples. D'autre part, les reconstructions ERM nécessitent l'acquisition de plusieurs images avec des décalages de phase variables entre l'onde mécanique et les gradients de sensibilité au mouvement (MSG), afin de capturer l'onde de cisaillement à des instants différents lors de sa propagation. La stratégie décrite ici tire parti de l'acquisition de plusieurs déphasages en ERM permettant d'obtenir les différentes valeurs de temps d'écho (TE) nécessaires à la séparation eau-graisse. Pour cela, les temps d'écho et les décalages de phase ERM sont incrémentés conjointement au cours de l'acquisition (Figure R.5). Le nombre de décalages de phase ERM et le nombre de TE utilisés pour résoudre l'algorithme IDEAL sont les mêmes. Par conséquent, l'élastogramme et la carte de température FR-PRFS sont mis à jour en même temps. Cette méthode offre ainsi la possibilité d'enregistrer des informations de déplacements chimiques dans un seul jeu de données ERM.

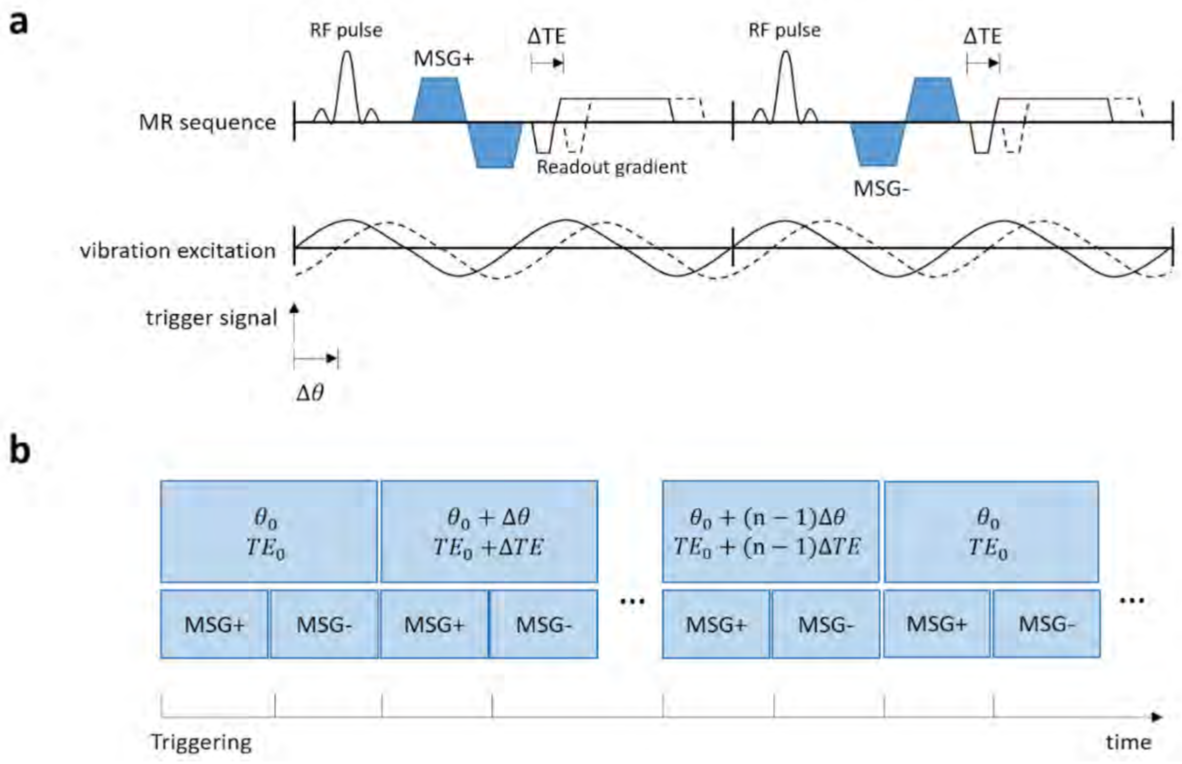

Figure R.5 (a) Chronogramme schématique de la séquence GRE ERM pour la thermométrie FR-PRFS et l'ERM simultanées. Les impulsions RF, les MSG et les gradients de lecture sont représentés sur une seule ligne. TE est incrémenté de ΔTE, Δθ représente le décalage de phase nécessaire en ERM. (b) Schéma résumé de l'acquisition du signal, avec « n » le nombre de décalages de phase Δθ et de temps d'écho ΔTE. Les images sont acquises par paire en alternant la polarité du MSG. Chaque paire d'images est acquise avec le même TE spécifique et le même décalage de phase.

Pour la validation, trois séries d'expériences ont été effectuées : premièrement, la mesure de la température a été validée dans une expérience sur fantômes via comparaison avec mesure thermométrique de référence (par fibres optiques). La deuxième série d'expériences a été effectuée pour valider les cartes d'élasticité, en les comparant à celles reconstruites par la séquence ERM de référence. Enfin, cette méthode a été testée lors d'expériences HIFU menées ex-vivo dans du tissu de porc avec une fraction adipeuse homogène.

Résultats de chapitre 4

La figure R.6 présente les variations de température (ΔT), les variations d'élasticité (Δμ) et les images d'ondes mesurées avant (t=40 s) et pendant les 2 phases de montée en température (t=200 s puis t=400 s) pour une expérience de validation réalisée sur fantôme. Afin de mimer une ablation thermique, un circuit d'eau chaude (~90°) a été manuellement activé via une seringue. L'augmentation de la température s'accompagne ici d'un ramollissement du milieu, ce qui correspond à une diminution du module de cisaillement sur les cartes Δμ et à une diminution locale de la longueur d'onde de cisaillement sur les images d'onde.

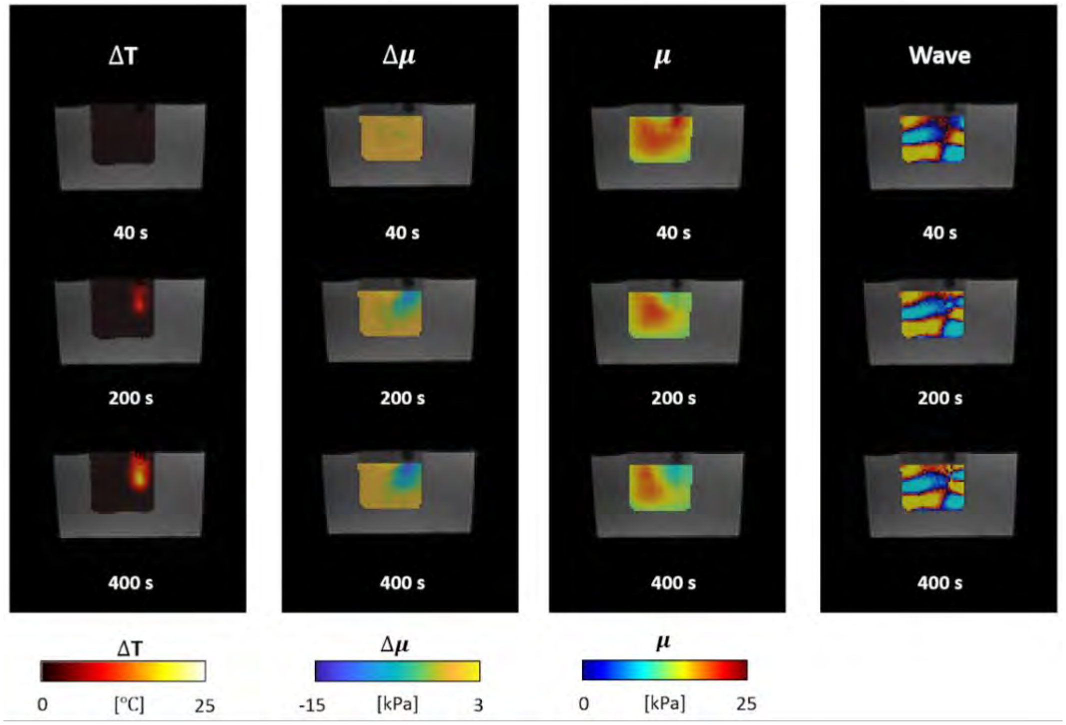

Figure R.6 De gauche à droite, cartes des variations de température (ΔT), cartes des variations d'élasticité (Δμ), élastogrammes (μ) et images d'onde superposées à l'image d'amplitude correspondante, obtenues avant (t=40 s) et pendant la phase de chauffe (t =200 s et 400 s). Au cours de cette dernière, une augmentation localisée de la température est observée. Le gel de l'inclusion se ramollit, comme en témoigne la diminution relative de la longueur d'onde de cisaillement visible sur les images d'onde.

La deuxième série d'expériences a été effectuée pour valider les cartes d'élasticité, en les comparant à celles reconstruites par la séquence ERM de référence (Figure R.7). Ces expériences ont montré un très bon accord, sans différences significatives avec une erreur relative égale à 4.7 ± 1.8% sur l'ensemble du fantôme. L'utilisation de jeux de données à TE multiples permet ainsi de reconstruire des élastogrammes obtenus en ERM standard n'exploitant qu'un seul TE. Une analyse détaillée est décrite au Chapitre 4.4.1-2.

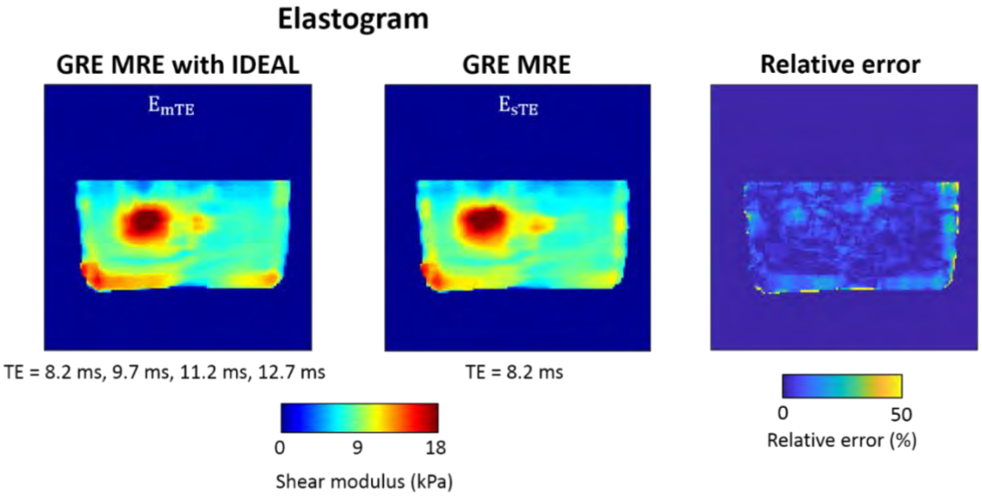

Figure R.7 Élastogrammes reconstruits à partir de jeu de données incluant plusieurs TE (E_{mTE}) et un seul TE (E_{sTE}). L'erreur relative est donnée par la formule : $|E_{mTE} - E_{sTE}|/E_{sTE} \times 100$ et est évaluée à 4.7 ± 1.8% dans l'ensemble du milieu. Ceci nous permet d'avancer que l'ERM-IDEAL fournit des élastogrammes semblables à ceux obtenus en ERM classique.

Pour les expériences HIFU menées ex-vivo, la figure R.8 rend compte des variations de température ΔT subies par les tissus, ainsi que des modifications de la rigidité relative du milieu (RSC = $\Delta\mu$ / $\mu 0$, où $\mu 0$ est la rigidité initiale), des cartes d'élasticité et des images d'onde mesurées avant (t =100 s), après échauffement par HIFU (t=250 s) et pendant la phase de refroidissement (t =570 s) au cours de 4 expériences. En définitive, il a été constaté que le module de cisaillement diminuait au niveau du point focal, comme indiqué sur les cartes RSC. Une analyse détaillée est décrite au Chapitre 4.4.3.

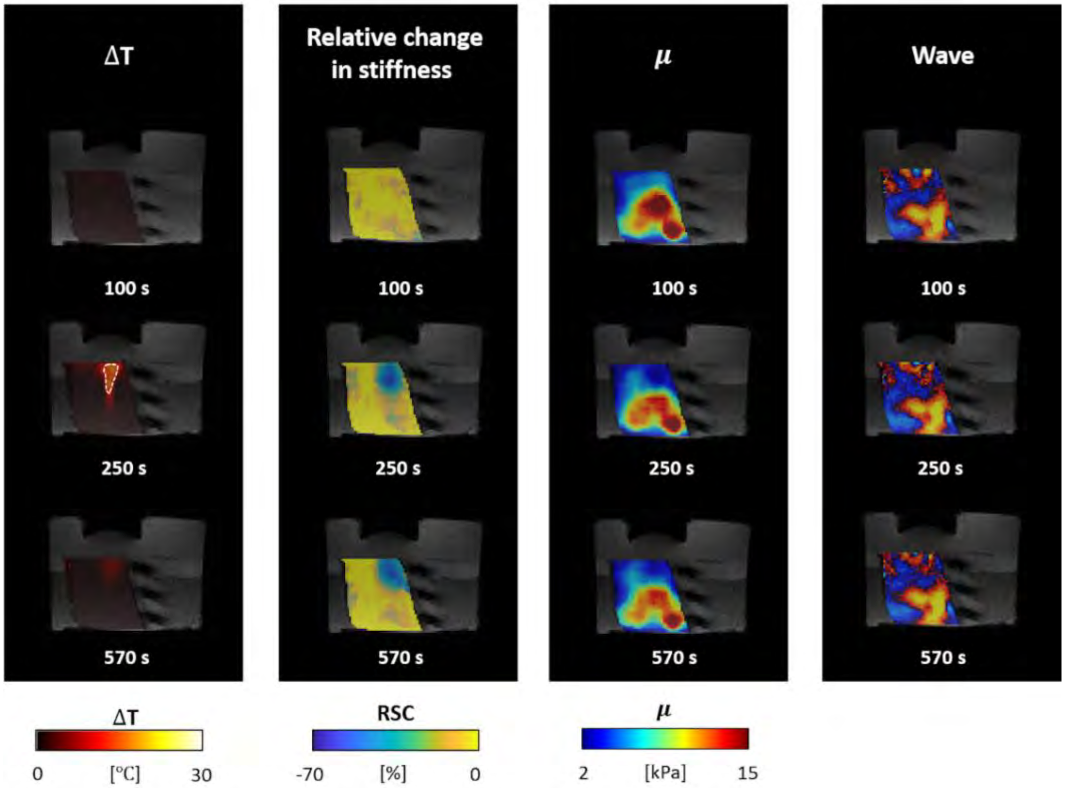

Figure R.8 Expérience Hifu ex vivo dans du muscle de porc. De gauche à droite, variations de température (ΔT), modification de la rigidité relative (RSC), cartes d'élasticité et images d'onde superposées avec l'image d'amplitude pour une même valeur de TE, avant (t =100 s), pendant la phase de chauffe HIFU (t=250 s) et au cours de la phase de refroidissement (t =570 s).

Conclusion chapitre 4

Dans le chapitre 4, un nouveau cadre a été développé pour la thermométrie FR-PRFS associée à l'ERM permettant le suivi des ablations thermiques en temps réel. Ce protocole a été validé sur fantôme puis ex-vivo dans du tissu de porc. La stratégie d'acquisition s'appuie sur la combinaison de plusieurs méthodes de compensation de la phase : exploitation de plusieurs temps d'écho et de plusieurs déphasages entre le gradient de sensibilité au mouvement et l'excitation mécanique. La thermométrie FR-PRFS permet d'obtenir des mesures de température précises dans tous les tissus mous, y compris les tissus contenant de la graisse. Associée à l'ERM, notre méthode peut donc aider les cliniciens pour le suivi des traitements d'ablations thermiques dans divers types de tissus.

Conclusion générale

Dans cette thèse de doctorat , nous avons présenté deux développements différents afin de surmonter certaines des limitations actuelles de l'ERM et de la MRT interventionnelles simultanées, en termes d'extension à la couverture spatiale de la région ciblée et au développement d'une nouvelle méthode de surveillance des ablations thermiques pour tous les types de tissus mous, y compris les tissus adipeux. Ces contributions visent à améliorer la sécurité et l'efficacité des ablations thermiques guidées par IRM.

Liste des publications découlant de cette thèse

Revues internationales à comité de lecture

[1] **Kisoo Kim**, Elodie Breton, Afshin Gangi, Jonathan Vappou, “Simultaneous fat-referenced PRFS thermometry and MR Elastography for the monitoring of thermal ablations”, *Magnetic resonance in medicine*, 2019, Accepted: 24 November 2019, DOI: 10.1002/mrm.28130

Conférences internationales avec actes

[1] Jonathan Vappou, Paolo Cabras, **Kisoo Kim**, Pramod Rao, Afshin Gangi, and Elodie Breton “Monitoring high intensity focused ultrasound ablations in real time using interventional MR Elastography”, *ISMRM 26th Annual Meeting & Exhibition-Paris*, 7458, 2018. *(E-poster)*

[2] **Kisoo Kim**, Elodie Breton, Afshin Gangi, Jonathan Vappou, “Interventional MR Elastography and thermometry using simultaneous image refocusing (SIR) for multislice monitoring of thermal therapies”, *ISMRM 26th Annual Meeting & Exhibition-Paris*, 7867, 2018. *(E-poster)*

[3] **Kisoo Kim**, Elodie Breton, Afshin Gangi, Jonathan Vappou, “Simultaneous fat-referenced PRFS thermometry and MR Elastography for the monitoring of thermal ablation”, *ISMRM 27th Annual Meeting & Exhibition-Montréal*, 0971, 2019. *(Présentation orale)*

Conférences nationales

[1] **Kisoo Kim**, Elodie Breton, Afshin Gangi, Jonathan Vappou, “Elastographie et Thermométrie par Résonance Magnétique simultanées avec séparation eau/graisse pour le suivi des ablations thermiques”, *SFRMBM 4ème annuel*, Strasbourg, 2019 *(Présentation orale)*

[2] **Kisoo Kim**, Elodie Breton, Afshin Gangi, Jonathan Vappou, “multislice interventional MR Elastography using Simultaneous Image Refocusing (SIR) ”, 6èmes journées scientifiques de la FMTS, Strasbourg, 2018. *(Présentation orale)*

Prix et distinctions

[1] 2018: SFRMBM stipend for the ISMRM 26th Annual Meeting, Paris, France

[2] 2018: ISMRM Trainee (Educational) stipend for the ISMRM 26th Annual Meeting, Paris, France

[3] 2019: SFRMBM stipend for the ISMRM 27th Annual Meeting, Montréal, Canada

[4] 2019: ISMRM Trainee (Educational) stipend for the ISMRM 27th Annual Meeting, Montréal, Canada

[5] 2019: Best student abstract, 3rd place, ERM study group meeting, ISMRM 27th Annual Meeting, Montréal, Canada

[6] 2019: Best student abstract, 2nd place, Interventional MR study group meeting, ISMRM 27th Annual Meeting, Montréal, Canada

[7] 2019: Magna Cum Laude Merit Award, ISMRM 27th Annual Meeting, Montréal, Canada